UC Berkeley
UC Berkeley Electronic Theses and Dissertations

Title

MEMS Materials and Temperature Sensors for Down Hole Geothermal System Monitoring

Permalink

https://escholarship.org/uc/item/0v30k44g

Author

Wodin-Schwartz, Sarah

Publication Date

2013

Peer reviewed|Thesis/dissertation

MEMS Materials and Temperature Sensors for Down Hole Geothermal System Monitoring

by

Sarah Wodin-Schwartz

A dissertation submitted in partial satisfaction of the

requirements for the degree of

Doctor of Philosophy

in

Engineering - Mechanical Engineering

in the

Graduate Division

of the

University of California, Berkeley

Committee in charge:

Professor Albert P. Pisano, Chair
Professor Liwei Lin
Professor Eugene E. Haller

Spring 2013

MEMS Materials and Temperature Sensors for Down Hole Geothermal System Monitoring

Copyright © 2013

by

Sarah Wodin-Schwartz

Abstract

MEMS Materials and Temperature Sensors for Down Hole Geothermal System Monitoring

by

Sarah Wodin-Schwartz

Doctor of Philosophy in Engineering - Mechanical Engineering

University of California, Berkeley

Professor Albert P. Pisano, Chair

The advancement of renewable energy technologies is critical due to the unsustainable nature of currently used energy sources and the need to meet increasing energy demands. A broad and diverse energy plan is important for long term energy independence and stability. Geothermal energy sources including hydrothermal systems and enhanced geothermal systems (EGS) should play a key role in this energy plan. Geothermal energy is the most reliable, currently developed, schedulable alternative energy source. It is estimated that improvements in these systems have the potential to economically access at least 200,000 exajoules of energy to the U.S. within 50 years [1]. The progress in developing this field is challenging in part due to the complex geochemical and geophysical properties of the subsurface environment. This dissertation reviews geothermal energy system limitations resulting from current well monitoring technologies and introduces microelectromechanical systems (MEMS) sensors as a means of optimizing well performance. Harsh environment MEMS offer an ideal alternative to macro-scale sensors due to their harsh environment material compatibility, the ability to couple MEMS with wireless RF transmission systems, and their small footprint.

In this work, harsh environment MEMS encapsulation materials are tested in simulated geothermal environments to determine their survivability. The sensors must be encapsulated to provide protection from oxidation, erosion, surface roughening, and other chemical attacks. Encapsulation materials such as silicon carbide, sapphire, vitreous carbon, and poly-crystalline diamond were tested in multiple simulated geothermal environments to determine a suitable protective layer for these MEMS devices. Once appropriate materials are determined, two temperature sensors are designed, optimized, fabricated, and tested. The first sensor improves upon existing out-of-plane MEMS capacitive temperature sensor devices by utilizing harsh environment materials. The second sensor is a novel in-plane design optimized to linearize capacitive output. These sensors are tested up to over 650 °C.

For my mom and dad. I hope this makes up for not thanking you in 6th grade.

Contents

List of Figures

ix

List of Tables

Acknowledgements

I would like to thank my advisor, Albert Pisano, for his support and ability to show me how my research fits into the bigger picture. I always left your office feeling more confident, with a smile on my face. I would also like to thank my dissertation committee members, Professor Liwei Lin and Professor Eugene Haller for your questions and advice during my qualifications exam and during my writing process.

I would like to thank the whole BMAD lab for their help and support. In particular I would like to thank Dr. Debbie Senesky, Dr. Jim Cheng, Matt Chan, Fabian Goericke, Dr. Gabriele Vigevani, Dr. David Myers, Yegan Erdem, Dr. Ting-Ta Yen, and Dr. Adrienne Higa. All of you have helped me throughout my time at Berkeley socially, academically, and professionally. In addition to lab mates, the nanolab staff has be a very valuable resource through my research time at U.C. Berkeley.

Finally, I would like to thank my family and friends for their constant love and support. Thank you mom for always making sure I understood what I was talking about by making me explain it to you, dad for all of the long phone conversations, and Aaron for being a great older brother.

Chapter 1

Introduction

1.1 Overview

This dissertation discusses the testing of specialized harsh environment materials for use in down hole geothermal environments, as well as the design, fabrication, and testing of two temperature sensors for operation within that environment. These sensors are designed for profiling a geothermal well, see Figure 1.1, giving well operators real time data to improve daily well operation, safety, and reduce well exploration costs.

There are two main goals of this project. The first is to determine and evaluate materials that can survive within down hole geothermal environments. This includes the testing of substrate, sensor, and encapsulation materials in liquid, vapor, critical point, and supercritical water and subcritical simulated geothermal brine. Once the appropriate materials are determined, the second research goal, the design of MEMS temperature sensors, is completed. These temperature sensors have the ability to be integrated with a suite of MEMS sensors and harsh environment compatible SiC electronic circuits for down hole monitoring. Both in-plane and out-of-plane passive SiC temperature sensors are designed. Each of these sensors is fabricated in the UC Berkeley Nanofabrication Center and tested in high temperature environments.

The following chapters of this dissertation describe the design, fabrication, testing, and experimentation that was conducted to achieve these goals. However, before going into detail on the project specifics, this chapter discusses some background of geothermal energy potential and how the addition of sensors, particularly MEMS sensors, can improve geothermal well performance. This chapter also gives some background on exposure testing and defines the down hole geothermal environment.
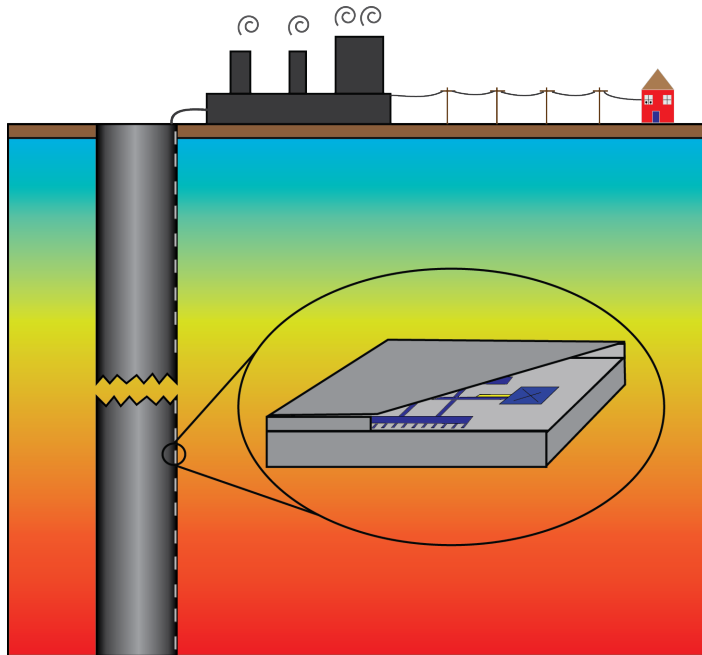
Figure 1.1. A geothermal well is profiled with a suite of encapsulated MEMS sensors to monitor the down hole environment.

1.2   Geothermal Energy Potential

The advancement of renewable energy technology is critical due to unstable energy resources and the predicted increase (by a factor of two) in electrical demand by 2030 [2]. The improvement of hydrothermal geothermal systems and the development of enhanced geothermal systems (EGS) has the potential to economically tap into at least 200,000 exajoules of stable, base load energy in as little as 50 years [1] . However, engineering reservoirs is challenging due to the complex geochemical and geophysical properties of subsurface environments. Most current technology utilizes surface measurements to develop thermal and geophysical profiles (e.g., heat flow, electrical resistivity and magnetotelluric surveys). The data collected can only be used for predictions of down well behaviors based on averaged well properties.

The improvement of subsurface sensors is necessary to realize this large U.S. geothermal potential. Increased knowledge of down hole conditions including temperatures, pressures, chemical composition, depth, flow rates, and other physical parameters are useful data for geothermal plant operators. For example, an understanding of the physical and chemical conditions would improve well operators' abilities to determine optimized reflow rates, energy extraction rates, and well lifetime expectancy. This data could also be used to improve geothermal modeling, increasing the life of current wells and giving more accurate lifetime prediction information for potential well sites. Sensors would also allow for appropriate safety precautions (or predictive measures) to be taken when approaching anomalies in boreholes. Operators need to plan for sudden drops in pressure in the borehole due to wash-outs or

spikes in pressure from gas or fluid pockets in reservoirs [3] [4]. Current down well sensors are not sufficient for permanent down hole environment monitoring. Harsh environment sensors used in conjunction with advanced feedback systems would allow for well system optimization, enhanced well operation, reduced exploratory well costs, and increased well lifetime.

1.3   Present Day Geothermal Well Monitoring

State-of-the-art geothermal sensors can be broken down into two categories, exploratory tools for site planning and well monitoring tools. Each of these two categories has both surface and sub-surface tools. Surface exploratory tools are focused around locating geological indicators such as carbonates (sinter and tufa), clays, or sulfates. All of these result from hydrothermal alteration and thermal anomalies such as surface exhaust vents and hot springs. These indicators can be discovered using direct surface sample analysis or through the use of air and space craft imagery. Research in the use of infrared imagery has given promising results in lowering exploratory well location identification costs [5]. Initial well identification is an important part of the exploratory process as it shows where test wells should be constructed. However, surface exploratory sensing does not give complete evidence that a given location is ideal for geothermal energy extraction. Once a potential well site has been identified, down hole sub-surface exploratory tools are needed to determine the wells viability.

State-of-the-art sub-surface exploratory tools are very large and expensive. Sub-surface tools are used to determine rock thicknesses, porosities, fracture patterns, pressure, temperature, salinity, pH, and steam quality. In addition, positional and angular sensors are important for drilling navigation for very deep and deviated (non-vertical) holes. This data is currently acquired using thermal, magnetic, electrical, radiation, and acoustic sensors [6]. All of these properties are collected to generate a subsurface map to determine the ideal locations to drill both production and re-injection wells for power generation. Usually all of these tools are combined into a single multi-tool that is sent down hole for temporary well state analysis. These probes are macro-scale and require active cooling or expensive Dewar flask sealing while in the sub-surface environment due to the harsh environmental constraints. These tools are very long, up to 6 feet in length, and are only capable of 4-6 hours of down hole operation [7]. While all of the currently available data is valuable, well exploration and field development makes up over half, an average of 63% on a 50-megawatt plant, of a geothermal electric plant start-up cost [8]. This cost can be reduced by increasing the accuracy of subsurface maps and models based on long-term monitoring of subsurface chemistry, pressure, and temperature.

Currently, most well operational monitoring sensors are permanently affixed at the surface level. These sensors monitor properties including flow rate, surface water temperature, surface water pressure, and water chemical composition. This does not give the most immediate or accurate information as to the environmental conditions down hole [4]. These sensors

record average well properties of the well as a whole. There are no accurate measurements for an operator to use to identify and address well problems at a specific locational depth. While down hole sensing tools used during well operation to monitor well performance exist, these devices are limited to short time durations. Some monitoring sensor systems claim to be permanent down hole fixtures; however, they are currently either limited by temperature, exposure time, or both. Newer fiber-optic technologies are currently under investigation for down hole applications; however, the best suited cable is currently limited to 300 °C [9], [10]. These optical fibers suffer from hydrogen darkening, which can lead to exceeding the optical budget of the cables as they become opaque. Cabling is costly as it must run the full length of the well to transmit optical pulses.

1.4   Geothermal Environments

For the purposes of this research, a definition of a characteristic geothermal well environment is desired. However, geothermal environments are characterized by large ranges pressures, temperatures, and corrosive chemistries. There is no typical geothermal brine chemistry. Some of the most common components found in geothermal brine are water, silica, chlorine, sodium, and carbon dioxide. Individual wells will have contaminants ranging from salts and sulfurs to toxic heavy metals. These contaminants can be found suspended in solution and precipitated. A summary of U.S. geothermal well chemistries was made for the US DOE EERE Geothermal Technologies Program [11], and its extensive detailed data confirms this wide chemical variation from well to well. A summary of some key well properties of 5 U.S. wells is shown in Table 1.4 [11]. Dissolved gas ratios change as geothermal well conditions and compositions change over time with well re-injection. These changes can lead excessive wear on well components that were designed to meet the parameters of the wells original chemical state. High levels of sulfur, like those seen in wells in Japan, can lead to the formation of sulfuric acid and the corrosion of piping systems. These changes in dissolved gas ratios can also lead to toxic gas emissions. High levels of chlorine salts found in U.S. wells can lead to the formation of HCl acid, which will corrode pipes when found in high concentrations. All of these factors can lead to the early abandonment of wells costing millions of dollars.

State	Temperature (°C)	pH	Na (ppm)	Ca (ppm)	SiO_2(ppm)
Nevada	153.9	6	430	11	79
Nevada	231.1	8.9	363	3	-
California	255	5	78000	37735	625
California	351	5.3	53000	27500	4
Utah	432.7	8.3	160	12	-

Table 1.1. Summary of some geothermal well properties for 5 U.S. wells.

In addition to a variety of chemistries, well pressures and temperatures have a wide range. High enthalpy sources can be utilized to run turbines directly. Lower enthalpy sources with lower quality steam can be used with more complex turbine systems to generate electricity. The pressure and temperature values correlate to the extraction of liquid, vapor, or supercritical brines. These temperatures and pressures change over time with the use of the well and with the changing well chemistry. These pressure and temperature ranges are so vast that the geothermal industry has had to develop multiple types of energy harvesting systems to run the plant turbines.

Hydrothermal Systems

The geothermal environment is so diverse that there are three categories of turbine systems used to generate electric power in hydrothermal systems. The highest quality steam for hydrothermal systems can be pumped directly into a turbine that powers an electric generator. This is shown schematically in Figure 1.2. This type of system can be seen at The Geysers geothermal plant facility in northern California. Flash steam plants are built in locations that produce lower quality geothermal fluids. These wells produce a mixture of gaseous and pressurized liquid brine, which must be expanded to steam. Water temperatures above 182 °C can be used in a flash steam system in which the liquid is pumped into an expansion chamber to drop the brine pressure, changing the liquid to a vapor. This vapor is then pumped into at turbine to run a generator. The lowest grade of hydrothermal brine, which can not be flashed to steam to run a turbine directly, can be fed into binary-cycle systems. These systems use a heat exchanger to collect the thermal energy from the brine. Cleaner fluid in a closed loop is converted to steam using this heat and is then fed into a turbine system. This is the most common type of hydrothermal generation system in the U.S. due to the abundance of moderate temperature water sources [12]. Many hydrothermal systems utilize a combination of heat exchangers and expansion tanks.
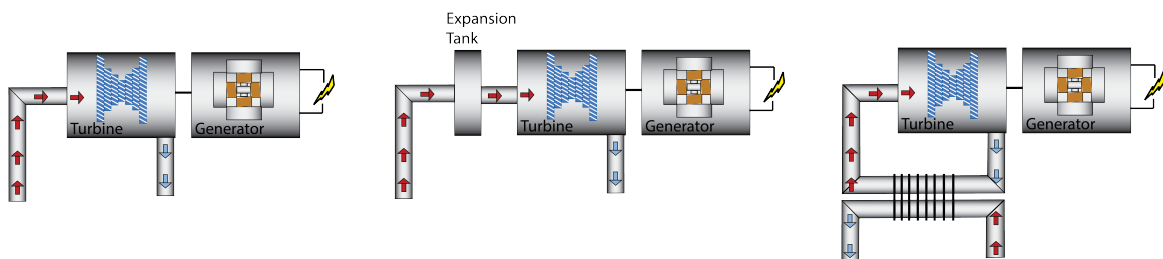
Figure 1.2. (Left) Dry steam plants are used at high enthalpy hydrothermal locations. (Center) Flash steam plants are used in hydrothermal locations that pump a steam/liquid brine mixture. (Right) Binary-cycle steam plants are used in hydrothermal locations with moderate temperature sources.

Enhanced Geothermal Systems

Enhanced geothermal systems (EGS) add more diversity to the already expansive potential environmental conditions of the down hole geothermal environment. In EGS, there is no underground geothermal brine reservoir from where fluid is pumped to a turbine. In EGS power generation, wells are dug down to into hot rock layers, which initially have poor permeability. Forcing water through this rock area reopens pre-existing fractures to increase permeability. Water can then be pumped down into the rock fractal system and pumped back up as a heated fluid [12]. This is shown schematically in Figure 1.3. Since EGS plants do not require pre-existing hot sub-surface fluids, they increase geothermal energy production location potential. This could move geothermal energy harvesting to U.S. locations away from the west coast, the traditional U.S. location for geothermal energy production. Current down hole sensing technology is not developed to a point where subsurface fluid flow patterns can be effectively modeled. This makes reservoir engineering very challenging, and results in the need for multiple production wells to recollect heated water supplied by the reinjection well. There is also the potential for large water losses into the rock fracture network.
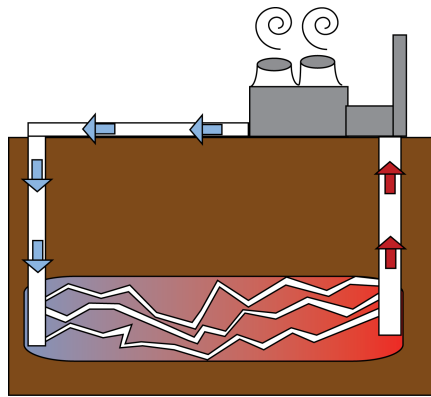
Figure 1.3. Schematic of an EGS plant with cold water entering the hot rock fractal zone and exiting as heated water.

Temperature Range and Resolution

A temperature sensor for down hole geothermal environments must measure both temperature fluctuations due to changes in re-injection depth over a large temperature range, and small temperature changes over time in the well due to the natural well life cycle. For this reason, both temperature resolution and range are important sensor parameters. Water reaches its critical point at 374 °C at 22 MPa (a depth of approximately 2200 meters assuming atmospheric pressure at the well surface and a liquid water column). In order to have the same sensor design used to profile the depth of the well, it should be able to measure temperatures in both supercritical and liquid brine phases. A maximum measurable temperature of 400 °C was selected as it is in the supercritical phase for water and higher than most

wells in the U.S.. A lower bound for the temperature range of 90 °C was chosen as it sets a range that includes 99.98% of geothermal wells in the U.S.. This gives a 310 °C temperature range over which the sensor should have a linear response. While good temperature sensors able to operate at these higher temperatures can achieve resolutions as small as 0.05 °C [13], achieving resolutions to this tolerance comes at the cost of sensor range. Most off the shelf temperature sensors with a 300 °C range have a resolution of 0.1-2 °C [14][15]. These values are all bandwidth dependent. For geothermal applications, the high bandwidth is not essential. A 10 Hz bandwidth was chosen as a low frequency value.

1.5 Exposure Testing

Exposure testing as used in this research is the placement of MEMS materials within a simulated environment to correlate experimental deterioration or robustness to damage or success within the down hole geothermal environment. It is important to closely match the application environment to the simulation so that the data collected is relevant. MEMS materials were exposed to both supercritical and sub-critical conditions in an attempt to match as many physical parameters as possible in the tests conducted since there is no defined characteristic geothermal brine condition. The temperature sensor range of 90 °C to 400 °C covers a range of water phases from vapor to liquid to supercritical depending on the applied pressure. In the first set of experiments, harsh environment materials including SiC and sapphire were exposed to a liquid, vapor, critical point, and supercritical environments. Silicon was used as a control for these tests to ensure that harsh environment materials are required within the down hole geothermal environment.

In the second set of tests, NaCl was added to the water environment to see how SiC, sapphire, diamond, and vitreous carbon survived a more characteristic brine environment. The brine tests were conducted in a liquid environment, 360 °C and 25 MPa, to keep the NaCl in solution. Also, most geothermal wells within the U.S. have temperatures at or below 350 °C, so sub-critical conditions yield more directly applicable results.

1.6 MEMS for Geothermal Monitoring

Harsh environment MEMS sensors offer an ideal alternative to macro-scale sensors due to their robustness and small footprint. MEMS sensors and packaging are nearly planar and centimeters in size. This reduction in sensor size allows the sensors to be mounted to well casings for permanent monitoring, or to be easily inserted and removed from wells for temporary monitoring without the well obstruction seen with current technologies. Wireless technologies, either mud pulses or electromagnetic transmission (EM), can be utilized to transmit signals from MEMS sensors in a harsh locations. Until wireless signal transmission is available, a logging unit in a more protected down hole location could be removed and the

data downloaded, eliminating the need for expensive down well cabling. Or, a data collection unit could be lowered into the well to acquire the stored data.

Harsh environment MEMS have be previously fabricated and tested in superheated steam at temperatures up to 600 °C for short durations. They have also demonstrated high shock resilience, up to 64,000 G, indicating that they would survive the shock applied to geothermal well casings during installation [16].

1.7   Dissertation Overview

Chapter 2 describes the materials testing that was conducted to determine geothermal well compatible materials. It describes two experiments, water and brine testing, that were conducted to determine certain MEMS materials survivability. It goes into detail on the corrosion and oxidation theory of the materials selected for testing, the preparation and fabrication of tested samples, the testing procedures, and the post-exposure analysis techniques used.

Chapter 3 provides an overview of the state-of-the-art temperature sensing methods currently in use in many different applications including geothermal well monitoring. This chapter also includes the design, modeling, fabrication, and testing of a harsh environment compatible out-of-plane MEMS temperature sensor. This sensor is modeled after non-harsh environment compatible, capacitive, temperature sensors. This sensor shows that the more common out-of-plane temperature sensor designs can be made for use in harsh environments.

Chapter 4 compares the advantages and disadvantages of out-of-plane sensing devices to the in-plane devices from Chapter 3. It then details the design process for a novel in-plane temperature sensor, which includes some basic analytical modeling and more extensive ANSYS finite element modeling. These modeling techniques were used to optimize sensor linearity and signal output. A detailed account of the in-plane temperature sensor fabrication is also shown. Process flows are used in conjunction with SEM images to describe many techniques that were used to achieve the final sensors. The fabrication of the initial thin SiC device layer sensors, and the final thick SiC device layer sensors, are presented. Test set-ups and results are described to show sensor performance, which is compared to the theoretical models generated earlier in the chapter.

The final chapter, Chapter 5, summarizes the results described in the earlier chapters and compares the theoretical results to the achieved sensor performance. It also discusses the future work that will help take MEMS geothermal sensors from a test environment to their application in active geothermal systems.

Chapter 2

Exposure Testing in Simulated Geothermal Environments

Appropriate materials must be used in the design of any sensor. Before temperature sensors can be designed for the down hole geothermal harsh environment, exposure tests are required to determine materials survival. These tests are used to determine the best materials for the design of the device layer, its substrate, and the encapsulation.

Harsh environment materials were exposed to simulated geothermal environments in Tuttle pressure vessels for long duration testing. Tests were conducted in both sub- and supercritical water and sub-critical salt water simulated brine. Water testing was conducted in four phases of water by changing the applied pressure and temperature. The pressure and temperature conditions were chosen to expose potential geothermal sensing materials to liquid, vapor, super critical and critical point water. Tests ranging from 1 to 100 hours were conducted in these water environments to look at material degradation and determine a suitable method of sensor testing once the sensors were fabricated and tested.

The brine testing was conducted in a NaCl solution to simulate the corrosive salt water environment seen in many geothermal wells. These tests were conducted for longer durations of 100, 200, and 300 hours. These tests were conducted in a sub-critical liquid environment as the salts are immiscible in supercritical fluids.
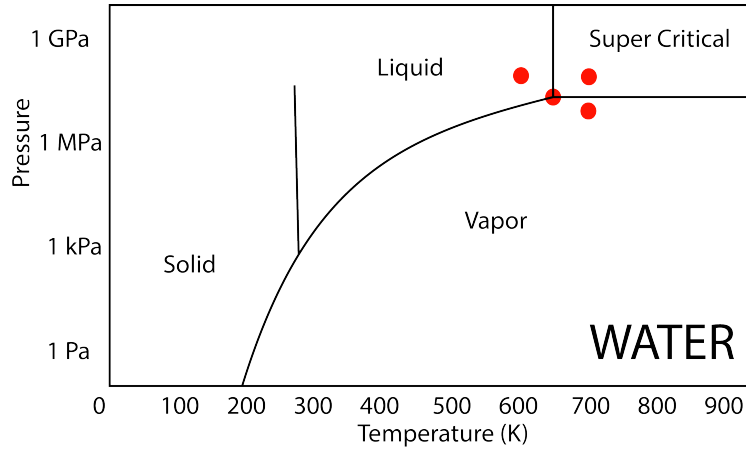
Figure 2.1. Water phase diagram with the four exposure pressure and temperature environments for water exposure testing shown with red dots.

2.1 Theory

The main purpose of materials testing is to observe the material degradation to determine the best sensor materials. Degradation could occur in the form of oxidation, reduction, layer delamination, surface roughening, and ion diffusion.

While many studies have been conducted to determine the corrosion rates of sintered and CVD SiC in supercritical water, [17], [18], [19], [20], [21], none of these studies investigated crystalline 4H-SiC, sapphire, or AlN. All of these are harsh environment MEMS materials that may be useful for MEMS encapsulation or device layers. While it was not expected that AlN would survive the geothermal environment, by exposing the AlN thin film, its survivability within the harsh environment in the event of encapsulation failure can be studied. Other harsh environment materials including single crystal and micro-crystalline synthetic diamond hold potential for MEMS encapsulation. In this section, the theoretical materials degradation mechanisms are discussed for both the water and brine environments for each of the tested materials.

2.1.1 Si Degradation Physics

Silicon is the standard substrate material for both MEMS and IC production. Silicon processing is well established and is suitable for applications below 200 °C as limited by electronic properties. As a structural material, silicon has been shown to survive high temperatures, supporting platinum heater traces up to 1000 °C [22]. However, silicon is known to oxidize in high temperature environments, starting around 800 °C. Both wet and dry oxidation reactions, shown in Equation 2.1 and Equation 2.2, are common for silicon. The Deal-Grove model shown in Equation 2.3, based on Fick's 1st law and gas transport phenomenon, describes the oxidation physics where constants A and B are based on envi-

10

ronmental parameters limiting the oxidation reaction [23]. The standard Deal-Grove model describes both wet and dry oxidation processes for Si in pure oxygen or water vapor. This model uses both gas kinetics and diffusion equations to describe the transport of oxygen to the oxide surface, oxygen in-diffusion through the oxide to the Si/SiO_2 interface, the reaction of oxygen with the Si, the out-diffusion of reaction gases, and the removal of product gases from the outer oxide surface. This oxide may be stable and serve as a passivation layer in some environments as long as the oxide is not etched from the surface.

$$Si + O_2 \rightarrow SiO_2 \tag{2.1}$$

$$Si + 2H_2O \rightarrow SiO_2 + 2H_2(g) \tag{2.2}$$
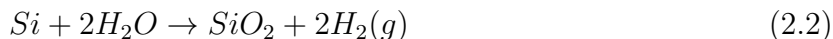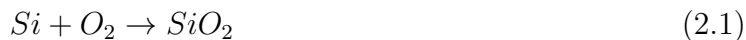
$$t = \frac{X_o^2}{B} + \frac{X_o}{B/A} \tag{2.3}$$

In addition to being oxidized in air and water, silicon is known to be etched by chlorides by the reaction shown in Equation 2.4 [24].

$$4Cl + Si \rightarrow SiCl_4 \tag{2.4}$$

The limited chemical resistance of Si makes it a favorable material to use for experimental controls.

2.1.2   SiC Degradation Physics

While SiC is often considered to be a chemically inert material, with great promise for many harsh environment applications, SiC can still be etched and will oxidize under certain prescribed conditions. The ability to be etched and grow an oxide are positive attributes from a fabrication standpoint in that it allows for patterning devices and growing oxide gates. However, from an encapsulation standpoint, these two attributes can lead to the weakening of a protective layer leaving sensors exposed and leading to failure. While some corrosion and oxidation may not pose a problem to an encapsulation layer, significant material degradation is not acceptable.

The main factors that influence the corrosion of SiC in water are the oxygen content of the water and the SiC fabrication method. Higher oxygen content has been shown to increase corrosion of SiC in water environments. Corrosion of sintered SiC is higher than that of CVD SiC due to the increased free Si bonds. The Si reacts with the oxygen in the water by either the reaction shown in Equation 2.5 [25], to form a silica or based on a modified Deal-Grove model shown in Equation 2.3 [26]. The modified Deal-Grove model describes the H_2O/SiC surface reaction as shown in Equation 2.6. The modified oxidation process incorporates the out gas diffusion of CO and H_2 that is not included in the standard oxidation process of Si.

$$SiC + 2H_2O = SiO_2 + CH_4 \tag{2.5}$$

$$SiC + 3H_2O \rightarrow SiO_2 + CO + 3H_2 \tag{2.6}$$
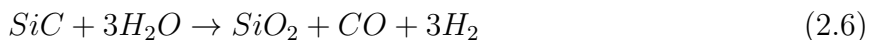
In many environments the grown silica layer would act as a protective layer, passivating the SiC underneath. This layer is non-porous under ideal grown conditions, and prevents further oxidation. However, in a high temperature water environment, this passivation layer can dissolve into the water by the reaction shown in Equation 2.7. This allows for further corrosion of the SiC. Islands of carbon have been found to form on the surface of the SiC under the oxidized layer when free carbon bonds meet and bond with other carbon atoms rather than oxygen to form CO or CO_2 in place of the removed Si atoms [27]. Corrosion measured by weight loss of 20 ppb to 32 ppm have been shown with sintered SiC in water at 290 °C. This range is based on different oxygen levels in the tested water environment [20],[21]. CVD SiC has much higher corrosion resistance due to the reduced free Si reaction sites. Corrosion is seen to preferentially attack at grain boundaries and at pores when tested at 360 °C in pure water [18]. When exposed to water at 450 °C and 45 MPa, the formation of an amorphous SiO_2 layer has been observed [28]. Similar degradation patterns can be seen with other CVD SiC studies as well as SiC fibers, powders, and nanowires [29],[30].

$$SiO_2(s) + 2H_2O(g) = Si(OH)_4(g) \tag{2.7}$$
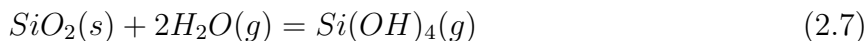
Single crystal SiC may serve as a more robust encapsulation material because this corrosion occurs along the grain boundaries due to the free Si bonds. While single crystal SiC is most easily available in substrate form, there has been some work done with the growth of single crystal SiC on Si [31]. This may prove to be a feasible encapsulation technique if the SiC is shown to survive the supercritical water environment.

In addition to being potentially etched by water, SiC is also known to be etched by dry chlorine above 1000 °C by the reaction shown in Equation 2.8, [32]. Chlorine can still be an effective etching gas at lower temperatures when used with an inductively coupled argon plasma [33]. This may pose a problem for SiC when exposed to the chlorine salts in the geothermal environment.

$$SiC + 2Cl_2 = SiCl_4 + C \tag{2.8}$$

Fluorine can also be used as an effective etching gas. Reactive ion etching (RIE) couples both physical and chemical etching regimes. The etch rates of fluorine plasma was investigated by Pan at Intel to experimentally determine the chemical reactions between SiC and the fluorine [34]. A combination of silicon reacting with fluorine, shown in Equation 2.9, and carbon with oxygen, shown in Equation 2.10, yields an overall chemical reaction, Equation 2.11, describing the etching of the SiC.

$$Si + 4F \rightarrow SiF_4 \tag{2.9}$$

$$C + xO \rightarrow (CO, CO_2) \tag{2.10}$$

$$SiC + xF + yO \rightarrow SiF_4 + (CO, CO_2) \tag{2.11}$$
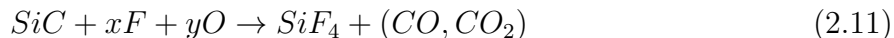
2.1.3   Sapphire Degradation Physics

Sapphire, or single crystal alumina, Al_2O_3, is an aluminum oxide that is generally considered insoluble in water. However, in sub-critical water conditions (335 °C, 21.5 MPa for 500 hours), just below the critical point, mass loss of -0.5 wt.% has been observed in sintered C799 alumina [25]. This effect was reduced and was determined unmeasurable in supercritical conditions. This reduced corrosion in supercritical water is due to the drop in pressure seen in the supercritical phase. The high pressure and slightly lower pressure in the sub-critical phase allows water to keep ionic compounds in solution, making it ideal for ionic reactions. While alumina was etched in these conditions, this study was conducted with poly-crystalline α-Alumina. It is reported that there was preferential intergranular corrosion, which would be reduced with single crystal sapphire.

Sapphire corrosion and etching is know to occur in fluorine, hydrofluoric acid, and phosphoric acid. Sapphire has been etched with both H_2SO_4 and more slowly with a 3:1 volume mixed solution of H_2SO_4:H_3PO_4 [35],[36]. While this will not pose a problem with water testing, this may reduce sapphire's potential as an encapsulation material in geothermal brine containing sulfides and fluorides.

Chlorine-based plasma etching chemistry (BCl_3) can be used for sapphire etching with relatively slow etch rates of 100 nm/min. This process requires high power inputs of up to 800 W [37]. Based on the etch power required and the strict photoresist processes parameters required to achieve a reliable etch mask, there is likely a large amount of physical etching in this process and minimal chemical attack from the chlorine ions. This type of physical bombardment would not be seen in a geothermal well. Single crystal sapphire has been used as a container for molten NaCl due to its chemical stability [38]. Survivability in this environment indicates that sapphire has a strong potential to survive the NaCl in the geothermal environment.

2.1.4   Vitreous Carbon Degradation Physics

Vitreous carbon, or glassy carbon, is the carbonized form of certain cross-linked polymers. Once fabricated, it has bonding similar to that of graphite within the graphite sheet, i.e. covalent bonds with 1.42 Å spacing. However, while graphite has Van der Waals forces holding the sheets together, vitreous carbon has some cross linking between the layers. This cross linking is not complete like that of a diamond structure, but there is enough cross linking to increase hardness and reduce gas permeability. Porosity can be reduced to the size that the films will prevent the permeability of helium. High purity vitreous carbon also has a very low oxidation rate compared to close-grained graphite and baked carbons. The carbonization process must be very controlled to ensure that the polymer does not graphitize when heated [39].

Various photoresists have been used as the polymer for graphitization. This allows for the patterning of vitreous carbon structures before the carbonization process [40],[41],[42]. One recipe for using AZ4330 photoresist shows the polymer being pyrolyzed at 900 °C while

flowing forming gas. Another study used both AZ4330 and OCG-825 in the fabrication of glassy carbon [43]. These films were pyrolyzed with N_2 rather than forming gas. The films were all found to be non-porous. They were pyrolyzed at temperatures ranging from 600 °C to 1100 °C for 1 hour. The higher temperature-formed films behaved electrochemically like glassy carbon electrodes. Other polymers used in the fabrication of vitreous carbon include "Tammer F_3", phenolformaldehyde resin and furfurylalcholmaleic acid polymer [44].

Most patterning and processing that is done with vitreous carbon is done before the carbonization process. Vitreous carbon is treated like diamond and is machined using grinding processes for post carbonization processing. Some etching processes have been developed to etch carbonized carbon. A process of anodizing the film in 0.1 M NaOH has been shown to etch based on the electrochemistry shown in Equation 2.12 and Equation 2.13 where {C} is the carbon removed and C(s)OH(ads) is the chemisorbed -OH on the surface of the glassy carbon [45].

$$C(s) + OH^-(aq) \rightarrow C(s)OH(ads) + e^- \tag{2.12}$$

$$4C(s)OH(ads, int) \rightarrow 4\{C\} + 2H_2O + O_2 \tag{2.13}$$
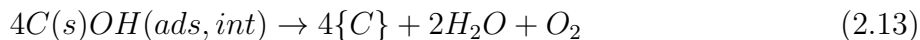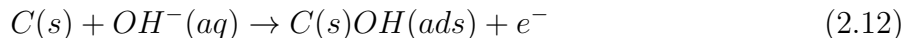
Glassy carbon has been shown to be stable in some chlorine compounds when used as an electrode. At 450 °C glassy carbon electrodes have been shown to be stable in 60-40 mol. % $ZnCl_2NaCl$ between 0.23 and 1.8 volts with zinc as the opposing electrode [46]. Other studies and pattens have shown the stability of carbon electrodes in $NaALCL_4$ salts below the chlorine evolution potential [47].

2.1.5   Diamond Degradation Physics

Single-crystal diamond is considered to be one of the strongest materials, with a Mohr's hardness of 10 and complete covalent C-C bonds on all carbon atoms less those on the terminating face. These strong bonds make diamonds chemically very inert and difficult to oxidize. Synthetic diamond has been used in supercritical water reactors as a protective coating [48] and as windows in high temperature/pressure molten salt reactors [49].

Oxygen plasma at very high frequency has been shown to etch single crystal diamond in low pressure environments [50]. Etching plasmas may be modified to include SF_6 or some other fluorine containing gas [51]. Synthetic diamond has been shown to oxidize or graphitize at 750 K and 1100 K respectively [52]. These oxidation rates decrease with decreasing CH_4/H_2 ratios during growth due to increased surface energy of 293-285 kJ $mol^{-1}K^{-1}$ [53]. Similar to the behaviors seen with other materials discussed, there is preferential oxidation at grain boundary interfaces. While the oxidation process is not fully understood, it is surmised that the oxygen penetrates the diamond surface and creates a dipole. At a high enough temperature, the oxygen is able to form a more stable bond with the carbon. The

{111} planes have been shown to oxidize more readily than the looser packed {220} planes [52].

2.1.6 Aluminum Nitride Degradation Physics

Aluminum Nitride (AlN) has shown promise as a high temperature material for sensor device layers. It has been tested for ultrasound transmission and reception up to 1100 °C in argon [54] and can be integrated with high temperature circuits for reduced system complexity. While AlN has some promising properties as a device layer, it will likely not serve as an encapsulation material as it is known to allow oxygen diffusion [55]. AlN is known to oxidize to form a layer of Al_2O_3 above 1000 °C [56]. Chlorine-based plasma etches are known to etch AlN [57]. This indicates that AlN would likely not survive in a chlorine based salt environment at elevated temperatures. However, AlN has been used as an encapsulation layer in 0.1 M KCl brine to protect Tb-Fe films [58]. Even if the AlN is not an appropriate encapsulation material for geothermal brine, it is important to test potential device materials to determine their survivability and understand their potential reactions in the event of encapsulation failure.

2.2 Supercritical Water Testing

Initial tests were conducted in liquid, vapor, critical point, and supercritical water to reduce the materials that needed to be exposed in the more expensive brine tests. The water used was not deoxygenated, increasing corrosiveness, and contained Ni, Fe, Nb, and Rh ions leached from the steal test vessels. These contaminants are similar to those which would be seen in steel pipes in geothermal wells.

2.2.1 Exposed Materials

Water exposure testing was conducted on six different sample types shown in Figure 2.2. Two silicon based samples, one bare silicon substrate, and one silicon sample with AlN and Pt, were tested as controls in the geothermal environment to verify the necessity of specialized harsh environment materials. The harsh environment materials that were exposed were SiC, Al_2O_3, AlN, amorphous SiC (a-SiC), and Pt. While a wider array of materials may survive the environmental pressures and temperatures, these materials were selected for testing because of their potential abilities to survive within the corrosive water environment or their promise for new MEMS materials. Select material properties are summarized in Table 2.2.1 [59]. The harsh environment materials bond energies are high compared to that of the Si control sample used in the experiment. All of these materials would have little to no oxidation at the maximum temperature in the experiment, 427°C. However, due

15

to the free ions in high temperature water, local oxidation and corrosion may degrade the samples at this lower temperature by exceeding the materials bond energy. Bond energy is one indicator of corrosion resistance; however, other factors including the materials' physical composition (single-crystalline versus poly-crystalline), defect density, and surrounding environment chemistry play an important role in determining corrosion rates.
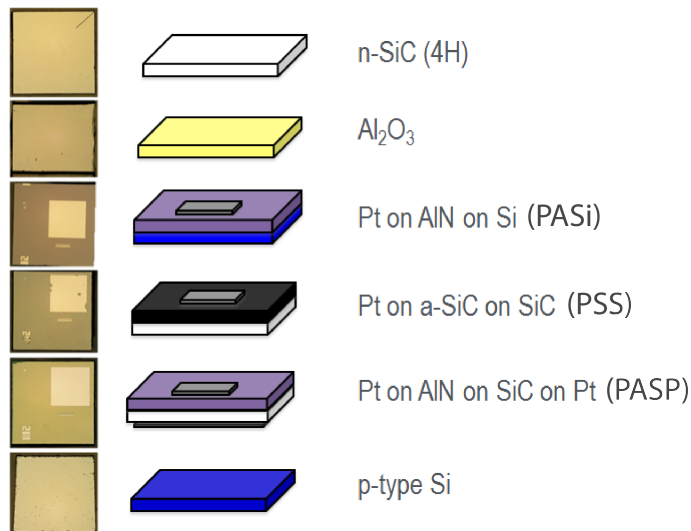
Figure 2.2. The six samples exposed to the geothermal testing environment. (Left) Fabricated top views of each sample type. (Right) Isometric graphic of corresponding sample.

Material	Chemical Bond Type	Bond Energy at 25 °C (kj/mol)	Melting Temperature
Silicon	Covalent	222	1420
Sapphire	Ionic/Covalent	595.65	2050
4H-SiC	Covalent	318	2030
AlN	Covalent	279.8	2470

Table 2.1. Summary of tested materials properties. Note: SiC is sublimation temperature

Each of the sample types has some fabrication steps taken prior to exposure. Two different single crystal 4H-SiC wafers from CREE Inc. were used for the exposure tests. C-axis sapphire wafers from MTI corporation were purchased and diced. These bare substrate materials were coated with photoresist before dicing and cleaning. The 500 nm AlN layer was sputtered using an Endeavor AT radial multi-chamber sputter system to achieve highly oriented c-axis AlN for the layers deposited on the Si and SiC substrates. The 300 nm a-SiC film was deposited at room temperature using the directional ion beam assisted deposition (IBAD) tool used for harsh environment encapsulation. All of the Pt was patterned using a lift-off process. The Pt layers on both SiC substrates were sputtered to 80 nm thick with a 10 nm thick chrome adhesion layer. The Pt layers on the Si samples were 100 nm thick with

a chrome adhesion layer using a slightly different sputtering recipe. These materials were diced to size (approximately 5 mm by 5 mm) and weighed on a scale with 5-point Mettler balance with 10 μgrams accuracy.

2.2.2   Experimental Set-Up

The samples were loaded into a sample holder shown in Figure 2.3. A water jet tool was used to cut the holder from sheets of 316 stainless steel. This medical grade stainless steel is alloyed to survive within corrosive environments. The holder was cut in three layered sections. These three sections allowed for simple fabrication within the small footprint size alloted by the Tuttle pressure vessel bore of $\frac{1}{4}$". The bottom section provided a backing for the samples to rest. The middle section acted as a spacer to separate each sample type. The upper section behaved as a window to allow environmental exposure. The three sections were held together by size 2 stainless steel screws and military grade, chemically treated, nuts.
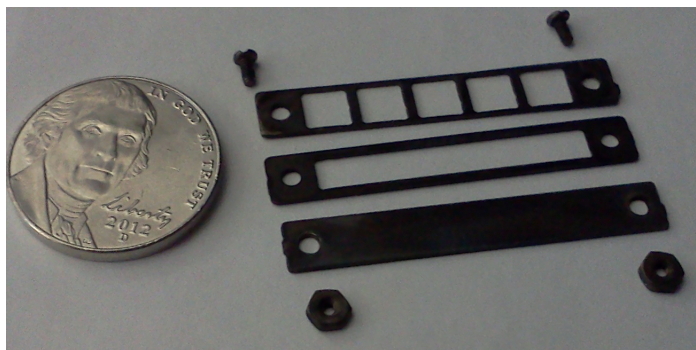
Figure 2.3. Fabricated stainless steel sample holder for exposure testing. A U.S. nickel is used to show scale.

The assembled sample holders were loaded into Tuttle pressure vessels, which were filled with water to create each of the four pressure and temperature defined testing environments. The pressure vessel was sealed using two conical interfaces with slightly mismatched angles as shown in Figure 2.4. The valve cone is made from a softer material, which allows slight deformation during the tightening process. This makes for a reliable pressure seal. This type of pressure vessel was originally designed by Tuttle for studies on silicates with water [60].

Once sealed, the vessel was connected to a waterline to pressurize the fluid within the vessel. The testing equipment used at the University of Manoa has water hook-ups for 6 pressure vessels in parallel shown schematically in Figure 2.5. This allows for 6 independent pressure and temperature experiments. The water pressure is controlled in the main line by both an automatic pump for large pressure changes, and a manual piston/cylinder fluid volume for fine tuning. The temperatures are controlled by individual heaters with temperature controller thermocouples recessed into the vessel at the closed end. This recessed

Figure 2.4. Tuttle pressure vessel interface.
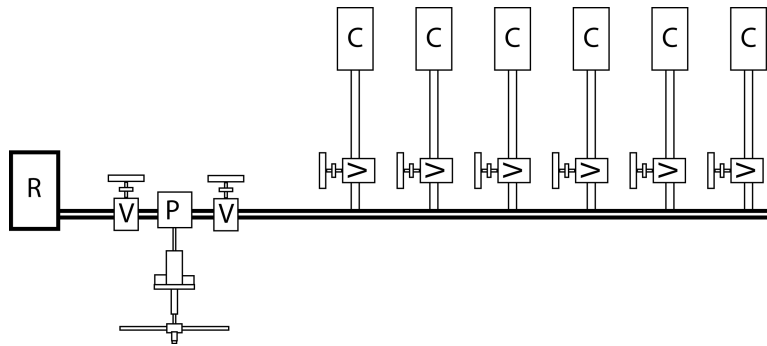
Figure 2.5. Schematic of test set-up in Professor Julia Hammer's laboratory. (C) Pressure Vessel (P) Pump (R) Water Reservoir (V) Valve.

pocket allows for the monitoring of the temperature closer to the samples precise location within the test setup. Each pressure vessel can be separated from the main line using an isolation valve. Pressure and temperature independence of each vessel from the main line allows for simultaneous execution of multiple exposure time experiments.

In this system, there is only a pressure gauge on the main pressure line. As such, each pressure vessel was pressure checked to ensure proper sealing before testing began. A pressure check was conducted by raising the pressure line to the desired pressure, isolating the desired pressure vessel, waiting for set time, and then reopening the isolation valve. A longer check period was afforded to tests with higher pressures. If the main pressure line value dropped when the valve was reopened, it indicated a leak in the vessel. These leaks were addressed by re-tightening the vessel seals before long duration testing began.

The longest exposure tests were conducted at the critical point for water as these were the pressure and temperature points defined by the Department of Energy. Shorter tests in liquid (327 °C, 100 MPa), supercritical (427 °C, 100 MPa), and vapor (427 °C, 10 MPa) environments were conducted to form a more complete picture of how a variety of geothermal environments affect MEMS materials. This allowed for a more in depth investigation of the mechanisms of corrosion. Tests of 1, 5, 20, 50, and 100 hours were conducted at the critical point exposing the SiC and sapphire substrates, and all three of the layered samples to include a-SiC, AlN, and the metal layers. Tests of 1, 5, 10, and 20 hours were conducted at the other pressure/temperature conditions exposing all of the bare substrate materials.

Tests longer than 20 hours were not conducted due to test facility time constrains and the substantial silicon degradation in super critical water for 20 hours.

2.2.3 Water Exposure Testing Results

Post exposure analysis began with a visual sample inspection. This inspection revealed platinum delamination. Next, the samples were weighed to determine any weight loss due to the environmental exposure. Other forms of sample processing included x-ray photoluminescence spectroscopy (XPS) analysis to determine the sample composition. This technique was used to determine any ion diffusion and oxide growth. SEM imagery was used to optically determine the mechanisms of corrosion. Finally, white light interferometry was used to determine the depth of surface roughening when appropriate.

Platinum Delamination

Two similar platinum depositions were utilized in test sample fabrication as described in the experiment set-up section. For tests longer than 5 hours both the Pt with Cr adhesion layer on AlN and Pt on a-SiC delaminated. Figure 2.6 shows one example of this phenomenon. The platinum layer appeared to be unaltered other than the delamination; however, due to its thin fragile state post delamination, no characterization tests could be conducted on the metal.
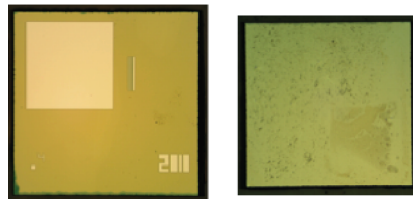
Figure 2.6. (Left) Pt on AlN on SiC before exposure testing. Same sample post 5 hours in the critical point water condition.

Mass Loss Analysis

The mass losses for SiC, sapphire, and Si in all four environments are shown in Figures 2.7, 2.8 2.9 and 2.10. The silicon mass loss was significantly larger than that of the SiC or sapphire samples, whose mass losses were unmeasurable in all phases of the testing. Mass loss in the super critical regime was the most extreme and led to silicon mass loss of up to almost 80% in 20 hours. The silicon substrate material mass loss in the liquid, vapor, and super critical environments can be seen in Figure 2.11.
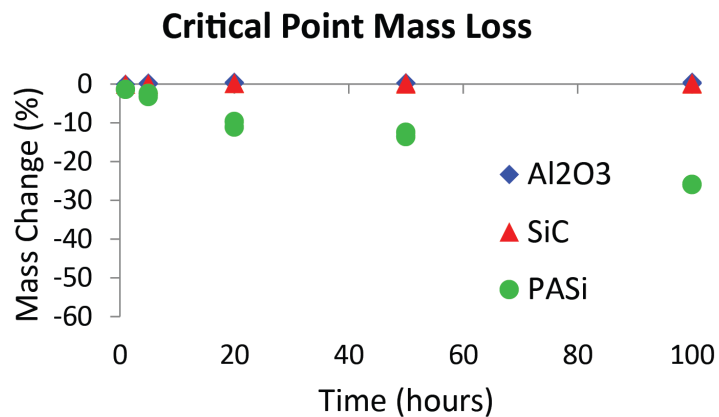
Figure 2.7. Mass loss of SiC, sapphire, and Si over 100 hours of exposure testing at the critical point of water.
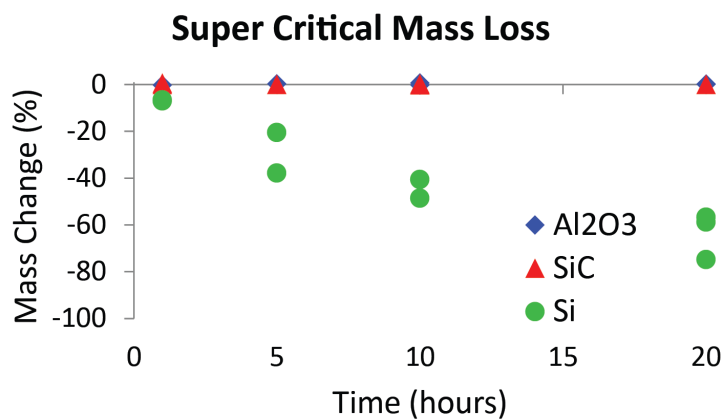
Figure 2.8. Mass loss of SiC, sapphire, and Si over 20 hours of exposure testing in super critical water.
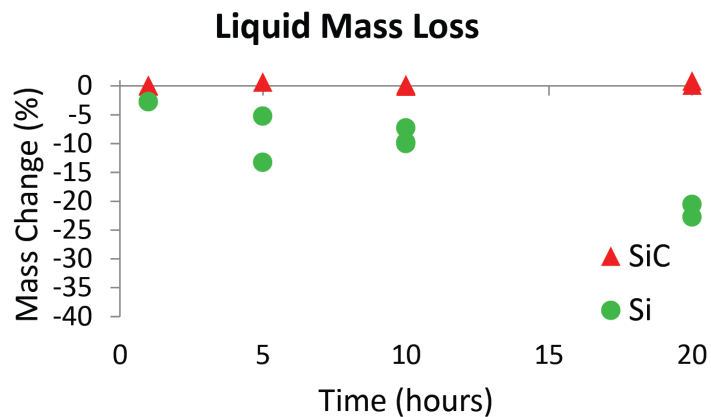
Figure 2.9. Mass loss of SiC and Si over 20 hours of exposure testing in liquid phase water.
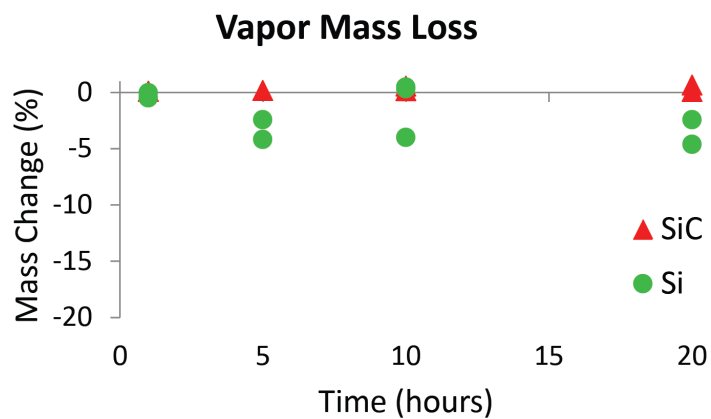
Figure 2.10. Mass loss of SiC and Si over 20 hours of exposure testing in vapor phase water.
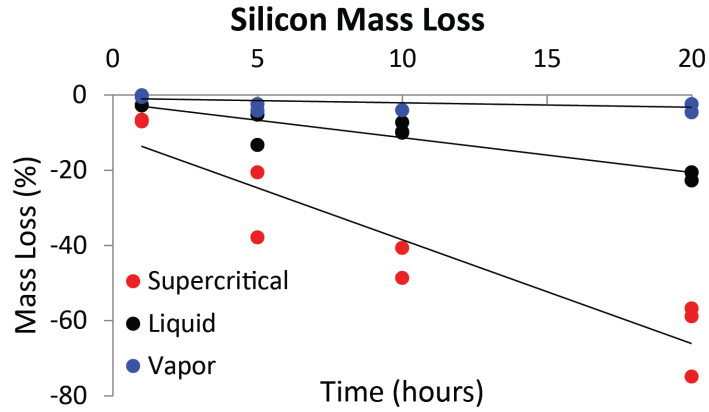
Figure 2.11. Mass loss of silicon in vapor, liquid, and super critical water.

Optical Inspection and Analysis

SEM images of the surfaces of some of the exposed samples were taken in an attempt to determine the degradation mechanism. Images of the silicon sample in liquid and supercritical water for 5 hours of exposure are shown in Figure 2.12. Both environments appear to have pitted the surfaces of the silicon samples. The supercritical sample has shallower pits; however, there is a large weight loss associated with this sample, so is it likely that the supercritical environment was more effective at removing the oxidation layer formed at each of the pitting sites. The liquid sample has deeper pits that are more distinct.

Silicon after 5 hours in
Supercritical Environment

Silicon after 5 hours in
Liquid Environment
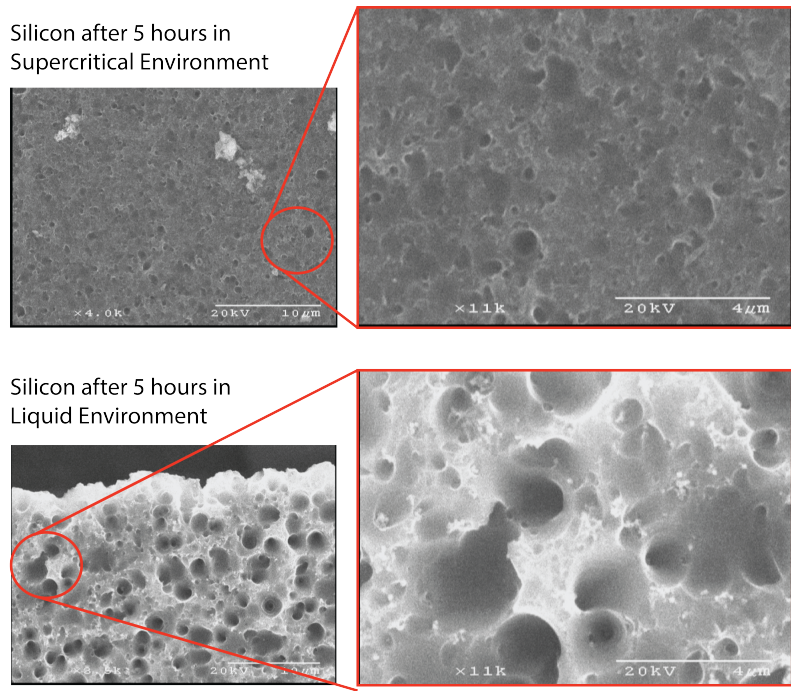
Figure 2.12. SEM images of the pitting of 2 silicon samples exposed for 5 hours in the supercritical water (top) or liquid water (bottom) environment.

A SEM of the AlN thin film deposited on 4H-SiC is shown in Figure 2.13. After 1 hour of exposure the layer begins to degrade in small patches on the surface. SEM images of the 5 and 50 hour samples show that the film continues to degrade in this nonuniform fashion. The AlN was deposited on Si, which is know to be etched by the water environments, so it can be seen that the layer has been removed from certain areas of the die. There are residual patches of AlN on the surface of the dies even after 50 hours or exposure. The AlN etching is not uniform over the die. Etching occurred more readily on the edges of the die than in the center. After 50 hours of exposure, minimal AlN remains and there is significant Si etching on the underlying layer. Sputter XPS was used to determine the AlN lifetime in the critical point water environment based on the thickness of the layer after exposure.

Etched Si

no exposure   1 hour   5 hours   50 hours

AlN Layer
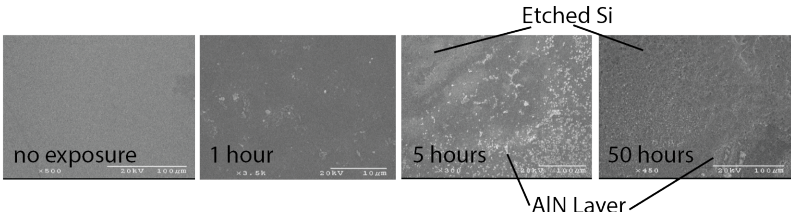
Figure 2.13. SEM images of the AlN thin film before exposure in critical point water and after 1, 5, and 50 hours of testing.

SEM images of the sapphire and SiC samples tested at the critical point for 100 hours are shown in Figure 2.30 and Figure 2.17, respectively. Both of these images show some surface wear; however, it is not as dramatic as that seen in the silicon samples after only 5 hours of testing. This is why there is no detectable weight change. White light interferometry was used to determine the thickness of the sapphire surface roughening. Roughness data was measured to show the increase in surface degratation with exposure time. However, this phenomena appears to be reducing with time as shown in the concavity of the plot in Figure 2.31. Similar surface roughening behavior can be seen on the sapphire sample surface in the super critical water environment as shown in Figure 2.16.
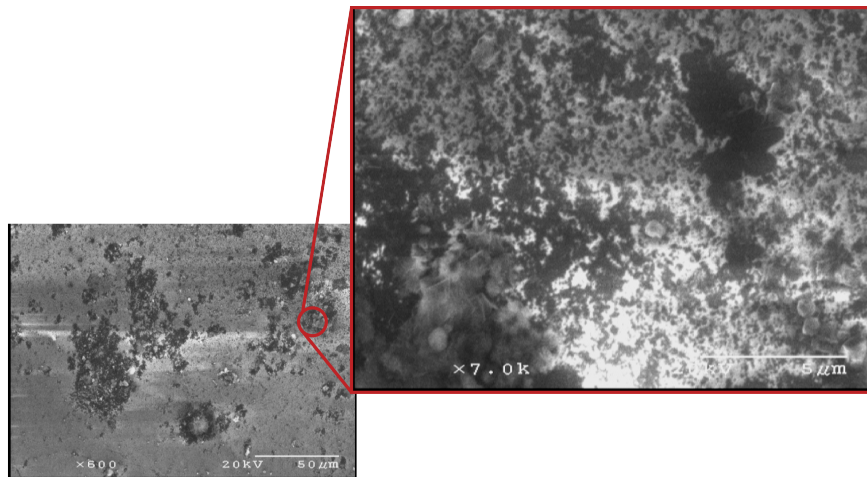
Figure 2.14. SEM images of the sapphire sample after 100 hours of exposure testing at the critical point.
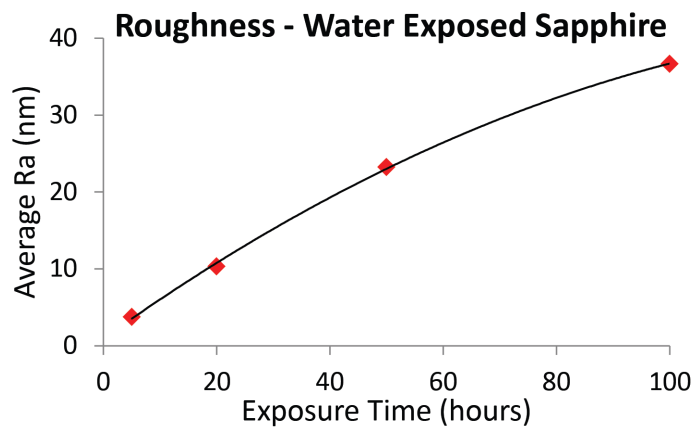
Figure 2.15. Roughness measurements for sapphire samples for 5 to 100 hours of exposure.

24
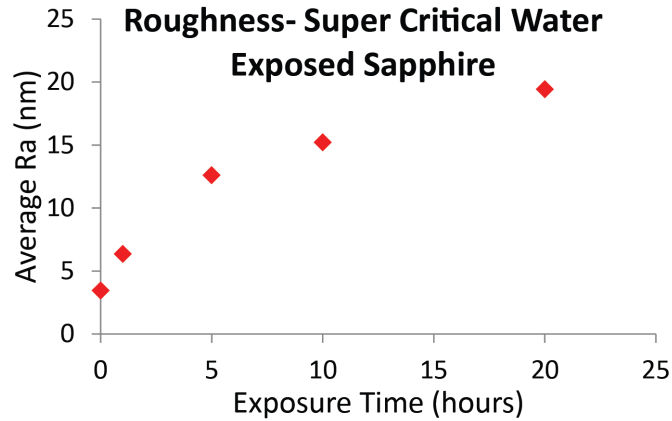
Figure 2.16. Roughness measurements for sapphire samples for 5 to 100 hours of exposure.
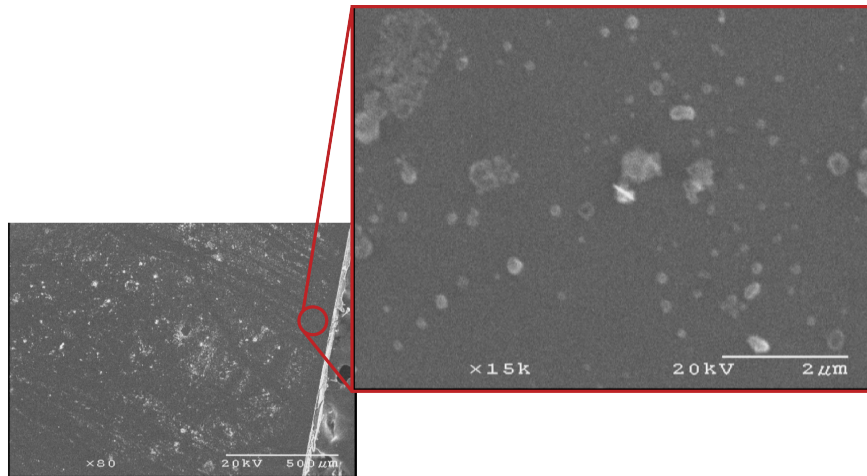
Figure 2.17. SEM images of the 4H-SiC sample after 100 hours of exposure testing at the critical point.

XPS Analysis

X-ray photoluminescence (XPS) analysis was conducted in conjunction with a sputtering tool to determine the sample chemical composition through many of the exposed samples. Sputtering of 5-50 nm step heights were resolved based on the SiO_2 sputter etch rates.

Aluminum Nitride and Amorphous SiC Degradation   The first finding from the XPS analysis was the complete etching of the AlN thin film. The surface scan of the 100 hour critical point exposure tests showed no Al or N species. Figure 2.18 shows the loss of the

AlN thin film layer versus exposure time. After the same 100 hour tests there was also no trace of the a-SiC thin film layer. The a-SiC can be identified by a slight Al doped signature that results from the Al in the IBAD chamber. Scans of the 5, 10, 20, and 100 hour exposed a-SiC layer show no traces of the Al peak.
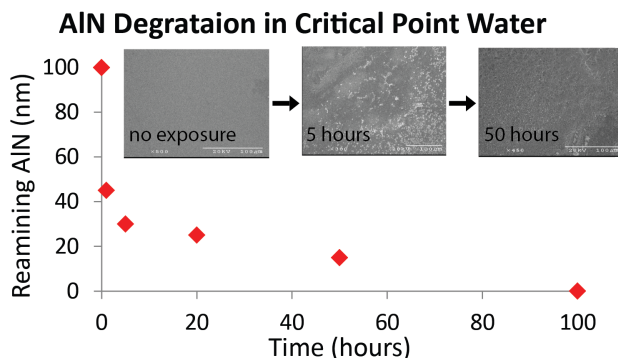
Figure 2.18. AlN thin film degradation over 100 hours of testing. An exponential decay trend line is shown with the experimental data. Before and after images of the 5 mm x 5 mm die are overlayed on the plot.

Silicon Carbide Oxidation and Ion Diffusion   The blank SiC samples are one of the highest interest as the exposure testing was conducted to determine sensor packaging materials and SiC is readily available as a substrate material. The SiC samples were XPS depth analyzed for oxide growth rates and ion diffusion rates. Samples were tested in 1 mm^2 areas for chemical compositions. That area was then sputtered in small increments before each following scan to generate a depth profile.

The initial surface scan of a 100 hour critical point tested revealed unexpected ions such as Fe, Nb, Rh, and Nd in addition to the expected Ni known to be present in the water. These four elements are used in treating the steel used for manufacturing the Tuttle pressure vessel. A scan showing the surface Fe and Ni is shown in Figure 2.19. The sample's surface was cleaned in ethanol in a sonicator for 30 minutes. Post-cleaning, these unexpected elements were no longer seen in the XPS surface scans. This indicates that the Fe, Nb, Rh and Nd did not diffuse into the SiC sample. The initial surface scan reveals Ni and a transitional silicon oxide (SiO_x). These surface scans also showed the expected Si, O_2 and Ni binding energies. Interestingly there was also a carbon peak. The carbon peak seen in Figure 2.20 shows the binding energies of elemental carbon, carbon from SiC, carbon as it is known to be found with SiO_2, and the formation of hydrocarbons and silicon carboxide. The exact chemistry of the hydrocarbon formation is not entirely clear; however, it is likely that the free ions in the critical point water caused local reactions with the SiC to form SiO_2 and C. Both the out-diffusion of oxidation reaction products and product removal are hindered by the surrounding static water more than that of the ideal oxidation vapor flow. This would lead to the buildup of reaction products within the sample. Thus, we do not see the clean SiO_2 layer as predicted by the theoretical modeling of the SiC oxidation process. These free carbon atoms are shown in the scan in elemental form indicating a graphitized surface;

26

however, they also bond with oxygen to form hydrocarbon chains. The silicon carboxide would also be formed in a similar way with the addition of some silicon atoms. These larger molecules were not expected on the sample surface, and while scientifically interesting, they were only found on the surface. For encapsulation purposes, effects that degrade through the sample are of greater consequence.

While some material degradation is tolerable for an encapsulation or substrate material, that damage must be asymptotic to prevent total encapsulant failure. The samples were sputtered in 5, 10, and/or 15 nm depth increments to determine the depth of sample degradation. The sputtering depth rate was calculated based on the sputtering rate of SiO_2. The hydrocarbons, elemental carbon, and silicon carboxide were only found on the top 10 nm of the samples. However, the SiO_2 and the Ni contamination continued through the SiC sample. At each depth step XPS peak scans were taken. The strength of the Ni and SiO_2 signals decreased with depth into the sample. The oxide depth was determined to be reached when the signal was indistinguishable from the scan noise. Over the 100 hours, the oxidation reached an average depth of approximately 150 nm from the surface of the SiC samples, as seen in the depth scans shown in Figure 2.21. The SiC samples exposed for 50 hours showed oxidation to 65 nm. This oxidation depth is significantly more than the SiC native oxide of betweeen 0.2 nm to 1.3 nm as seen in the literature [61], [62]. This increase in degradation depth at these exposure times indicates that the SiC will continue to degrade with increased exposure time. Nickel ions were able to penetrate to a depth of 50 nm in the SiC after 100 hours of exposure. This was an increase of 15 nm from the 35 nm Ni penetration depth with the 50 hour exposed SiC sample.
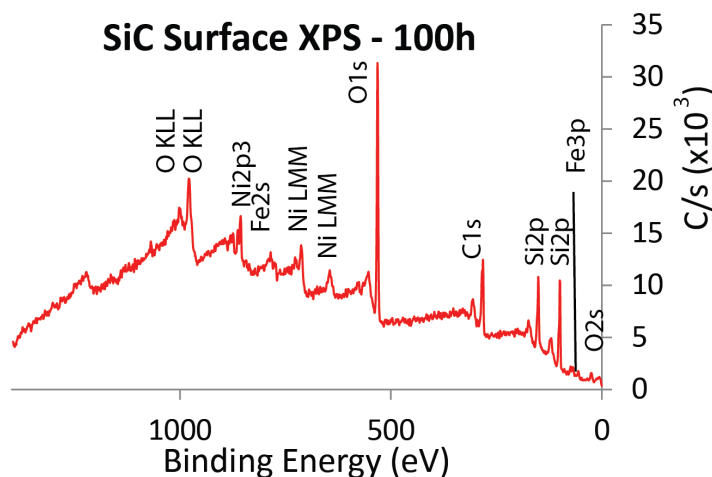
Figure 2.19. Surface XPS data of a 100 hour exposed SiC sample before cleaning. Both nickel and iron are observed on the surface.
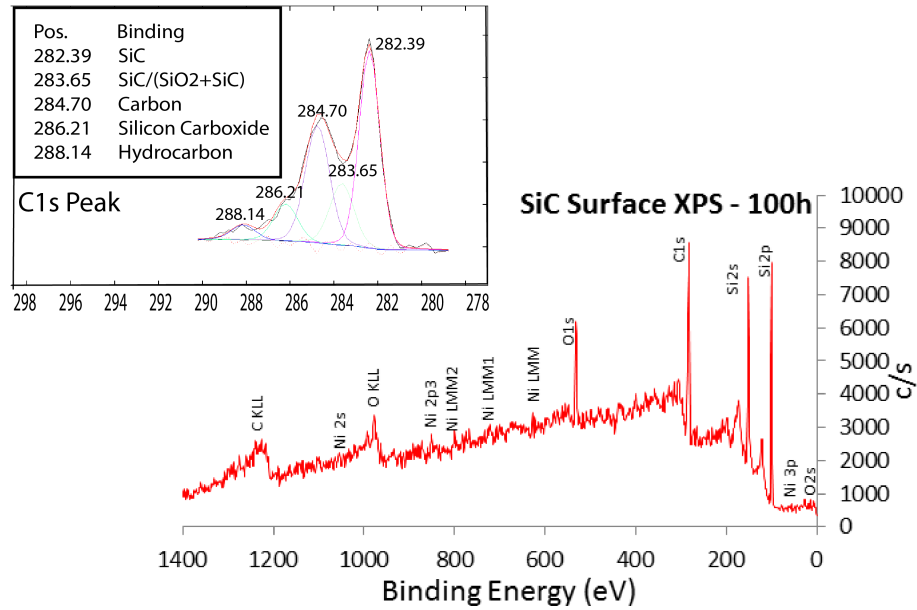
Figure 2.20. Surface XPS data of a 100 hour exposed SiC sample. Analysis of the C1s carbon peak (upper left) reveals that there is oxidation as well as the formation of hydrocarbon chains. Note that the Fe peak is no longer detected.
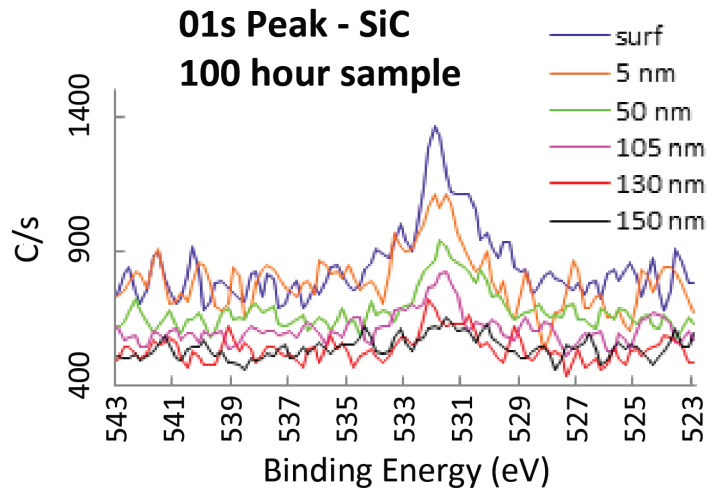
Figure 2.21. Depth of oxidation of SiC over 100 hours of testing based on XPS of the O1s peak. The peak is indistinguishable from the signal noise by 150 nm.

Sapphire Etching and Ion Diffusion   The pre-cleaned sapphire samples had surface contaminants including the Ni and Fe seen in the initial SiC surface scans. The scan also

detected Si and C on the surface, see Figure 2.22. These contaminants were likely deposited on the surface of the sample once etched from the SiC sample surface as they were tested in the same chamber. These contaminants were all surface level and were removed with a DI water soak.

The degradation of the sapphire structure was shown in a different way from that of SiC. As sapphire is already an oxide, the XPS scans were looking for binding energy shifts in the oxide peak. These shifts around the 74 eV binding energy for the Al2p peak for sapphire indicate oxide degradation to a different aluminum oxide form. The binding energy shift can be seen in Figure 2.23. This damage penetrated to a depth of 50 nm for both 50 and 100 hour exposure tests. The nickel diffused to a depth of 10 nm for both of these exposure times. This indicates that sapphire was the most stable encapsulation material for down hole geothermal sensors.
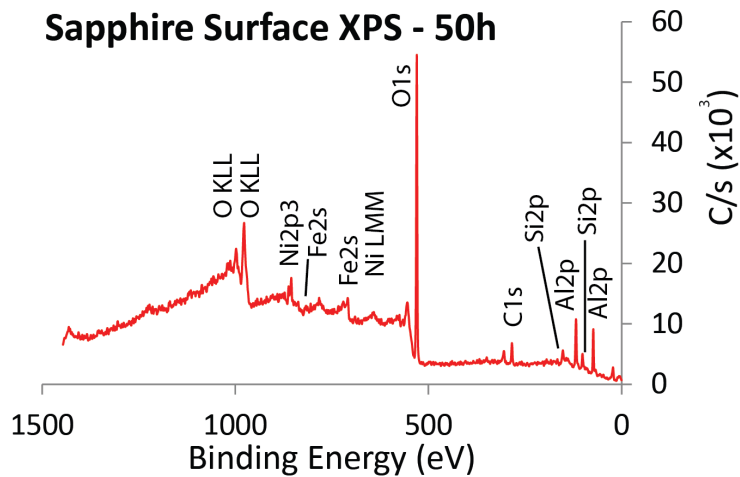
Figure 2.22. Sapphire surface scan after 100 hours to exposure in critical point water before cleaning. Surface contaminants including Ni, Fe, Si, and C are shown.
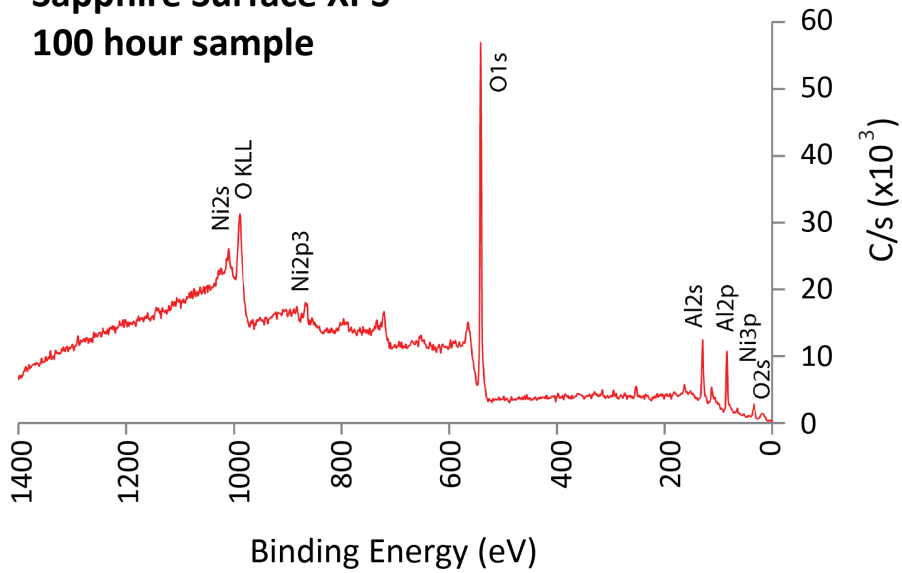
Figure 2.23. Sapphire surface scan after 100 hours of exposure in critical point water. The diffused Ni ions can be seen as well as the Al and O peaks.
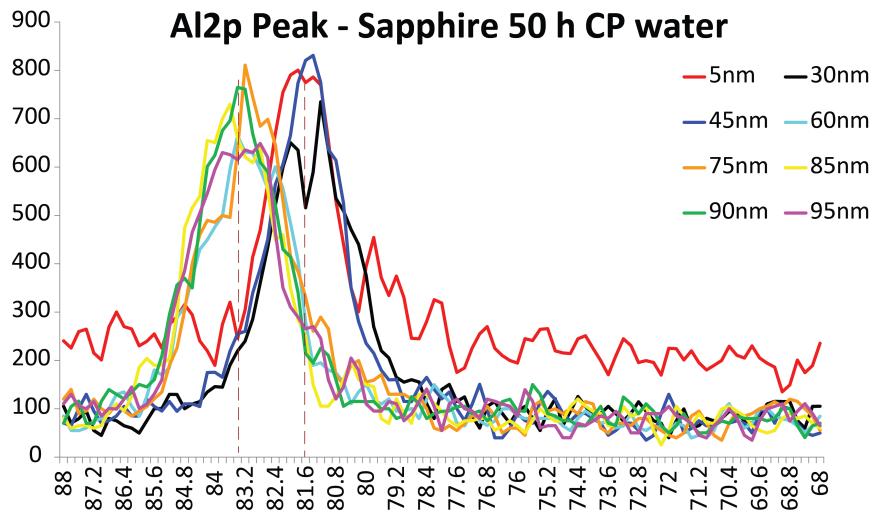
Figure 2.24. Shift in Al2p peak from a 50 hour sapphire sample. The first 50 nm of the sample are degraded and shown by a shift in the peak. All of the peaks have been shifted by about 8 eV due to sample charging.

2.2.4 Summary of Material Testing in Water

The water testing exposure data detailed in this section provide the basis for the design of fabrication processes with encapsulation to shield sensors during down hole operation in geothermal wells. Of the materials exposed, sapphire is the most promising material for both the substrate and encapsulation of MEMS devices for down hole operation because 1) the decreasing rate of surface roughening at longer exposure times 2) no additional material degradation between the 50 and 100 hour exposure tests and 3) minimal and constant depth of Ni diffusion. SiC does not appear to have an asymptotic degradation behavior. Longer duration tests or brine testing may show that degradation ceases at a deeper depth than the sapphire samples. While the SiC degraded more than the sapphire, it was also tested in the brine environment to determine the salt effects on the material.

Silicon is not a suitable material for direct exposure in geothermal environments. There is significant weight loss in vapor, liquid, critical point, and super critical water environments. Amorphous SiC and AlN are also not suitable materials as they are etched within 100 hours of exposure.

2.3 Subcritical Geothermal Brine Testing

2.3.1 Geothermal Brine

A geothermal brine environment must be defined before brine testing can be conducted. Supercritical brine can be either a binary or ternary water-salt system rather than the uniary system seen with supercritical water. The ternary water-salt systems are seen with more chemically complex salt systems such as SiO_2-H_2O-NaOH or H_2O-HgI_2-PbI_2. Of the binary systems, there are two different classifications. For high solubility salts such as the more common NaCl, NaOH, KOH, and KCl compounds there is no intersection of the critical and solubility curves, meaning the salt and water are either in a single homogeneous mixture, or most of the salts dissolved in water precipitate out of solution in the supercritical phase. For NaCl only around 100 ppm remains in solution depending on the system pressure [63]. This is significantly lower than the 360,000 ppm solubility limit of NaCl in room temperature water. So, in the supercritical phase salt water will attack samples similarly to water with no salts present. This means that adding salts would not greatly change the exposure testing results from those taken in the supercritical phase. However, the presence of salts increases the fluids critical point. A paper written by Valyashko in 1997 shows the increases for solutions critical points with different salt compounds and concentrations [64].

Many studies have shown that liquid water near the critical point is more corrosive as the fluids have not gone through the drastic density change seen in the supercritical phase [65], [63], [66], and [67]. While these studies were conducted on metals used in supercritical reactors rather than ceramics used for MEMS sensors, most wells within the U.S. are below

supercritical temperatures [11]. As this could be a potentially more corrosive environment, especially with the salts precipitated out of the supercritical phase, a sub-critical liquid environment was chosen as the characteristic brine environment. The brine exposure tests were conducted in sub-critical conditions at 350 °C at 25 MPa.

The brine chemistry defined for this experiment was based on the salt most common in U.S. geothermal wells. The average amounts of salts most from the well data for wells above 150 °C were compared. The top three salts are NaCl, KCl, and $CaCl_2$ with 8624.7 mg/L, 2476.9 mg/L, and 4045.9 mg/L respectively [11]. NaCl was used to reduce variables in the experiment as it has the highest average concentration of 0.265 mol%. At this small concentration, the critical point of the brine solution is only slightly higher than that of water at approximately 285 °C. Higher salt concentrations would further increase the critical point of the fluid and could lead to increased reaction rates of the exposed materials. Brine testing environmental chemistries should be varied to generate a more complete picture of how the materials behave in a wider array of geothermal environments in future experiments once initial tests have been conducted to eliminate materials that are not environmentally suitable.

2.3.2 Exposed Materials

Materials that were exposed to geothermal brine include single-crystal diamond, micro-crystal diamond, vitreous carbon, SiC, and sapphire. The sapphire, SiC, vitreous carbon, and single-crystal diamond were tested as bare substrates while the micro-crystal diamond was grown on bare Si substrates. The sapphire and SiC used for brine testing were from the same vendors as were used for the water exposure testing. The substrate materials were diced into 4x4 mm dies while protectively coated with photoresist. The photoresist was stripped with acetone post dicing. The dies were then cleaned with IPA and dried with N_2. The single-crystal diamond that was tested was from the National Institute for Materials Science (NIMS) Optical & Electrical Materials Unit in Ibaraki, Japan. The 2.5x2.5x0.5 mm sample was doped with a N = 2e19 cm^{-3} concentration.

The micro-crystal diamond was grown on Si so that its effectiveness as an encapsulation layer could be determined. As Si is known to be heavily etched in the liquid water phase from the initial water testing, Si samples can be encapsulated with micro-crystal diamond, and the silicon's survival or degradation can be used as another test of the diamond films viability. A bare 4" Si wafer was diced into 4x4 mm dies. Conformal coverage can be seen in Figure 2.25. These dies were cleaned in acetone, IPA, and dried with N_2 gas. The dies were seeded using an ultra sonic diamond seeding bath for 5 minutes. The dies were then washed with methanol and dried with N_2 gas. Once seeded the dies were placed on top of a dummy wafer on the cooling stack of a Sp3 model 655 series HFCVD diamond deposition reactor. Tungsten filaments were prepared and installed above the cooling stack. These filaments were heated to 1950 °C to keep the dies at 720 °C. Methane is used as the carbon source for diamond growth. Trimethylboron, $B((CH_3)_3)$, is flowed for the in-situ doping of the films. A 35 hour deposition was done to deposit 2 μm layer of diamond. The samples

were then flipped, new filaments were made and installed, and another 35 hour deposition was conducted to grow diamond evenly on all sides of the dies with a crystal layer with a 4 μm nominal thickness.
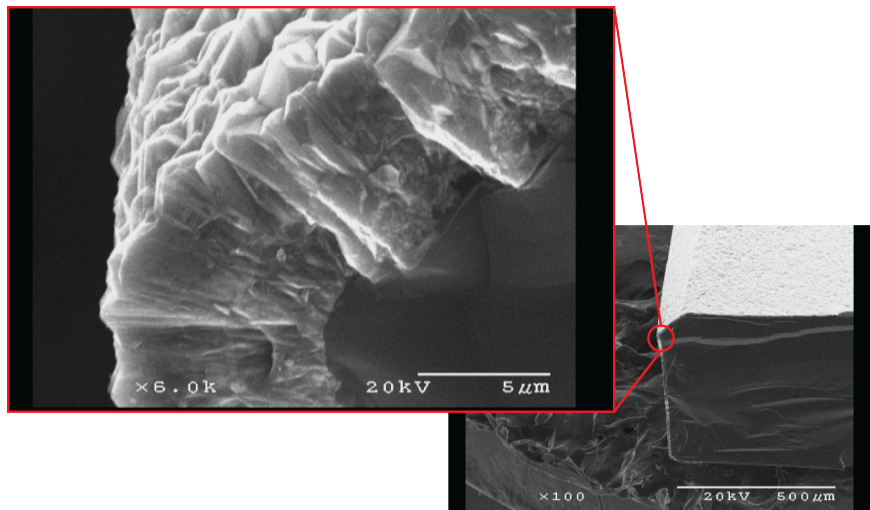
Figure 2.25. Conformal micro-crystalline diamond grown on a Si die.

For initial brine testing, vitreous carbon, Sigradur G, was purchased in thin bar stock from HTW. Vitreous carbon can be made by the pyrolyzation of PR to encapsulated sensors in future exposure tests if initial tests show this as promising testing option.

2.3.3   Experimental Set-up

Testing in geothermal brine rather than water poses new challenges in the design of the experimental setup. One of the main difficulties is maintaining a constant geothermal brine chemistry during the experiment. To maintain this chemistry, the container in which the experiment takes place must be an inert material. Gold reaction capsules shown in Figure 2.26 were used to seal the brine and test sample into a controlled environment. This is a common technique used in many geophysical and geochemical studies. These capsules are either closed with plugs [68], flattened and bent [69], crimped [70] or most commonly and effectively, welded [19],[71],[72]. The gold purchased for these experiments was ordered from Depths of the Earth with a 4 mm OD for ease of removal from the Tuttle pressure vessel used for the water testing. A special DC precious metal welder was used to reliably weld the gold capsules in an inert Ar environment.

Samples were exposed for 100, 200, and 300 hours. Controls were welded into gold capsules and were not exposed to increased temperatures and pressures. A total of 21 capsules were welded including 4 vitreous carbon dies, 5 sapphire dies, 5 SiC dies, 5 micro-crystalline diamond coated Si dies, 1 single crystal diamond die, and 1 capsule with salt water brine and no die enclosed.

Figure 2.26. A welded gold capsule shown with a U.S. nickel as a scale reference. The capsule is filled with salt water brine and a 4x4 mm 4H-SiC die.

Once testing was completed, dies were removed from their capsules and soaked in DI water for 24 hours to dissolve any salts that were sitting on the samples surfaces. Samples were then rinsed with DI water and dried with N_2 gas. Samples were then analyzed similarly to the water samples using a SEM for imaging, sputter XPS for chemical analysis, and white light interferometry for surface roughness data when appropriate.

2.3.4   Geothermal Brine Testing Results

Of the 21 sealed gold capsules, 18 survived the exposure testing, which is an improvement on the 20% to 50% burst rate seen with sealed glass capillary reaction capsules used for supercritical water testing [73]. The 200 hour and 300 hour sapphire samples and the 200 hour SiC sample were compromised due to bursting as shown in Figure 2.27 or collapsing of the gold capsules. All of the samples were weighed pre- and post-exposure, and there was no weight change for any of the samples within a 5 mg tolerance, approximately 100 μm on a 4x4 mm die.

Figure 2.27. This gold capsule burst at the crimp location. The gold is coated with an ethylene glycol residue used in the water pressure lines in the test vessels.

Brine samples were taken from within the testing capsules post exposure to ensure that no gold from the reaction capsule walls entered the fluid. There are no traces of gold seen in the water samples. This indicates that the brine did not chemically attack the gold reaction

capsules. XPS surface scans shown in Figure 2.28 reveal Na and Cl ions from the salt and oxygen and carbon from the drying process prior to analysis.

Vitreous Carbon 300h Water Sample
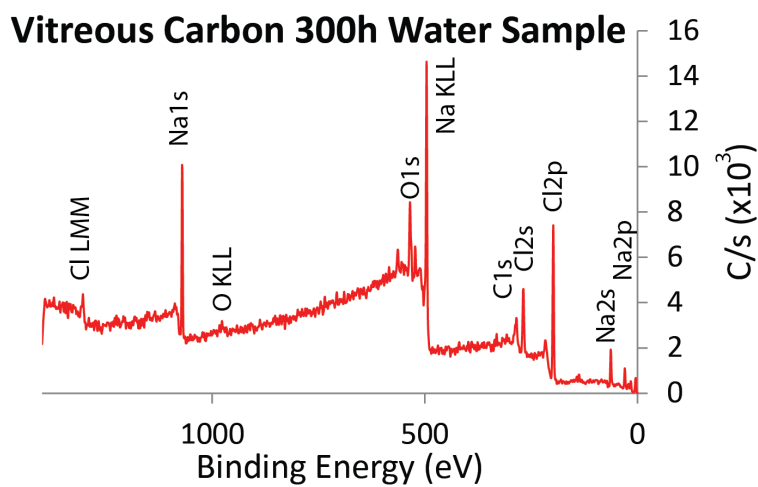
Figure 2.28. Surface XPS scan of dried brine fluid on Si carrier die.

Vitreous Carbon Brine Testing Results

SEM images were taken of the vitreous carbon before testing and post 0, 100, 200, and 300 hours of heated and pressurized brine exposure. These images are shown in Figure 2.29. A full set of SEM images for all times are shown in Figure A.1 in Appendix A. The pre-exposure scans show a smooth top surface and a rough, layered side profile. There are no visual surface changes to the control sample exposed to the simulated brine with no heat or pressurization. However, after 100 hours of exposure at the pressurized elevated temperature, the sidewall is dramatically eroded and appears smooth. The top surface reveals pinholes with approximately 5 μm diameters. Pinholes also appear in the 200 and 300 hour exposed samples. These pinholes will allow the infiltration of brine into the encapsulated sensors, so this type of vitreous carbon is not an appropriate material for encapsulation in the geothermal environment. As the sample did not pass optical inspection, no post exposure XPS or other measurements were taken.

Sapphire Brine Testing Results

The 200 hour and 300 hour sapphire reaction capsules did not survive the pressurization process during exposure testing. The data from the pre-exposed samples, control sample, and 100 hour exposure test are presented. As with the water testing, the surfaces of the sapphire samples appear to be strongly attacked by the environmental exposure as shown in Figure 2.30. A full set of SEM images for all times are shown in Figure A.2 in Appendix
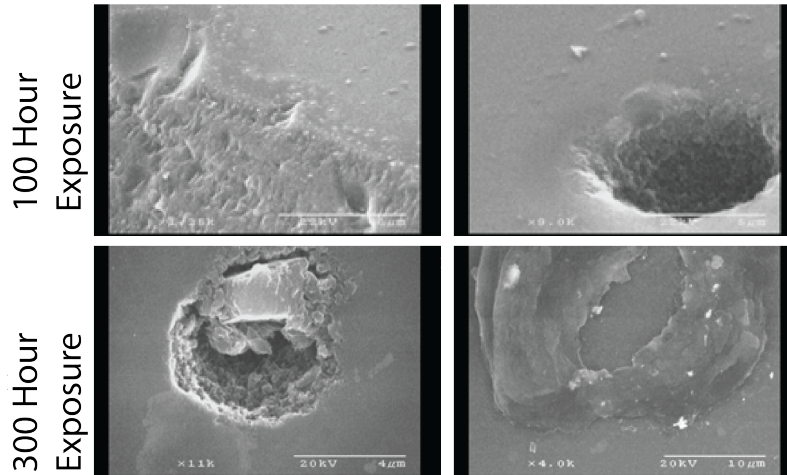
Figure 2.29. SEM images of vitreous carbon exposed for 100 and 300 hours in the simulated geothermal brine environment.

A including images from the 300 hour capsule that broke. That sample is shown to display the effects of a burst capsule on the sapphire sample. The control sample and 100 hour exposed sample have dramatically changed surfaces from the pre-exposed sample. Before soaking the sapphire sample in water for 24 hours, a SEM image revealed that significant amounts of salt have adhered to the sample surface. These salts were removed after the DI water soak. While the surfaces appeared to be greatly damaged, white light interferometry, shown in Figure 2.31, and stylist profilometry revealed that this surface damage is on the order of tens of nanometers as was measured with the water tested samples. An average surface roughness of 4.33 nm was measured for the 100 hour sapphire samples. While the 200 hour and 300 hour samples did not survive testing, surface roughness measurements were taken to show the difference in surface effects when capsules burst versus collapsed. Surface roughness of 110 nm was recorded for the 200 hour sapphire sample in the burst capsule and a roughness of 4.13 nm for the 300 hour sample within the collapsed capsule. The exposure to that ethylene glycol the leached into the 200 hour capsule has roughened the sapphire surface more dramatically than both the water and brine testing.

Sputter XPS was used to determine the depth of sample degradation below the surface roughening. The Al2p peak was tracked through the sample to see when it becomes a single peak at the expected binding energy for crystalline sapphire. The control sample shows degradation down to 24 nm. For the 100 hour exposed sample, the peak stabilizes at a sputtered depth of 30 nm. The 200 hour and 300 hour samples were not measured using the XPS technique as the exposure testing was compromised. Further investigation is required with the sapphire materials to determine its compatibility with the down hole geothermal environment.
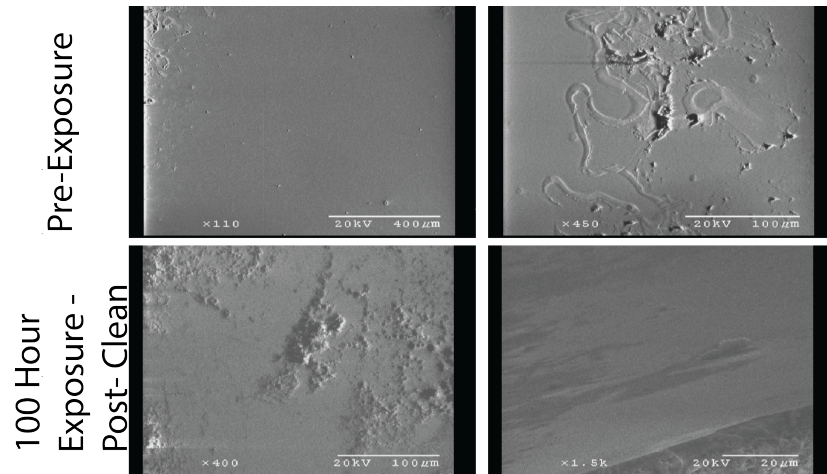
Figure 2.30. SEM images of sapphire pre-exposed and post 100 hours of exposure in the simulated geothermal brine environment.

SiC Brine Testing Results

SEM images did not reveal any surface defects or roughening of the 4H-SiC substrate material. However, there was some erosion that could be seen in the roughening of the SiC sample side wall. Surface and side wall SEM images are shown in Figure 2.33. A full set of SEM images for all times are shown in Figure A.3 in Appendix A. After dicing, in the pre-exposure images, there are some small hole type imperfections that can be seen on the SiC side wall. After 100 hours of exposure, there are many more holes seen on the side walls. After 300 hours of exposure, these holes have fully textured the side of the SiC die. These changes show the SiC material degradation over time.

Sputter XPS was used to determine the depth of surface oxidation of these samples. In the pre-exposed SiC sample, there is a native oxide of less than 8 nm. The oxide depth was measured using Voigt peak fitting of both the Si2p peak as shown in Figure 2.34 and the C1s peak. This is slightly greater than the values reported in the literature. The 100 hour exposed sample was oxidized to a depth of 108 nm. The stabilization of the C1s peak at 282.6 eV, a carbon binding energy for SiC from the NIST database, is shown in Figure 2.35. This data was also verified using the Voigt peak fitting technique for the C1s and Si2p peaks. The large surface peak at 284.6 eV is due to a thin partially graphitized surface layer. The 300 hour sample showed minimal oxidation. This was surprising as all other exposure tests of the SiC material showed oxidation. This sample may be an anomaly or may indicate that there is an etching and removal process that occurs with the SiC degradation. If that were the case, the 300 hour sample shows a time in which the oxide is less present on the sample surface. Further testing with the SiC substrate material is required to determine its potential usability for geothermal MEMS.
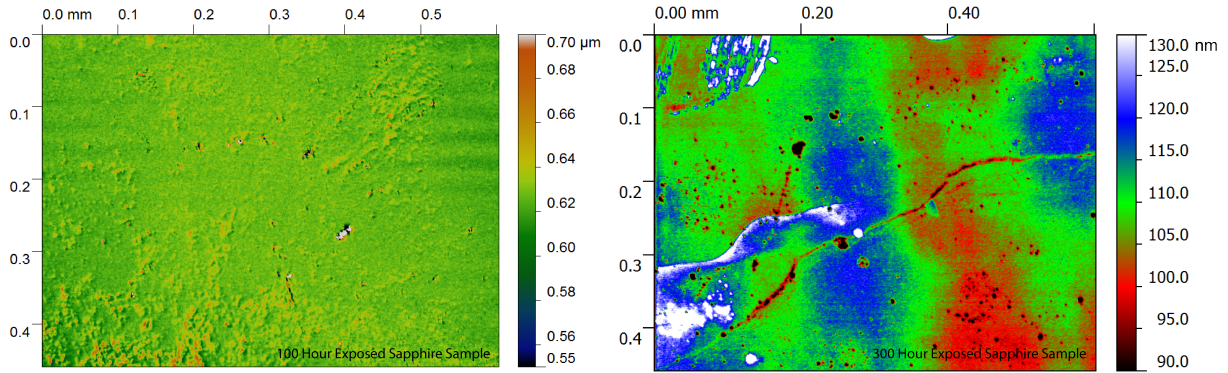
Figure 2.31. White light interferometry scans of sapphire exposed for 100 hours and 300 hours. The 300 hour sample was in a collapsed gold capsule and shallow surface roughening is measured.
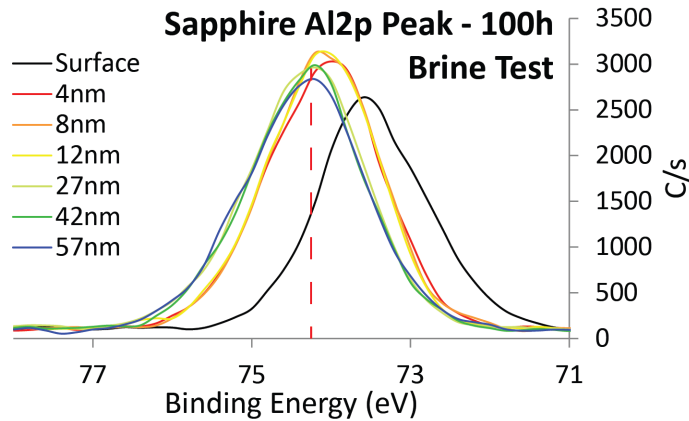
Figure 2.32. Sputter XPS scans of 100 hour exposed sapphire Al2p peak. The peak position stabilizes at a depth of 30 nm.

Single Crystal Diamond Brine Testing Results

Only one single crystal diamond (SCD) sample was exposed to the simulated brine environment due to the rarity of the samples. This sample was tested for 300 hours. Pre- and post-exposure SEM images and XPS surface scans were taken for sample analysis. There was some surface oxidation shown both pre- and post- exposure surface XPS scans. Surface oxygen content dropped from 8.1% to 7.7% post 300 hours of exposure as indicated on Figure 2.36. The oxygen peak was scanned using sputter XPS to determine the oxidation depth. The oxygen peak is no longer present in the XPS scans after sputtering to a depth of 4 nm as shown in Figure 2.37. The SEM images taken for the SCD sample did not reveal any surface changes. SCD is a promising material for survival within the geothermal environment as the oxidation on the SCD sample appears to be the same thickness as the
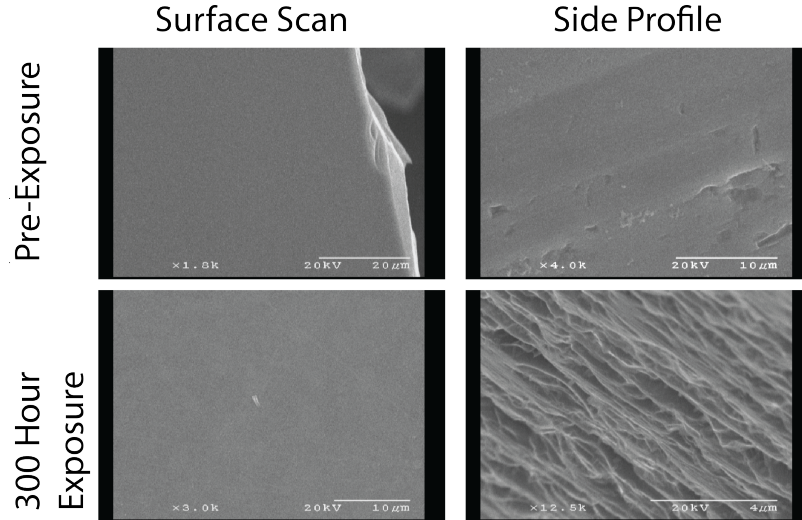
Figure 2.33. SEMs of SiC before brine exposure and post 100 hours of exposure in the simulated geothermal brine environment.

native surface oxide after 300 hours of exposure. However, the fabrication of SCD is not well developed. Developing an encapsulation process using this substrate material would be timely and costly.

Micro-Crystalline Diamond Brine Testing Results

The most expected failure mode for micro-crystaline grown diamond encapsulation was pinholes, which would allow the simulated brine to attack the underlying silicon. There was no mass loss recorded for any of these samples indicating no major silicon or diamond etching. SEM images were taken of the diamond surfaces and cross-sections, shown in Figure 2.38. A full set of SEM images for all times are shown in Figure A.4 in Appendix A. The cross sections show a 4.31 μm nominal thickness for all exposure times. Surface scans for each exposure time, shown in Figure 2.39, show mostly carbon content in each material make-up. There is no silicon signal indicating no pinholes in the micro-crystalline diamond. There is an overall lower counts per second reading for the longer testing micro-crystalline films. This could be due to charging of the surface from a reduced surface electrical conductivity. The surface of the diamond is graphitized, which leads to a drop in the sample conductivity, increasing signal noise. However, this effect is only on the top surface layers and does not appear to penetrate the sample based on the SEM images that show no crystal deformation over time. In addition, the Auger peaks are inspected and show that there is a shift in the surface Auger scans for the 200 and 300 hour exposed samples, see Figure 2.40. The peak shifts back to the control levels after 4 nm of sample sputtering. Shifts in carbon Auger peaks, measured using electron kinetic energy, have been used to differentiate between diamond, graphite, and polyethylene [74]. In addition to peak shifts, peak shapes have been shown to distinguish between the different carbon bindings of diamond and graphite.
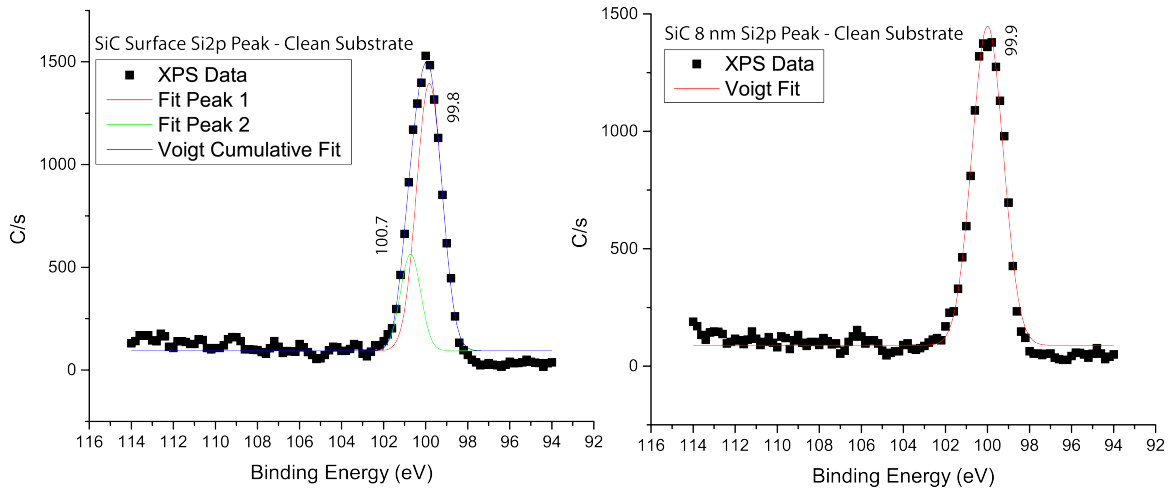
Figure 2.34. Sputter XPS scans of Si2p peak for SiC substrate with no exposure in the simulated geothermal environment. Peaks for Si in bindings of SiO_2 and SiC and seen on the surface. Only the SiC bound Si2p peak remains in the 8 nm scan showing that all of the oxide has be sputtered off the surface.

There is some surface oxide on the pre-exposed and 100 hour exposed samples. This oxide composed 1.9% of the pre-exposed sample and 2.2% of the 100 hour sample. This oxide is removed after 4 nm of sputtering as shown in Figure 2.41.

2.3.5   Summary of Brine Testing

Five different materials were exposed to a simulated geothermal environment based on the 0.265 mol% average NaCl concentration in U.S. geothermal wells. Subcritical conditions were used as the testing environment as they provide a more characteristic geothermal environment for U.S. wells and because the NaCl salt stays in solution in these conditions. Of the materials tested, the vitreous carbon was the least robust material. Pinholes formed within the first 100 hours of exposure testing, making vitreous carbon a poor choice for MEMS sensor encapsulation. While the formation of pinholes was not expected, it is not completely surprising. The pyrolization process used in making vitreous carbon leads to some cross linking between layers of bonded carbon making it stronger in the out-of-plane direction than graphite. However, this partial cross linking can lead to surface sites that are less robust than the fully cross linked diamond structure.

SiC experienced oxidation on the order of hundreds of nanometers over the 300 hours of testing. Sapphire experienced surface roughening on the order of tens of nanometers. As only one of the exposed capsules survived exposure testing, a degradation trend cannot be extrapolated for the sapphire samples. Both the single crystal diamond and the microcrystalline diamond were the most chemically robust. There was minimal surface oxidation and no detectable surface roughening post 300 hours of exposure. Single crystal diamond is
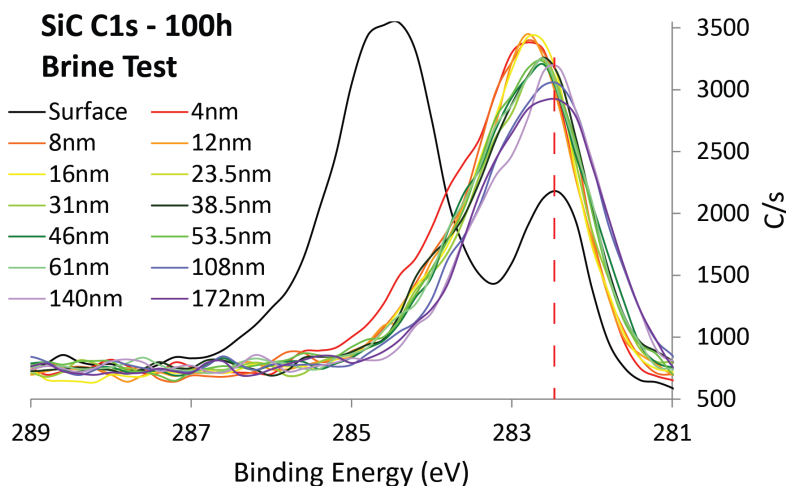
Figure 2.35. Sputter XPS scans of C1s peak for SiC sample exposed for 100 hours in the simulated geothermal environment. The peaks stabilize at a depth of 108 nm.

expensive, and there are few developed microfabrication techniques for processing making it difficult to integrate with MEMS sensors. Micro-crystalline diamond is grown in a MEMS compatible reactor that could be used to either make devices directly or to encapsulate MEMS made from other harsh environment materials.

2.4   Conclusions of Materials Testing

Initial testing in four pressure and temperature conditions of water and sub-critical brine reveled the failure mechanisms of may MEMS compatible materials. Silicon was used as a control and was shown to lose significant mass in vapor, liquid, critical point, and supercritical water. Mass losses of almost 80% after 20 hours in supercritical water were measured. Porous etching of silicon was greatest in the supercritical environment as the low density of the supercritical fluid was more readily able to remove oxide bi-products from the exposed surfaces preventing the passivation effects of the silicon dioxide. The etching effects were slower in the liquid environment when etch products were not transported away from the sample surface as readily. Aluminum nitride and amorphous SiC thin films were also unable to survive within water at its critical point for up to 100 hours. Chrome/platinum layers appeared to survive the water testing; however, the layers delaminated from the substrate surfaces. New adhesion layers and processes must be developed if metal layers are going to be exposed in the geothermal environment.

In the salt brine testing, vitreous carbon did not survive due to the formation of surface pin holes. SiC and sapphire show some promise for encapsulation. The SiC samples experience surface oxidation in both water and brine environments. Oxidation increases with time

41

SCD Pre-Exposure Surface Scan

Carbon - 91.9%
Oxygen - 8.1%

CPS

C KLL, O KLL, O1s, C1s

Binding Energy (eV)
1000, 500, 0

SCD 300h Brine Test

Carbon - 92.3%
Oxygen - 7.7%

CPS

C KLL, O KLL, O1s, C1s

Binding Energy (eV)
1000, 500, 0
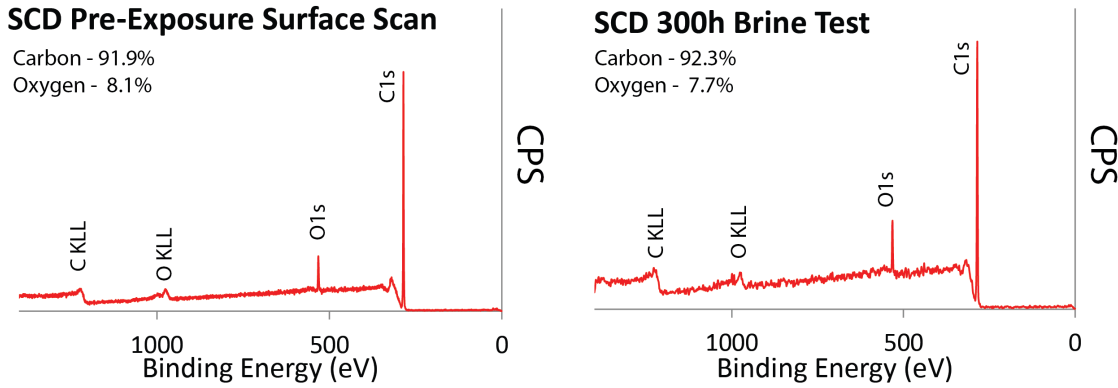
Figure 2.36. Surface XPS scans of the single crystal diamond sample pre- and post-exposure in the simulated geothermal brine environment.

SCD O1s Peak - 300h Brine Test

— 4 nm
— 8 nm
— 12 nm

C/s
500, 450, 400, 350, 300, 250, 200, 150, 100

Binding Energy (eV)
545, 540, 535, 530, 525, 520
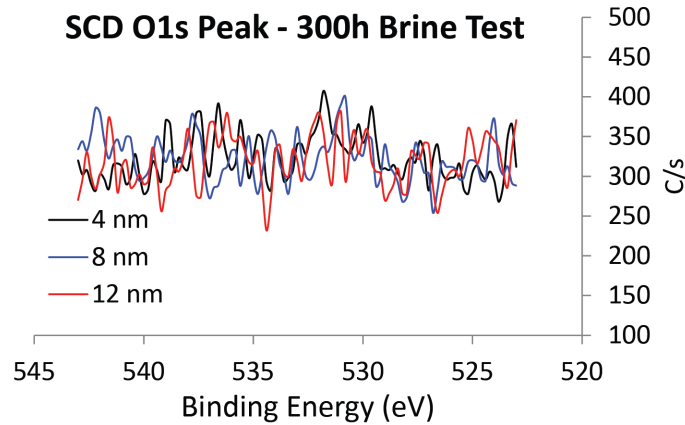
Figure 2.37. Sputter XPS scans of the O1s peak for the single crystal diamond sample post 300 hours of exposure.

in the water testing. Longer tests in the brine environment are required to determine if there is an oxidation and removal process that occurs on the SiC sample surface or if there was an error with the 300 hour test.

The sapphire samples show surface roughing and material degradation in both water and brine environments. In the water testing, the rate of surface roughing decreases at longer exposure times. Also, the degradation is the same depth for 50 and 100 hour tests at 50 nm depth. Brine tests show less degradation, 30 nm after 100 hours of testing. A surface roughening average of 4.33 nm for the 100 hour brine test is significantly less than the 100 hour surface roughness average of 36.7 nm seen in the sapphire sample tested in critical point water.

Single crystal diamond and micro-crystalline diamond have the best survivability of the tested materials. There was no measurable surface roughing and only minimal surface oxi-
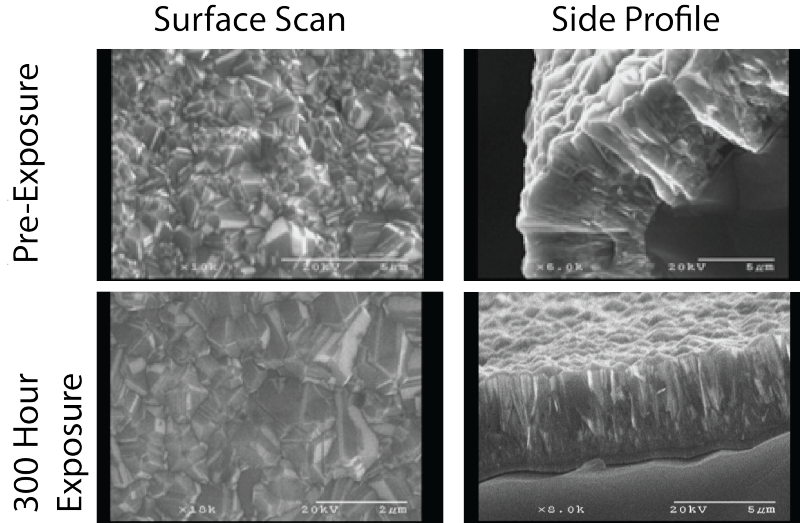
Figure 2.38. SEMs of pre-exposed micro-crystalline diamond and post 300 hours of exposure in a simulated geothermal environment.

dation with less than 4 nm measured after 300 hours of testing. Slight surface graphitization led to increased XPS signal noise; however, the graphitization appears to be only surface level. No pin holes were detected in SEM images of the grown micro-crystalline film, and there was no Si peak from the underlying Si substrate in the XPS scans. These results indicated that diamond is the best choice of the exposed materials for MEMS encapsulation. As the micro-crystalline diamond can be grown in a thin film form that is integratable with current MEMS processes, this is a preferable choice to the single crystal diamond.

Synthetic Diamond Surface XPS Scans

Substrate Scan

100h Brine Test

200h Brine Test

300h Brine Test
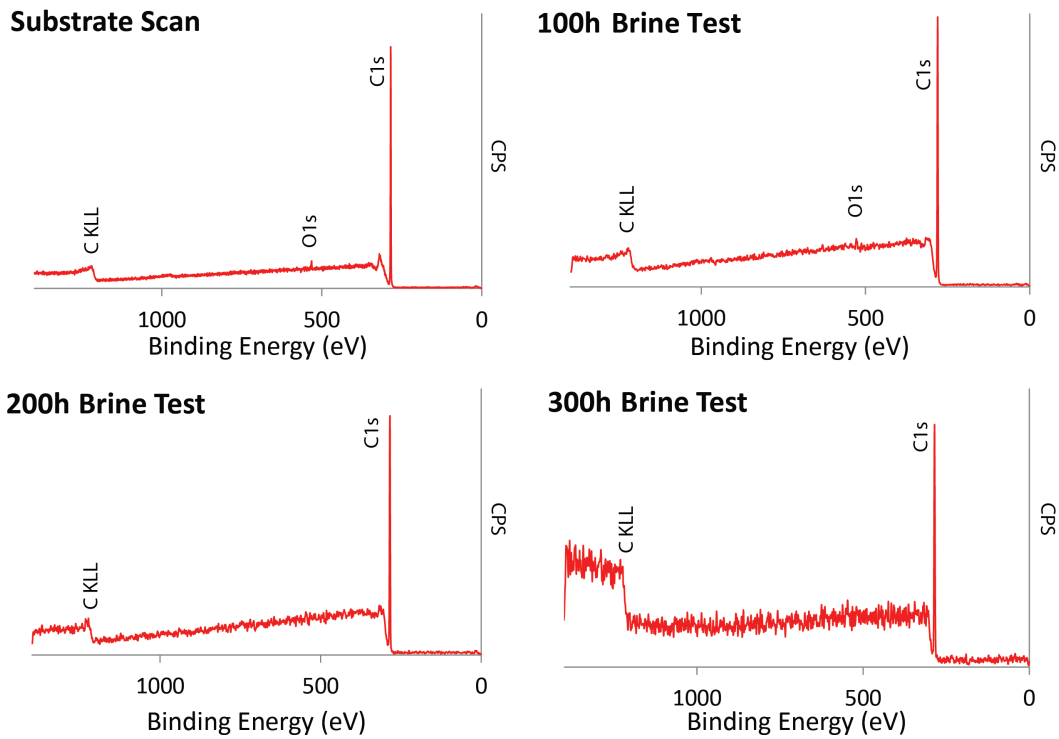
Figure 2.39. Surface XPS scans of micro-crystal diamond sample pre- and post-exposure in the simulated geothermal brine environment.

Carbon Auger Peak Micro-Crystalline Diamond 200h Brine

- Surface
- 4 nm
- 8 nm
- 16 nm
- Control

Carbon Auger Peak Micro-Crystalline Diamond 300h Brine

- Surface
- 4 nm
- 12 nm
- 20 nm
- 75 nm
- Control
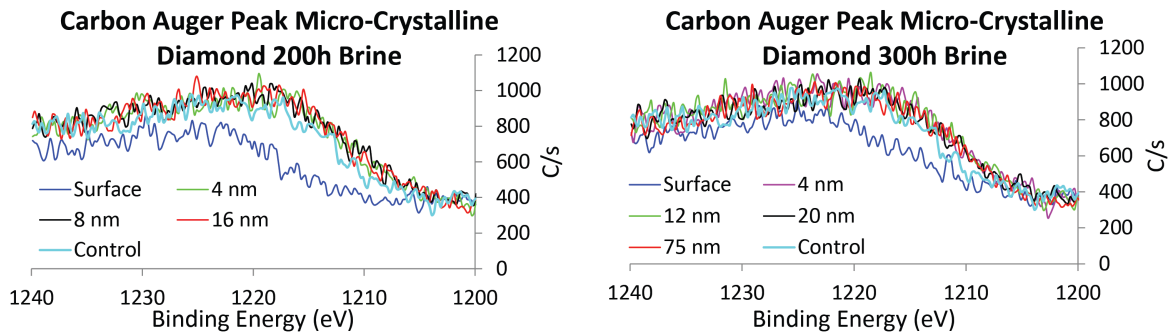
Figure 2.40. XPS scans of carbon Auger peak for 200 and 300 hour exposed micro-crystalline diamond samples.

44
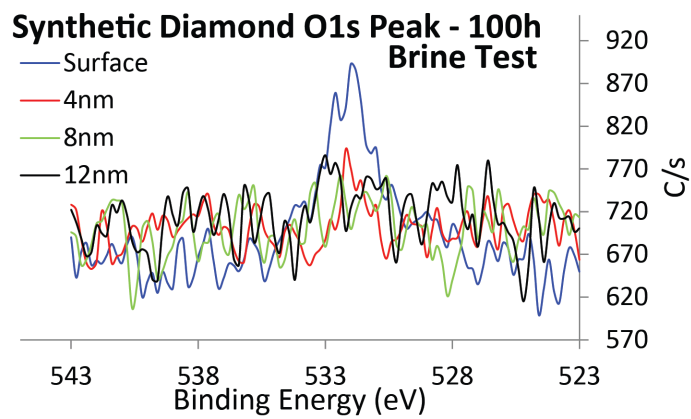
Figure 2.41. Sputter XPS scan of O1s peak of micro-crystal diamond after 100 hours exposure in the simulated geothermal brine environment.

Chapter 3

Ruggedizing State-of-the-Art Temperature Sensors for Harsh Environments

Temperature sensing in geothermal environments is important as it will provide data to improve geothermal well models for exploratory applications and to monitor well conditions over the life of the well. Improved geothermal models will help reduce exploration costs, which is a large percentage of geothermal electric power generation system startup [8]. Down well temperature data can be used to improve well life time predictions and viability [75]. Operational well monitoring will increase well efficiency and safety. While pressure, temperature, and pH are commonly sought for in initial monitoring of the down hole environment, the sensor portion of this research is only focused on temperature sensor development.

3.1 Current Temperature Sensing Technology

Before designing a new temperature sensor, it is important to assess the necessity of this work. There are a wide variety of existing temperature sensors with different mechanisms for measuring temperature within desired temperature ranges and resolutions. Common temperature sensors include thermistors, thermocouples, RTDs, optical sensors, and frequency response sensors. Some of the key properties of these sensors are summarized in Table 3.1.

A thermistor, or thermo-resistor, is one of the most basic types of temperature sensors. It utilizes the phenomenon that the resistance of most materials changes with temperature.

Type	Max Temp (°C)	Resolution	Harsh Environment	Drift	Power
Thermister	130	high	maybe	medium	yes
RTD	500	high	no		yes
Thermocouple	1250	low	maybe	high	yes
Fiber Optic	300	low	yes	high	no
Si MEMS	250	high	no		no
SiC MEMS	600	high	yes	low	no

Table 3.1. Summary of key properties of existing temperature sensors.

A well characterized and linear temperature coefficient of resistance (TCR) is desirable for a reliable thermistor. Thermistors are often made from ceramics or polymers and are used for smaller temperature ranges, usually between -90 °C to 130 °C [76], with high accuracy of around 0.1 °C. This temperature maximum is too low for the geothermal applications.

RTDs, resistance temperature detectors, have a similar operation to that of thermistors; however, they are made with metals rather than ceramics or polymers. RTDs usually consist of a wire wrapped around a ceramic core. They offer long term stability and high accuracy within a range of -200 °C to 500 °C. However, RTDs are known to be fragile and easily damaged in harsh environments [77].

Thermocouples are a common temperature measurement tool. A thermocouple operates by measuring a potential difference between two dissimilar metals in the desired temperature field. The operational range of around -250 °C to 1250 °C is the trade off for lower accuracy [14]. There are many different metal junctions that can be used to create thermocouples. These pairs are denoted with a calibration letter, each with a different sensing range and sensing accuracy. Special high temperature thermocouples are commercially available up to 2300 °C; however, these sensors suffer from drift in high temperature environments [78].

Other temperature sensors have been designed to give signal outputs ranging from frequency, to optical, to capacitive [79], [80], and [81]. Each of these mechanisms has potential benefits for specific environments; however, most of these sensors require an electrical energy input.

A capacitive sensor was desired for this research as it can be easily coupled with a wireless RF transmission system. A passive, capacitive device would allow temperature to be measured with little or no on board power, reducing system complexity by reducing components. This could include eliminating the on chip battery requirement, extending sensor life. If small amounts of power are required, on chip energy harvesters can be integrated to meet the low power demand.

There have been some macro-scale, wireless, passive, capacitive temperature sensors that were made and tested as a part of an RF coupled system up to 235 °C. These sensors were mounted to rotary devices and the signal was detected with a loop antenna [82].

MEMS sensors are an ideal platform for designing capacitive sensors as capacitive forces

are more dominant in the microscale than the macroscale due to the ability to decrease gap spacing using microfabrication techniques. MEMS also have the advantage that the sensing elements and circuits can be co-fabricated on the same chip. This reduces production complexity and overall sensor system size. This small foot print allows MEMS to be placed in locations that do not obstruct normal system operation. This will allow for more sensors to be used in a system; thus, more useful data can be collected. There are MEMS temperature sensor designs that have been fabricated out of non-harsh environment compatible materials. Many of them require external power supplies to function; however, there are some designs that can be used for passive sensing, which could be integrated to a passive radio frequency (RF) circuit.

3.1.1 Capacitive Sensing

Before discussing existing MEMS passive capacitive sensors, it is important to understand some details about the mechanisms of capacitive sensing and how capacitors can be coupled with an oscillating RF circuit for wireless integration. RF signal transmission of subsurface applications and beacon type systems are in the kHz to lower MHz frequency band. The resonance frequency of a LCR circuit is determined by both the capacitor and the inductor. At resonance, the capacitor reactance X_C and inductor reactance X_L are equal. A basic series RLC circuit is shown in Figure 3.1.
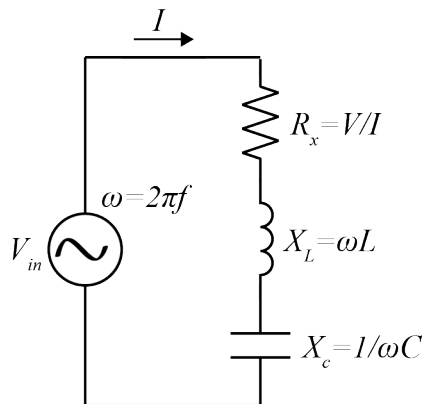
Figure 3.1. Basic series RLC circuit showing the individual component impedances.

Circuit resonance occurs when electrical impedance is minimized. Electrical impedance, Z, is define by:

$$Z = \sqrt{Z^2 + (X_C - X_L)^2} \tag{3.1}$$

So, at resonance:

$$X_L = \omega L = X_C = \frac{1}{\omega C} \tag{3.2}$$

$$\omega = \sqrt{\frac{1}{LC}} \tag{3.3}$$

The potential capacitance range for the temperature sensor is in part limited by the possible inductors that can be fabricated using MEMS fabrication techniques. Most MEMS scale on chip inductors have values on the order of nano-Henrys, [83], [84], and [85], resulting in a capacitive value in the nano-Farad range to maintain a resonance frequency in the kHz to lower MHz band. However, recently inductors in the μ-Henry range have been fabricated using microfabrication techniques [86]. Using inductors in the μ-Henry sets a nominal capacitive sensitivity in the pico-farad range while maintaining a mid MHz frequency. With further inductor improvement, capacitive values could be reduced as low as the femtofarad range. Commercial humidity sensors generally have nominal capacitance values in the hundreds of picofarads and operate with a few hundred picofarad range [87], [88]. However, MEMS capacitive sensors often have capacitive readouts that are smaller, in the atto- to femtofarad range [89] [90] [91]. The Irvine Sensors MS3110 capacitance to voltage converter, designed for MEMS capacitive sensor readout, has a noise floor of 4 af/rtHz [92], which sets a minimum possible capacitance resolution. However, as discussed, capacitances in the femto- to atto-farad range would not be currently compatible with an RF system in the high kHz to mid MHz band.

The increasing of capacitive sensing values of MEMS is important for sensor integration with the readout circuits. Fabricating a sensor with a larger capacitance not only reduces the circuit's osculating frequency, it also reduces the apparent effects of noise in the device. One method to increase this sensitivity is to increase the sensor size while maintaining small capacitive gaps. However, this technique reduces the mechanical natural frequency of the device and makes it more vulnerable to low frequency mechanical vibrations often present due to pumps and other machinery in the geothermal systems.

The fundamental physics behind variable capacitors must be understood to determine the optimal method for increasing capacitance. Capacitive values are based on the equation $C = \frac{\varepsilon * A}{d}$ were ε is the dielectric constant of the medium between the two parallel electrodes, A is the overlapping area of those electrodes and d is the distance between the electrodes. A basic parallel plate capacitor can be seen in Figure 3.2. The dielectric material between the two materials is usually set for a given design with a given environment. A dielectric stack including air and a thin film dielectric is common in variable capacitors. For out-of-plane sensing, the distance between the two electrodes changed to change the device capacitance. For in-plane devices either the distance or the overlapping area of the electrodes can be varied.

The transduction of temperature to a capacitive signal requires that a variable capacitor changes with a change in temperature. For a passive device, inherent physical properties of materials can be used to translate changes in temperature to changes in physical dimensions. The coefficient of thermal expansion (CTE) is a common property used for this type of transduction. Capitalizing on the CTE mismatches of different materials is an effective
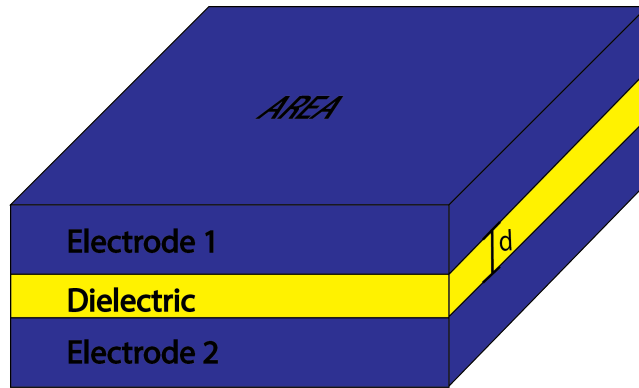
Figure 3.2. A basic capacitor diagram. The dielectric can be a set distance (d) for static capacitors and can vary for variable capacitors. Overlapping areas can also be static or dynamic depending on the system's design.

method for measuring static ambient temperatures. A CTE mismatch can be utilized in sensor design to move patterned sensor features relative to other features as shown in Figure 3.3. This relative motion can be measured using physical effects such as frequency shifts of resonators, resistance change due to induced stress in piezoresistive materials, capacitance changes from moving parallel plate systems, as used in this research, or other phenomena.
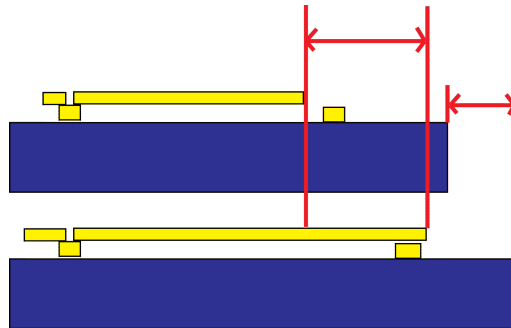
Figure 3.3. Both substrate and released device expand, but CTE mismatch makes the device expand more in this case.

While a device layer can be carefully selected in combination with a substrate to maximize their relative motion, this is often not enough physical motion to transduce a measurable electrical signal. Larger displacements can be generated through the use of a bimorph structure. This is a common practice in the fabrication of existing MEMS passive, capacitive temperature sensors.

Bimorphs behave like bimetallic strips in that as the structure experiences a change in temperature, one of the materials expands or contracts more than the other material due to their dissimilar CTEs. This differential CTE induces a bending moment on the system, which results in tip deflection. The MEMS process is ideal for making out-of-plane bimorph structures as devices are fabricated using layer by layer deposition techniques. Bimorphs are

50

modeled using the bimorph equation generated by Timoshenko, which describes structure deflection [93].

$$y = \frac{3L^2 \Delta T (\alpha_a - \alpha_b)(t_a + t_b)}{\frac{E_b t_b^3}{E_a t_a} + \frac{E_a t_a^3}{E_b t_b} + 6t_a t_b + 4t_a^2 + 4t_b^2} \tag{3.4}$$

This equation describes the bending shown in Figure 3.4. In this bimorph structure it is clear that the motion is in an arc rather than rectalinear.
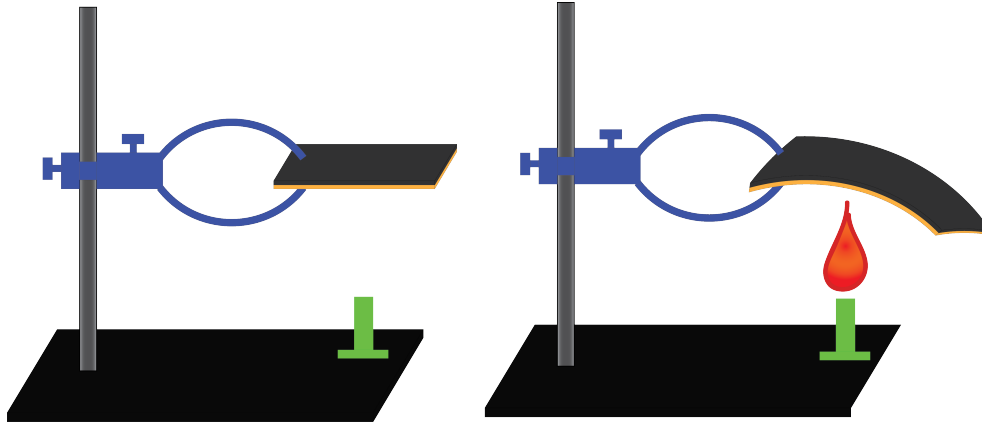
Figure 3.4. A bimetallic strip bent due to mismatched CTE values leading to differential thermal expansions when heated.

A single bimorph structure can be used as the top electrode in a parallel plate capacitor. The bottom plate can be static allowing the top electrode to move close to it, and in some cases come into contact. This type of layered MEMS device is shown schematically in Figure 3.5. Another design for out-of-plane bimorphs separates the upper sensing electrode from the bimorphs used to transduce motion from the applied changes in temperature. This type of configuration allows the electrodes to stay planar and parallel to the bottom electrode. Designs utilizing this type of system can achieve linear motion of the top electrode versus temperature. However, based on the capacitance equation, this will yield a $\frac{1}{d}$ relationship for the capacitance versus temperature output. While out-of-plane capacitive devices are inherently non-linear due the change in capacitive plate distance, out-of-plane sensor output can be linearized through the use of arrays of creative capacitive plate geometries [94]. The drawback to this type of system is that arrays of sensors increase system complexity, which is not ideal in a harsh environment.
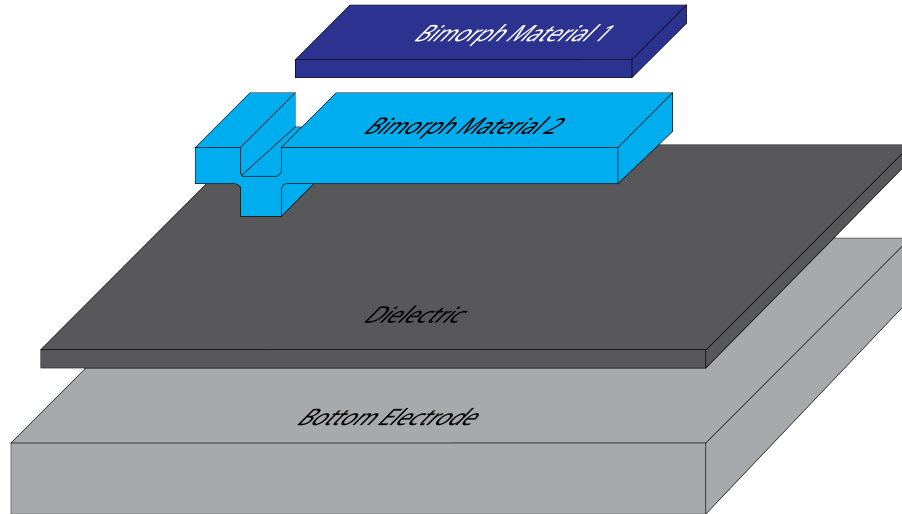
Figure 3.5. Exploded view of an out-of-plane sensing geometry. Two bimorph materials are connected and separated from the bottom electrode by a dielectric material.

3.2 Existing MEMS Capacitive Temperature Sensors

There are many out-of-plane MEMS capacitive devices that function using bimorphs. Four such devices are briefly described below highlighting key sensor performance benefits and drawbacks.

A silicon device, made by the PolyMUMs foundary process [95] was designed by Sohi as part of a combined pressure and temperature sensor [96]. The modeled theory for this sensor shows that it will actuate out-of-plane and sense capacitance in the femtofarad range at temperatures up to 250 °C. This research presents two devices that use bimorph structures for temperature sensitive actuation. One structure has a metal layer fully covering the Si top electrode. The second device has wide bimorph beams attached to the top electrode.

A SiO$_2$ and Al based bimorph temperature sensor was fabricated and tested for long durations recently by Scott [97],[98]. This sensor has been shown to operate at 300 °C with a 600 mus response time. This device is actually 220 individual bimorph structures used to measure a summation of each individual capacitance. A mean room temperature capacitive value of 9.46 pf is reported and changes in capacitance of almost 250 fF over a 275 °C temperature range.

The work of Warren [89] used bimorph structures incorporated into the beams of devices to actuate the sensing area at slightly elevated temperatures up to 50 °C for IR sensing. These sensors were fabricated using a poly-Si device layer and chitin as the bimorph material. Large capacitive plate electrodes were mounted to the bimorph arm sections for signal acquisition. Capacitance measurements were taken over the 5 to 50 fF range.

Another bimorph IR sensor was fabricated by Zhang [99] using different bimorph geometries. Poly-silicon was used as the device layer and chitin was again used as the bimorph

material. While these sensors were measured optically, a similar design could be used to collect capacitive data from the device.

3.3 Harsh Environment Compatible Out-of-Plane Temperature Sensor

An out-of-plane prototype was designed based on previously designed silicon-based sensors to show that the common, out-of-plane, temperature sensing device could be made using harsh environment materials. The sensor was then modeled, fabricated, and tested.

3.3.1 Harsh Environment Compatible Out-of-Plane Sensor Design

Materials Selection

The materials chosen for the out-of-plane sensor were selected based on a large differential CTE to achieve larger deflections, and for their intrinsic ability to survive high temperatures. Silicon carbide was chosen for the device layer based on its high temperature compatibility, its high stiffness, and its relatively developed fabrication techniques as compared to other harsh environment materials.

Aluminum was selected for the top layer of the out-of-plane bimorph structure. Its large CTE, around 24 ppm at room temperature, and previous integration to MEMS processing made it an attractive material choice. While aluminum may not be suitable for very high temperature applications at or above 500 °C, it is within its acceptable operational range for the U.S. geothermal wells as 99.98% of U.S. well temperatures are between 90 °C and 400 °C.

Sensor Geometry and Optimization

A simpler, non-touchdown geometry is utilized for the initial harsh environment sensor fabrication using poly-SiC as the device layer. Simple, out-of-plane bimorph beam geometries are coupled to a SiC capacitive plate electrode as a proof of concept for the harsh environment out-of-plane sensor physics. ANSYS was used to model 3 different sensor geometries based on those used for IR sensors in previous work by Zhang [99]. The sensor arm lengths, shown in Figure 3.6, are varied for different temperature ranges and resolutions.

In addition to sensor geometries, residual film stress has an effect on the sensor performance. The initial sensor position is dependent on each of the film stresses. This initial position affects both sensor resolution and range. The residual stress of the poly-SiC films
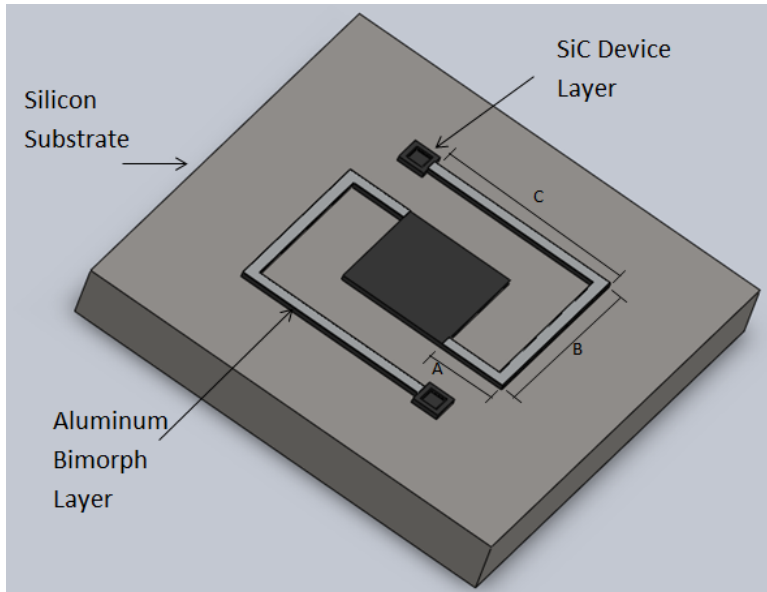
Figure 3.6. Out-of-plane sensor design. Arm lengths A, B, and C are varied among the designs to achieve different sensor responses to temperature.

made in the Berkeley Nanofabrication facility vary based on the film doping and the annealing process. The effects of annealing and doping concentration give a range of SiC stresses from 300 MPa of tensile stress to less than 200 MPa compressive stress. These stress levels are based on a range of annealing processes from no anneal step to 8 hours in argon at 1050 °C and atomic nitrogen percentages from 0 to 0.5. [100].

Sputtered and evaporated aluminum can have a range of stress values, which are power and annealing dependent. DC power has been used to tailor stress levels from 460 to -1438 MPa as shown in Figure 3.7 [101].

Using this simple sensor geometry leads to a non-linear capacitive output within the 90 °C to 400 °C temperature spectrum. ANSYS simulations model the capacitance versus temperature performance for sensors of each design. The simulations vary film stresses, sensor geometries, and layer thicknesses. The layer thickness is shown to have the greatest effect on the temperature sensor range. When thicker metals are used, the dramatic increase in capacitance, seen with all parameter sets, occurs at lower temperatures. This is due to the force that the thicker Al layer can apply to the SiC structure. For a given set of material thicknesses, the higher the stress in the metal film, the greater the device motion at a given temperature. The residual stress of the SiC film within the -500 MPa to 300 MPa range appears to have a minimal effect on the sensor output.

Metal was sputtered across the full device surface of some devices in addition to the bimorph section. This was done to increase initial mass displacement thus moving the sensing range to higher temperatures.

54
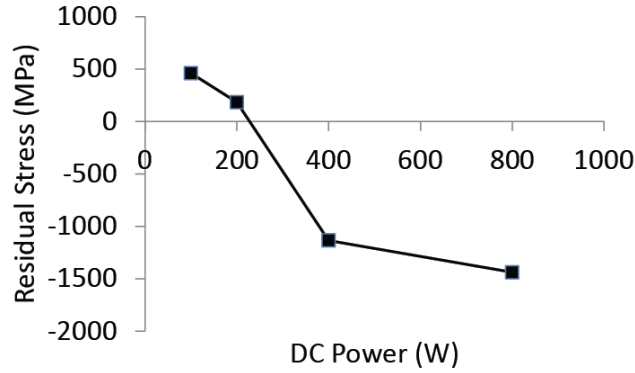
Figure 3.7. Residual stress of DC sputtered aluminum. Films can be made both compressive or tensile depending on DC sputtering power. Data reploted from Chu [101].

	SiC Stress/ Al Stress (MPa)	SiC Thickness/ Al Thickness (μm)
	-100/200	0.5/0.05
	-100/100	1.3/0.15
	-100/100	1.3/0.1
	-100/200	1.3/0.1
	300/100	2/0.15
	-500/500	1.3/0.1
	-100/200	1.3/0.02
	-100/100	1.3/0.02
	-100/300	1.3/0.05
	-100/200	1.3/0.05
	-100/100	1.3/0.05
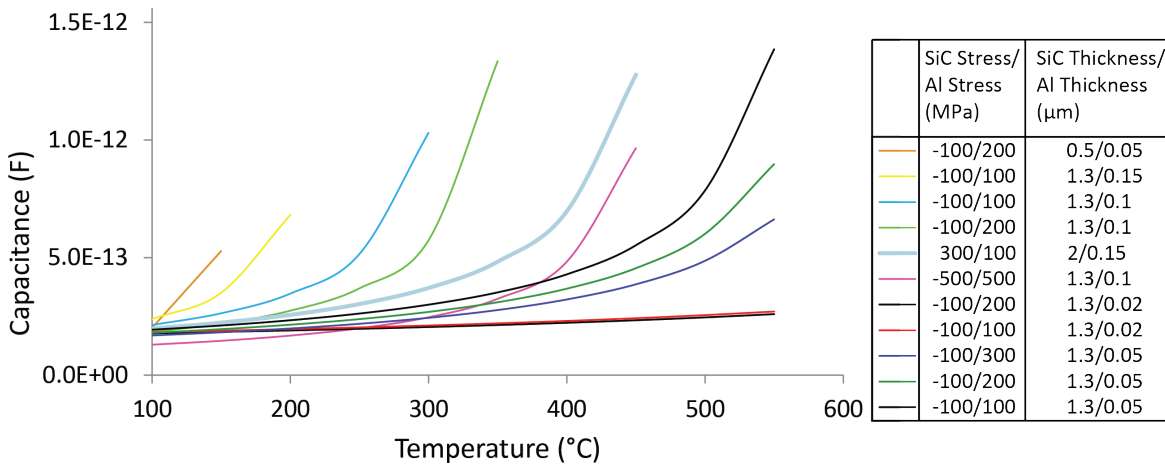
Figure 3.8. Residual stress of SiC/Al (MPa) and thicknesses (μm) of those films were varied in the ANSYS model to determine appropriate parameters.

3.3.2   Out-of-Plane Sensor Fabrication

The fabrication of the out-of-plane sensors is shown schematically in Figure 3.9. This process began with the deposition of a 500 nm low stress silicon nitride (Si_3N_4) layer used for electrical isolation. This deposition was done at 850 °C with 100 sccm dichlorosilane (SiH_2Cl_2) and 25 sccm NH_3 flow rates at 140 mTorr. This was followed by the deposition of 2 μm of poly-Si at 615 °C using silane (SiH_4) as the silicon source gas. This was used as a sacrificial release layer. The poly-Si was etched to make anchor holes using inductively coupled plasma at 13.56 MHz with an SF_6 etch chemistry. A 1.3 μm SiC device layer was deposited at 850 °C using methylsilane (CH_3-SiH_3) for the carbon source, dichlorosilane for the Si, and NH_3 for doping. No annealing step was used to keep the film stress high. A

100 nm thick Al layer was sputtered in an argon environment to coat the bimorph region. DC powers ranging from 250 to 300 Watts were used to keep the Al film stress at a low, positive value. On some of the sensors, another thin Al layer was deposited across the whole device. Initially the Al layer was etched using a heated aluminum etchant at 50 °C for times ranging from 15 seconds to 20 minutes. Each sample's surface was checked for electrical conductivity before the devices were released. While the etch areas were no longer conductive from the Al film, a residue from the Al film remained, see Figure 3.10. The process flow was changed to incorporate a lift-off process using negative photoresist rather than etching the Al film. The devices were then released by etching the sacrificial Si layer with XeF_2.

The final fabricated devices with Al on the bimorph section only and with full Al coverage are shown in Figure 3.11 and Figure 3.12 respectively.
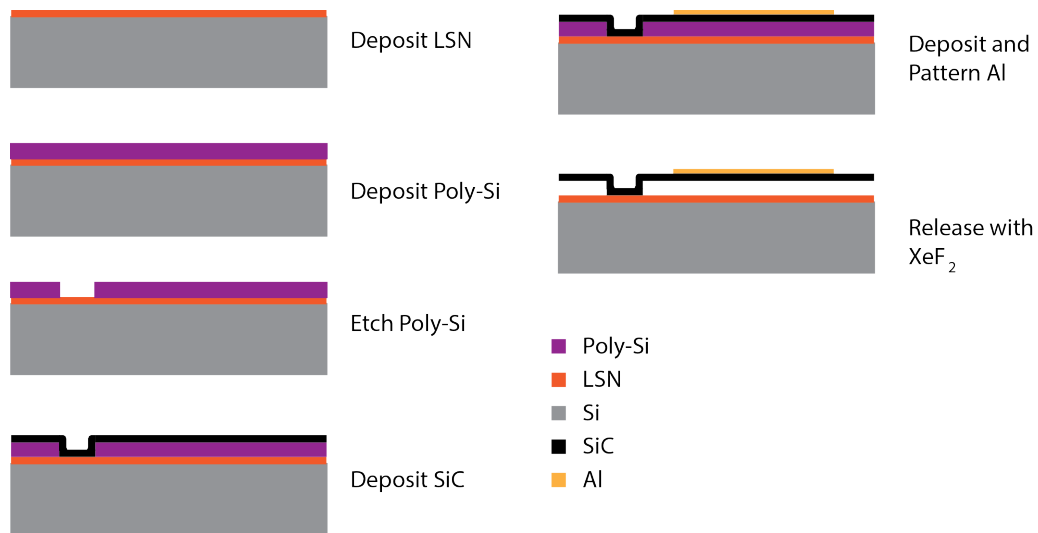
Figure 3.9. Fabrication method for out-of-plane sensors.
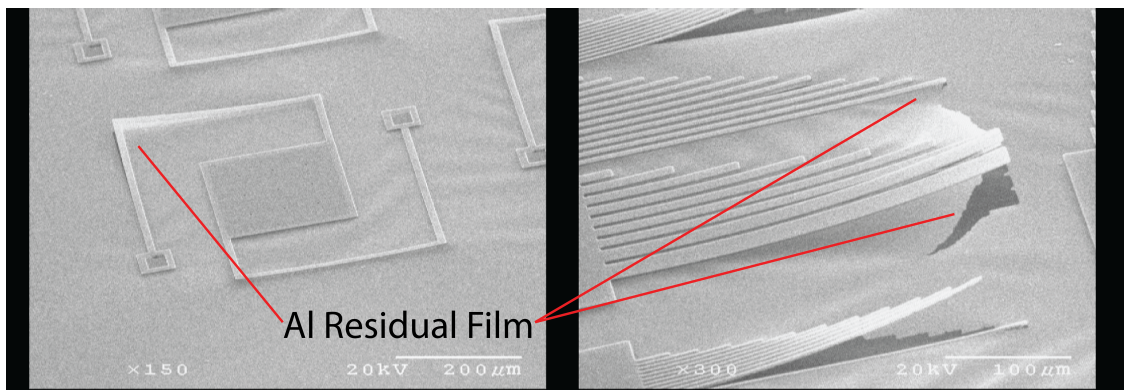
Figure 3.10. Al residue remains from the Al etching process.

56
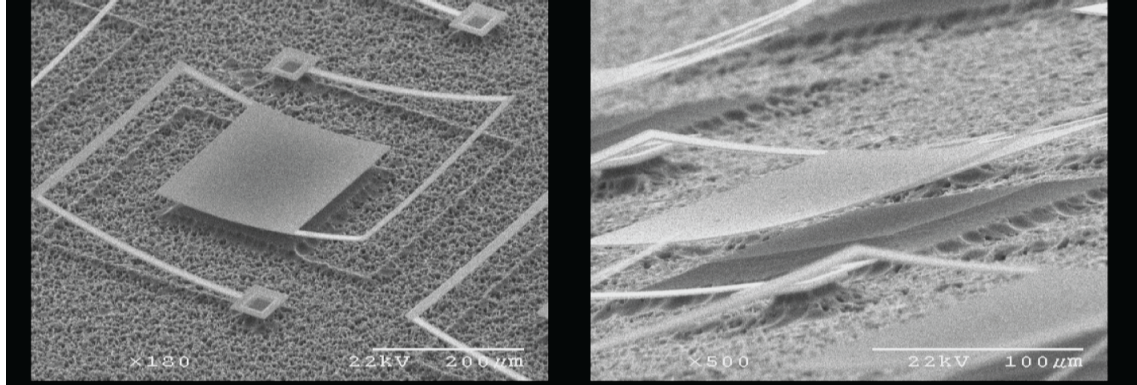
Figure 3.11. (Left) Isometric view of released out-of-plane device with Al as the bimorph material on the arms. Over etching with the XeF_2 resulted in substrate scalloping. (Right) The medium length arm device mass is suspended approximately 5 μm above the substrate.
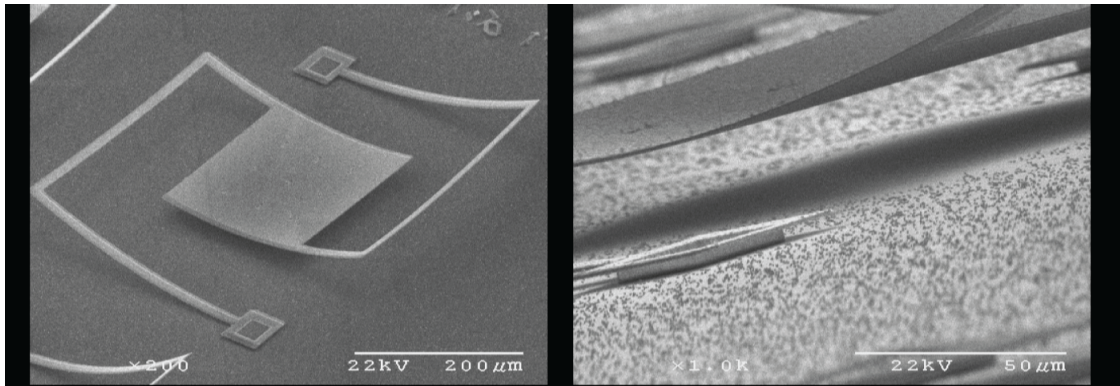
Figure 3.12. (Left) Isometric view of released out-of-plane device with a layer of Al across the whole device layer. (Right) The medium length arm device mass is suspended approximately 10 μm above the substrate.

3.3.3 Out-of-Plane Sensor Testing

The sensors were tested using a LCR meter to measure the capacitance change with temperature. A white light interferometer was used to measure the out-of-plane displacement versus temperature. For the out-of-plane displacement measurements, a 50 Watt, 5x5 mm heater was mounted below the optics of a Wyko NT3300 profiling system with a light center frequency around 600 nm. Two dimensional profiles, generated from three dimensional plots, like the one shown in Figure 3.13, were used to determine sensor motion. Height measurements were verified with distances measured using SEM images.

The white light interferometry measurement technique was limited by the radiative interference from the heater at higher temperatures. A maximum temperature of 350 °C was
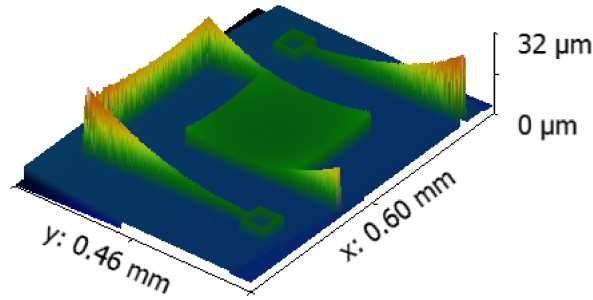
Figure 3.13. Out-of-Plane displacement image of partially released medium length leg sensor at room temperature.
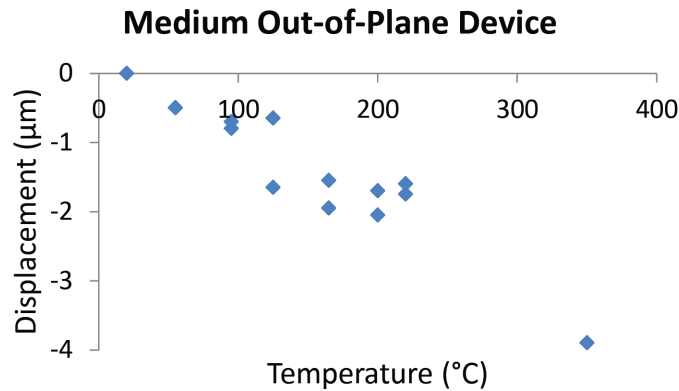
Figure 3.14. Out-of-plane displacement measurements of medium length leg sensor up to 350 °C.

recorded and is shown in Figure 3.14. A larger optical working distance would be required to record higher temperature motion.

Capacitive data was collected using an Agilent E4980A Precision LCR Meter. Data was taken at 100 kHz with a 1 volt signal amplitude. A probe station was used to contact the device. A probe with attached bottom electrode was used to collect the capacitive signal. A capacitance increase of 1 pico-Farad is seen between 20 °C and 80 °C in Figure 3.15. The touch down of the sensor occurs at approximately 100 °C. This is a lower temperature than seen with the WYKO displacement measurements as the bottom electrode probe tip changed the apparent initial sensor displacement. For higher temperature electrical sensing, a bottom electrode and larger initial plate spacing is required. The capacitive signals that are measured are non-linear versus temperature as expected. The linear displacements measured with white light interferometry dictate this $\frac{1}{d}$ capacitance relationship.
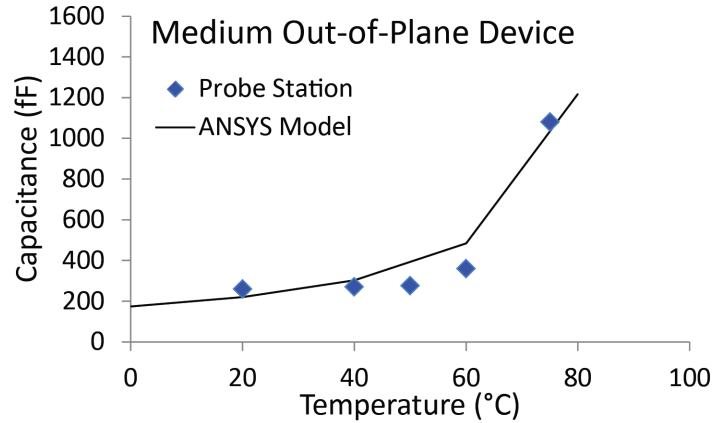
Figure 3.15. Capacitance measurements of medium length leg sensor up to 100 °C.

3.4 Ruggedizing State-of-the-Art Temperature Sensors Summary

There are many types of temperature sensors that are currently in use in many applications to meet varying requirements for temperature range, resolution, stability, harsh environmental compatibility, as well as many other parameters. MEMS sensors, and particularly passive, capacitive MEMS sensors are desired for the down hole geothermal environment. These sensors can be designed to operate within the desired range with the desired resolution for geothermal wells. They are small in size, which will reduce geothermal well obstruction. A suite of MEMS sensors can be fabricated and incorporated into an RLC circuit to be read passively utilizing RF technology.

There are many existing MEMS temperature sensors. Of the passive, capacitive MEMS temperature sensors, they are mostly out-of-plane actuated devices. Existing devices have been fabricated using silicon as the device layer, which limits the upper temperature sensing limit. A harsh environment compatible device was modeled after an existing silicon device design. It was fabricated using silicon carbide as the device layer to increase the potential operational temperatures. This sensor was tested up at 350 °C to show is functionality.

The main drawback with the out-of-plane sensing devices is the inherently non-linear capacitive output. The systems that have been implemented to achieve a linear signal using out-of-plane MEMS add system complexity, which can lead to a higher rate of failure in harsh environments. In-plane capacitive sensors can be designed to achieve a more linear output signal with temperature.

59

Chapter 4

In-Plane Temperature Sensors

In this chapter in-plane MEMS temperature sensors for down hole geothermal environments are designed, optimized, fabricated, tested, and analyzed. While the more common out-of-plane temperature sensors can be made from harsh environment materials, as shown in the previous chapter, in-plane temperature sensing offers the potential for more linear signal outputs with single devices rather than signal summations from multiple out-of-plane devices.

4.1 In-Plane MEMS Temperature Sensor Design

Single in-plane capacitive sensors can be designed to be more linear than out-of-plane capacitive sensors due to the relationship between capacitive electrode spacing and electrode overlap area with capacitive output. They have the additional advantage that both sensing electrodes can be fabricated on the same device layer. There is no direct need for top and bottom electrodes requiring individual lithographic masking steps.

4.1.1 In-Plane Capacitance Sensor Physics

Traditionally, in-plane, capacitive, or electrostatically actuated MEMS sensors are fabricated with either inter-digitated comb finger or parallel plate electrodes. In an in-plane system the motion between the two plates is either perpendicular or parallel relative to each other for parallel plates and comb fingers respectively. These relative motions can be seen in Figure 4.1
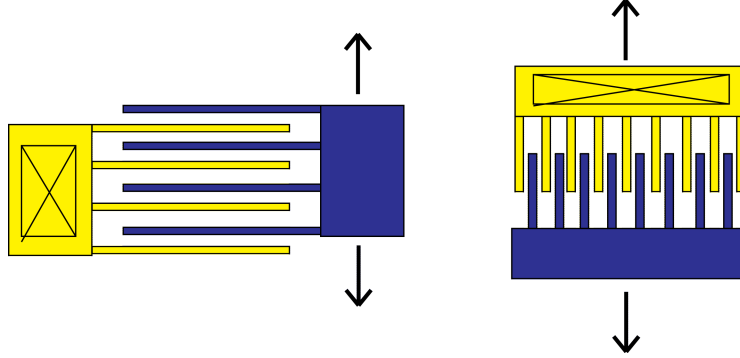
Figure 4.1. (Left) Simple parallel plate capacitive sensing electrode geometry. The fingers move due to the relative motion of the substrate to which the yellow fingers are mounted and the motion of an external mechanical system attached to the blue fingers. (Right) Simple inter-digitated comb finger capacitive sensing electrode geometry. The yellow fingers are anchored to the substrate and move relative to the blue fingers, which are attached to an external system, which moves the fingers up and down. In both of these systems the fingers elongate in addition to the motion of an external system. This adds to the sensed capacitance.

Basic Linear Systems

As with the out-of-plane temperature sensor designs, the external mechanical system attached to capacitive sensing electrodes is responsible for the majority of the motion in the system. The simplest method for achieving this motion is through the thermal expansion of a single device layer patterned on top of a substrate with a different CTE. This allows features anchored in one location on the substrate to move relative those anchored in a different location. This method requires long beam lengths to achieve large displacements as expansions due to CTE are based on original lengths. Figure 4.2 shows an example geometry for a basic inter-digitated comb finger temperature sensor design. The CTE mismatch between the device layer and the substrate causes the comb fingers to move relative to the sensing electrodes.

The change in capacitance, ΔC, versus temperature, T, can be calculated based on the sensor's geometry and the capacitance equation. Initially, it can be assumed that there is only one finger branch on each side of the anchor and the number of fingers, N, is half the total fingers on the branch, as one side of the branch interdigitates while the other side separates. While the capacitance of the fingers on both sides of the branches is measured, the signals are kept separate as the change in capacitance on each side will be equal and opposite. This phenomenon can be used to acquire a differential signal if desired. The initial capacitance is based on the initial overlapping area between comb fingers, A, and the distance, d, between those fingers as defined by the initial overlapping length, $OL_{initial}$, and finger thickness, t.

61
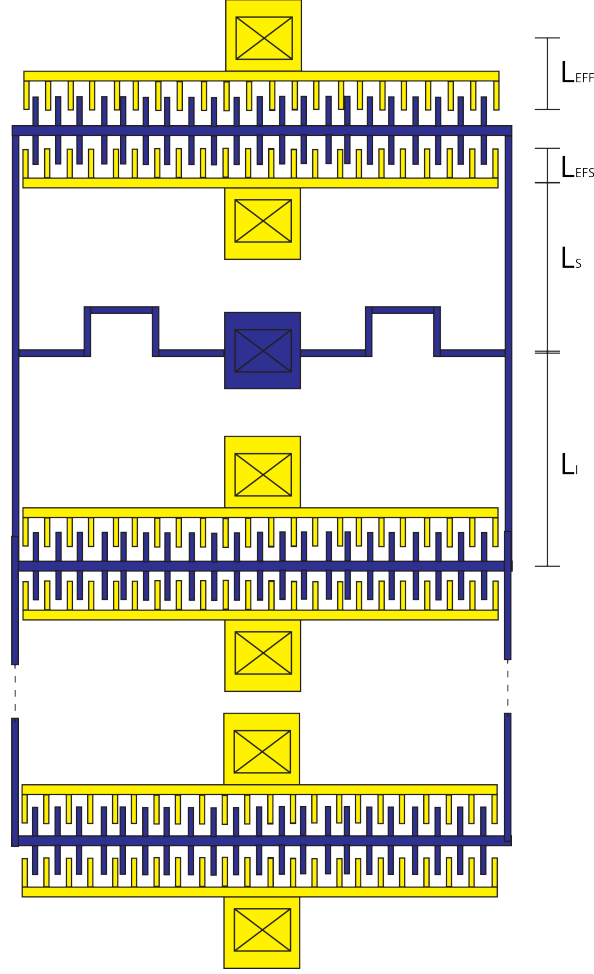
Figure 4.2. Example of an inter-digitated comb finger temperature sensor operating on the principle of CTE mismatch between the substrate and the device layer. Key dimensions are labeled. An extra branch of fingers is shown on the bottom, but branches would be added equally on both sides.

$$C = \frac{\varepsilon A}{d} N \tag{4.1}$$

The change in capacitance is based on the changing overlapping area, $\Delta ol * t$, of the comb fingers versus temperature.

$$\Delta C = \frac{\varepsilon t \Delta ol}{d} N \tag{4.2}$$

The thickness is constant and determined by fabrication parameters. The permittivity, ε, is based on material and environmental properties. The value of Δol, should be maximized to achieve the largest change in capacitive. For this design the overlap is based on both the movement of the device layer and expansion of the substrate. These motions are based on

the thermal expansion of the device beam lengths L_S and L_I, the sense finger length L_{EFS}, and the sense anchor to combfinger tip length L_{EFF}

$$\Delta ol = \Delta L_S + \Delta L_{EFF} + \Delta L_{EFS} - \Delta L_I \tag{4.3}$$

$$\Delta ol = CTE_A L_S \Delta T + CTE_B L_{EFF} \Delta T + CTE_A L_{EFS} \Delta T - CTE_B L_I \Delta T \tag{4.4}$$

Assuming that $L_{EFF} = L_{EFS}$ then:

$$\Delta ol = \Delta T(CTE_A(L_I + 2L_{EFS} + OL_{initial}) - CTE_B L_I) \tag{4.5}$$

If we then assume that:

$$2L_{EFS} + OL_{initial} << L_I \tag{4.6}$$

Then:

$$\Delta ol = \Delta T * \Delta CTE * L_I \tag{4.7}$$

This yields a linear relationship between temperature and the change in the overlap distance. Plugging 4.7 into the capacitance equation 4.2 gives a linear relationship, Equation 4.8, between temperature change and capacitance change.

$$\Delta C = \frac{\varepsilon * t * \Delta T * \Delta CTE * L_I}{d} N \tag{4.8}$$

The linear relationship is good; however, a large displacement is needed to achieve reasonable sensor resolution. To increase this resolution, more branches for sense fingers can be added to the design as shown in 4.2. However, this adds non-linearities to the capacitive readout. An equation to show these additional non-linearities, Equation 4.9, assumes a constant branch spacing, B_S, an even number of branches, N_B, on each side of the anchor, and an even number of fingers on each branch.

$$\Delta C = \frac{\varepsilon * t \sum_{k=0}^{N_B-1} \Delta T \frac{N}{N_B}(kB_S + L_S + L_{EFS})CTE_A - (kB_S + L_I + L_{EFF})CTE_B)}{d} \tag{4.9}$$

Parallel plate capacitive electrode geometries can be used to increase the sensor resolution. Slightly different equations are generated for parallel plate sense fingers. In this case, rather than the finger overlap changing due to thermal interactions, the gap distance between the fingers changes.

The same initial capacitance equation, Equation 4.1, is used; however, the change in capacitance is based on a change in the plate spacing.

$$\Delta C = \frac{\varepsilon A}{\Delta d} N \tag{4.10}$$

Based on the same arm structure geometry as in Figure 4.2, and replacing the inter-ditigated fingers with parallel plates makes $\Delta d = \Delta ol$ from Equation 4.7.

Plugging Equation 4.7 into Equation 4.10 gives:

$$\Delta C = \frac{\varepsilon A}{\Delta T * \Delta CTE * L_I} N \tag{4.11}$$

With this sensing geometry, the whole area of the parallel plate capacitor changes its location relative to the sensing electrode. This allows for a larger change in capacitance with temperature. However, this yields a non-linear relationship between temperature and capacitance. As with the inter-digitated comb finger design, the addition of more branches with parallel plate sensing fingers increases the system's non-linearity.

To maintain linearity within the system, the optimum solution is to increase the motion of a single branch of inter-digitated comb fingers. This is difficult to achieve when only using linear thermal expansion of individual materials. For this reason, other configurations are investigated to determine methods to increase the system's displacement with a temperature change.

Bimorphs

A bimorph structure can be used to induce in-plane beam bending, increasing displacements due to temperature change. This will in turn increase the motion of the capacitive sensing structure. This is similar to the bimorphs used in the out-of-plane sensors; however, the dissimilar materials are side-by-side rather than stacked in the vertical direction. The in-plane motion can be seen from a top view in Figure 4.3. In this bimorph structure, like that of the out-of-plane bimorph, tip deflection motion is in an arc rather than at right angles to the beam structure. Attaching comb fingers to the end of a single bimorph beam would require fabrication of comb fingers with a similar arc shape to achieve a linear signal. However, using two bimorphs with a connecting beam, as shown in Figure 4.4, allows for the rectilinear motion of an attached sensing unit if connected at the center of the device. This somewhat reduces the displacement of the capacitive plates and thus the sensor resolution. However, motion is still greater than the motion of a basic linear system. The motion of the double bimorph is a combination of clamped-clamped beam buckling and the bimorph effect. The linear thermal expansion of the single material that spans between the anchors creates enough force to buckle the structure. The direction of this buckling is controlled by the biomorph section, which forces the structure to buckle in the desired direction. Either parallel plates or comb fingers can be attached to this structure to generate the capacitive readout as shown in Figure 4.5.

Other types of capacitive reading units can be fabricated and used for temperature sensor design. Rather than using comb fingers, bottom electrodes can be designed to measure a
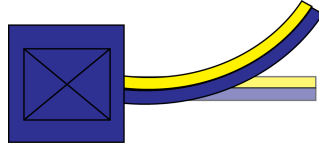
Figure 4.3. Bimorph structure once deformed due to heating.
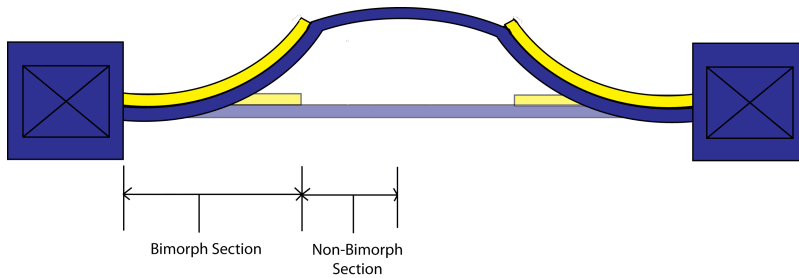
Figure 4.4. Double bimorph connected by single beam deformed due to heating.

capacitance across the gap to the device layer. For an in-plane bimorph, the device layer moves above and across the bottom electrode to generate a change in capacitance with a change in temperature. The can result in large capacitance changes from the motion of large plates attached to the bimorph structure. The in-plane structures with bottom electrodes require more fabrication steps due to this extra electrode layer. A single device layer with comb teeth is fabricated to reduce fabrication complexities while developing the in-plane bimorph fabrication process.

Basic geometric models were generated using the bimorph equation; however, for the more complicated geometries, a finite element modeling tool such as ANSYS was beneficial to optimize the structure's parameters.

4.1.2 Materials Selection

Appropriate device materials must be selected before modeling can be conducted to optimize device geometries. Of the exposed harsh environment materials, the single crystal diamond and micro-crystalline diamond had the best survivability. The SiC did not survive as well as an encapsulation material; however, as SiC can survive the high temperatures, and it has more developed MEMS fabrication techniques, SiC was selected for the main device layer. This will require that the sensor is encapsulated with either a single crystal diamond cap or a micro-crystalline diamond encapsulation layer. The material selected for the other part of the bimorph should have a CTE that differs from SiC so that the bimorph effect can contribute to the motion of the structure. As the sensor is an in-plane bimorph, the second material must be a high quality film and be able to be deposited conformally on the SiC

65
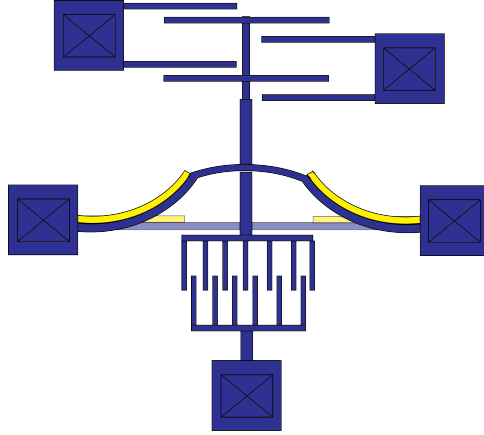
Figure 4.5. Double bimorph deformed due to applied temperature. Demonstrative parallel plate capacitive readouts are shown above the deformed beam and inter-digitated comb fingers are shown below. The double bimorph structure dictates orthogonal motion of the sensing elements.

device structure. For this reason, SiN, SiO_2, and Si were the options provided by the UC Berkeley Nanofabrication facility as they are available for furnace deposition. The CTE of SiC is $4.5*10^{-6}$ ppm/°C. Those of SiN, SiO_2, and Si are $3.2*10^{-6}$ ppm/°C, $0.5*10^{-6}$ ppm/°C and $2.6*10^{-6}$ ppm/°C respectively. The CTE's of SiN and Si are very close to that of SiC, so SiO_2 was selected for the second material. While SiO_2 will not survive the geothermal environment, it will survive the temperatures experienced within the geothermal well. This will not pose a fundamental problem as the sensor will be encapsulated with a suitable harsh environment material.

The substrate material must also be chosen carefully. The buckling effect will be reduced if the substrate expands at a similar rate to that of the device layer. Since the device operates by both buckling and the bimorph effect, this would greatly limit the device motion. For this reason, diamond or quartz would be good options for the substrates with CTE's of $1*10^{-6}$ ppm/°C and $0.33*10^{-6}$ ppm/°C respectively. Sapphire is also an option due to its chemical resistance as shown in the exposure testing chapter. It has a higher CTE of $5.3*10^{-6}$ ppm/°C, but an oxide interlayer could potentially be used to reduce the substrate temperature effects. However, to reduce fabrication complexities while developing the sensing element in this work, Si is used as the substrate. The temporary use of the Si substrate leads to the development of modified sensor designs to decouple the substrate motion from that of the device layer. This is discussed in the modeling section.

4.1.3 ANSYS Modeling

ANSYS models were used to optimize the geometry of the double bimorph structure. The structure is optimized for linearity over the desired 310 °C temperature range. The ratios of the widths of the bimorph beams, and both the length and the width of the bimorph

section to the non- bimorph section, all affect the maximum displacement of this system in the y-direction. The linearization of this structure is done by tweeking the bimorph to non-morph sections, the beam widths, the overall beam length, and the tether spacing. These parameters were varied within a 4 variable design space so that all dimension combinations could be modeled.

ANSYS modeling was done in a 2D design space using plane stress conditions. Tetrahedral meshing elements were selected with a minimum mesh size of 1/2 that of the smallest dimension used in the model. The bimorph structure had 4 meshing elements across its area. The mesh size was decreased and tested to ensure that this larger mesh size would converge at the same values as the more refined mesh size. Initially, 2D models of single bimorph structures were modeled and compared to values obtained using a Matlab code. The Matlab code was used to make a basic analytical model based on Timoshenko beam bending theory for single bimorph structures. One of the basic bimorph structures for which Matlab was used for analysis is shown in Figure 4.6. The Matlab code used temperature independent material properties; however, for basic models, the maximum tip deflection calculated with this code was within 0.2% of that modeled using the ANSYS code for 250 μm long beams over the 310 °C temperature range. The maximum tip deflections calculated using the models diverge more when using larger temperature ranges, with deflections differing by up to 6% for 500 μm beams.
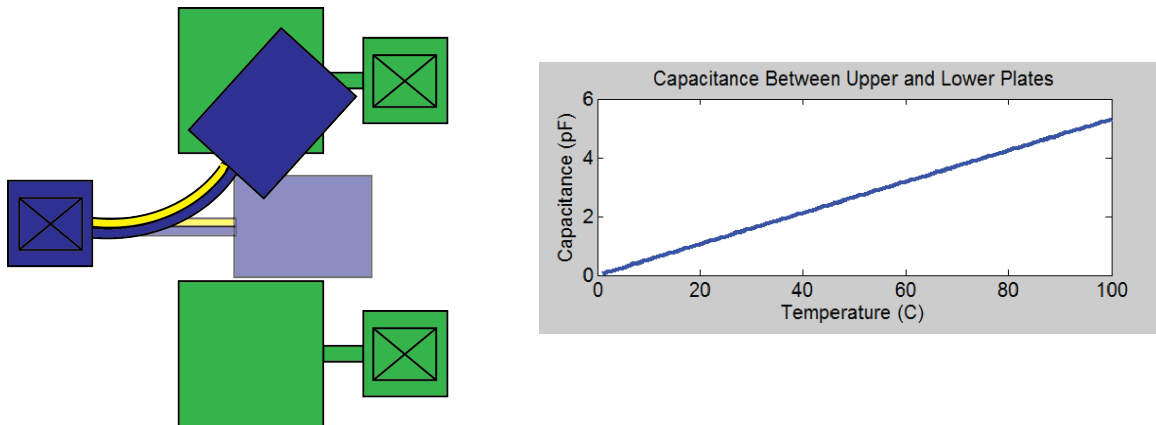
Figure 4.6. (Left) Image from Matlab program written to evaluate basic temperature sensor concepts using first order principles. A bimorph structure with a top and bottom plate sensing electrode is shown in this example. The motion is exaggerated for conceptual understanding. (Right) The capacitive output over 100 °C of this sensor. The Timoshenko equation governs the motion used to calculate the capacitance value shown.

While all of the geometries were varied together to determine the ideal lengths, widths, and spacings, each are described individually to explain the physical principals governing that physical parameters effects on the sensor structure. The first parameter to look at is the ratio of the bimorph to non-bimorph section. The buckling instability can be seen as the ratio of bimorph to non-bimorph section approaches both 0 and 1. In Figure 4.8, a full double bimorph beam with no non-bimorph section is shown deflecting with temperature.
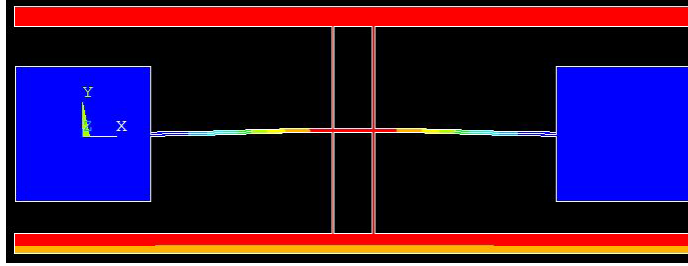
Figure 4.7. ANSYS simulation showing relative deformation in the Y direction of a connected double bimorph structure.

The instability due to the buckling is more dramatic when the whole structure is a bimorph. As the system motion is dominated by the linear thermal expansion, the length ratio of the bimorph to non-bimorph section has a minimal effect on the overall system displacement once the beam has buckled. However, this ratio plays an important role in the linearization of the beam midpoint deflection versus temperature. The most linear relationships between 90 °C to 400 °C are seen with structures with a 1 to 1 ratio of bimorph section length to non-bimorph section length.
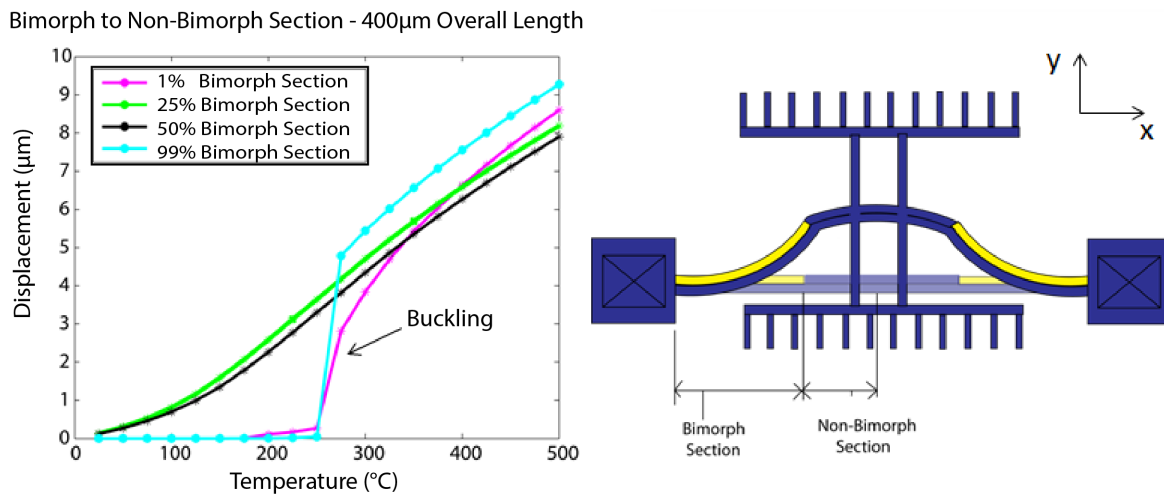
Figure 4.8. Maximum transverse displacement of the center of the 400 μm length double bimorph. The 200 μm full length line (cyan) shows the beam buckling more dramatically than the structures with a smaller bimorph to non-bimorph ratio. The 1 μm length bimorph section also shows buckling; however, due to the different structure material properties, the maximum displacement is different for the two buckling designs.

Next, the effects of beam widths of both materials is modeled. Varying beam widths, see Figure 4.9, of the bimorph section changes both the linearization of the design output and the overall structure displacement. Both similar and dissimilar widths for the two materials

were modeled. For widths between 1 to 5 μm in increments of 0.5 μm, similar widths for both sections yielded more linear outputs versus temperature. A structure with no SiO_2 was also modeled, and a cut out of the SiC was used to control the direction of the structure's buckling. Of those widths the most linear output is shown with 3 μm widths. The thicker the beam becomes, the larger the motional resistance in the y-direction. For this reason, thicker beams do not bend as easily at lower temperatures, and once they begin to bend the rate of displacement increases. With beams that are very thin, on the order of 1-2 μm, initial bending does not require overcoming a large motional resistance. However, the large initial travel cannot continue over the full desired temperature range. As the sensor begins to experience large deflections in the y-direction, the anchors begin to restrict motion. These ANSYS results can be seen in Figure 4.11. The increasing anchor stresses can be seen by looking at the directional stresses in the ANSYS model versus temperature. Looking at the x-direction stresses confirms that the structure begins to resist motion in the y-direction once the sensor has moved beyond a certain distance.

In addition to directional stresses to determine physical phenomonon responsible to motional trends with temperature, ANSYS can be used to determine locations of high stress concentrations. The Von Mises stress is plotted on a basic sensor structure in Figure 4.10. These stresses can be used to determine if the structure will survive a given thermal load or if it may break during operation.
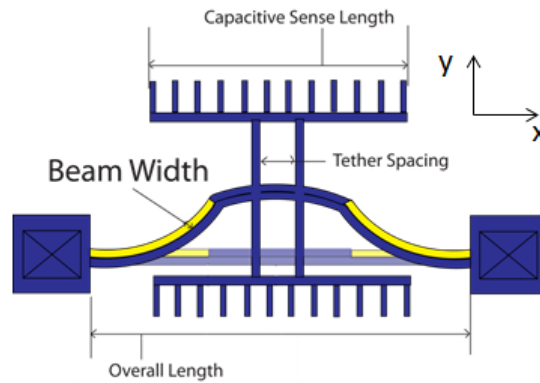
Figure 4.9. The widths of the individual beams (SiC and SiO_2) were varied to determine the most linear displacement of the comb fingers.
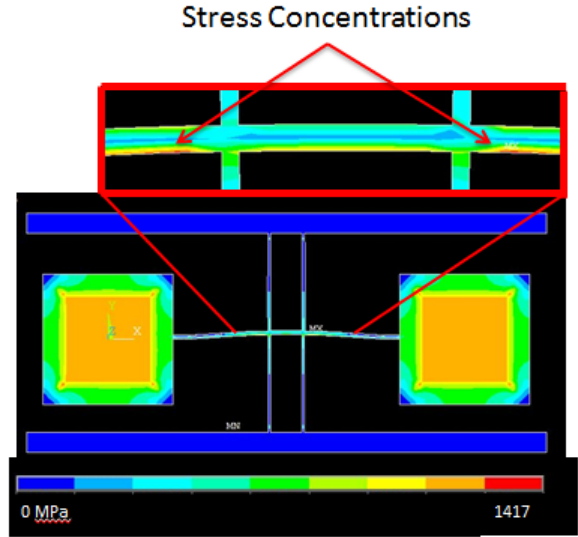
Figure 4.10. ANSYS stress plot for a basic, clamped-clamped, double bimorph structure.
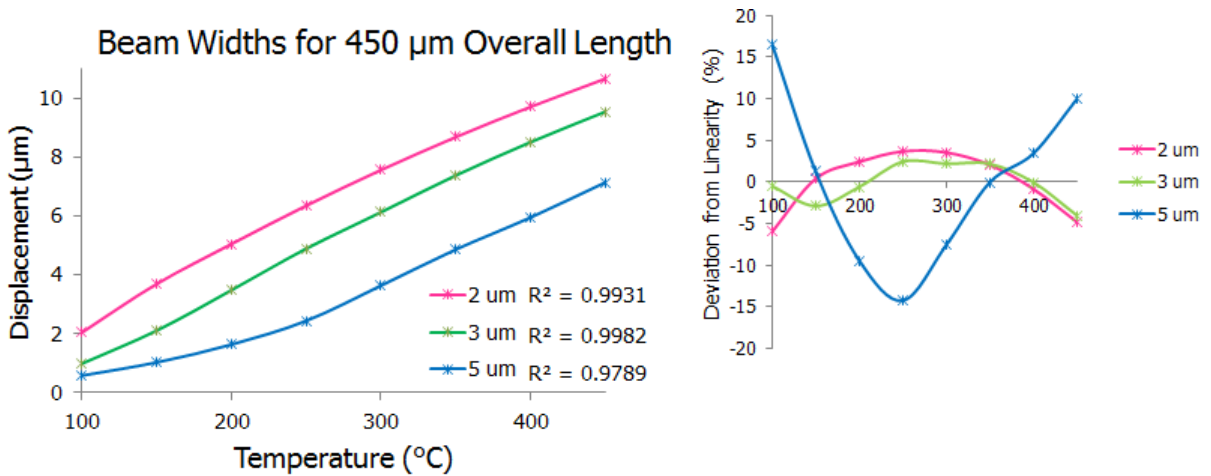
Figure 4.11. (Left) Plot showing displacement versus temperature for equal beam widths of 2, 3, and 5 μm beams. The R^2 values reflect each trend's linearity. (Right) Plot showing the deviation from linearity of the motion of the comb fingers versus temperature.

The tether spacing affects the stress in the center beam, which affects linearity and comb teeth displacement. Tether spacings from 2% to 60% of the overall beam lengths were modeled. The wider the tether spacing, the better sensors torsional resistance, but the lower the comb teeth displacement. The ideal tether spacing is one with the widest spacing with a linear output without sacrificing too much displacement. As shown in Figure 4.12, linear outputs with temperature are achieved between 2% to 10%. For this reason, a 10% tether

70

spacing is chosen for the final design as it will reduce the device's sensitivity to torsion without sacrificing linearity.
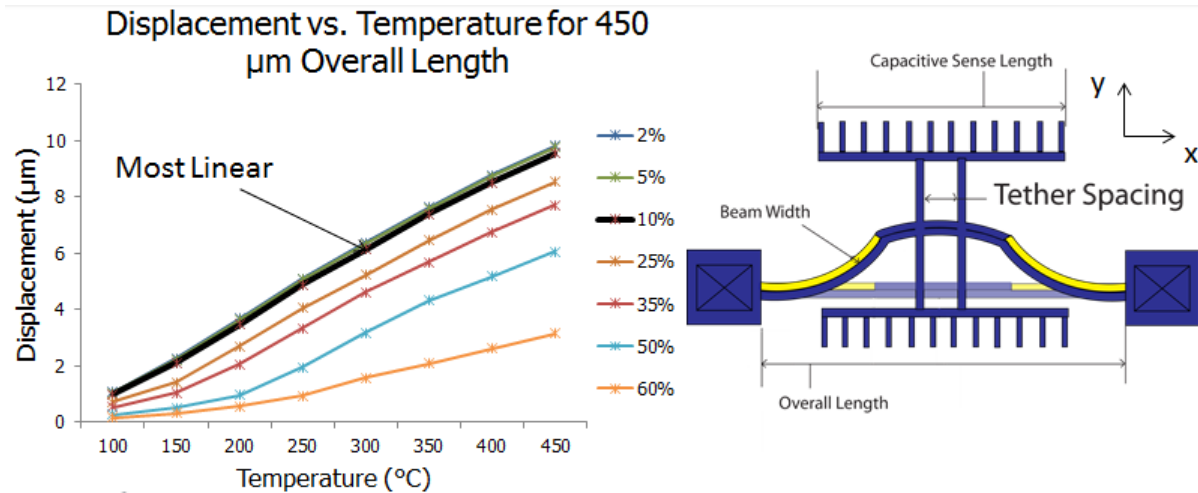
Figure 4.12. The device tether spacing changes both linearity and comb finger displacement. (Left) Plot shows displacement versus temperature for one of the devices. (Right) Image shows tether spacing parameter.

The final dimension to analyze is the overall sensor beam length. The longer the beam length, the larger the overall sensor displacement with temperature. However, increasing the beam length too far leads to a non-linear output. There are two competing phenomena that affect the concavity of the displacement curves shown in Figure 4.13: 1) the Young's modulus decreases with temperature so the displacement would increase with temperature and 2) with displacement, there is an increase in the stiffness of the beams (i.e. more force required to displace the comb structures). With the shorter beams, the Young's modulus dominates so concave up curves are generated, and for longer beams with larger displacement, the increase in stiffness dominates so concave down curves are seen.
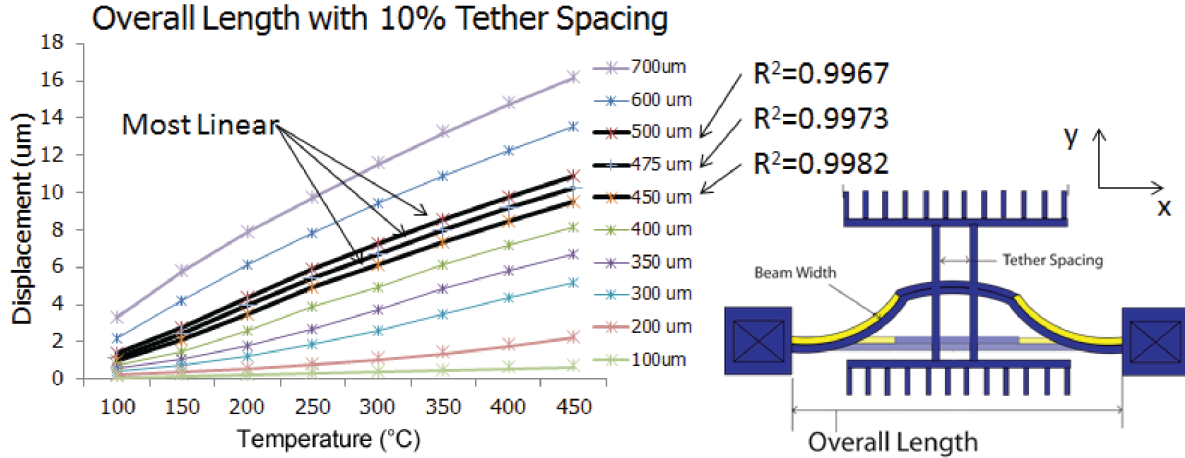
Figure 4.13. (Left) Plot of overall beam length versus temperature. The most linear plots have R^2 values shown. (Right) Graphic highlighting the overall length parameter.

4.1.4 Decoupling the Device from the Substrate

As these sets of sensors will be fabricated on Si substrates which has a similar CTE to that of SiC rather than a harsh environment material with a low CTE, device designs were generated to decouple the device layer from the substrate. The fixed-fixed bimorph originally proposed would allow for the controlled buckling of the beam due to thermal expansion, and the relief of the buildup in stress, which would normally lead to uncontrolled buckling. This type of design works well for sensors with a substrate whose coefficient of thermal expansion is small compared to that of the device layer. With matched substrate and device CTEs, the buckling effect is reduced by the increase in distance between the anchors due to substrate expansion.

The second set of device designs, Figure 4.14, attempts to decouple the substrate expansion from that of the device layer. Both crab leg and folded flexures suspension designs were used to allow for the free expansion of the bimorph beam. This reduces the buckling effect, which increased the in-plane displacement of the first design; however, by adding the suspension system, the moment imposed on the bimorph beam structure boundaries is reduced. This allows for larger beam bending deflections from those seen with fixed-fixed boundary conditions. The extent of the decoupling is shown when comparing the displacement of the device over 500 °C when including substrate expansion versus excluding that substrate motion. The curves shown in Figure 4.15 show all three anchor geometries. The clamped-clamped anchors have the largest difference in displacement over the temperature range. Both the crab leg and folded flexure anchor systems effectively decouple the device layer from the substrate.

72
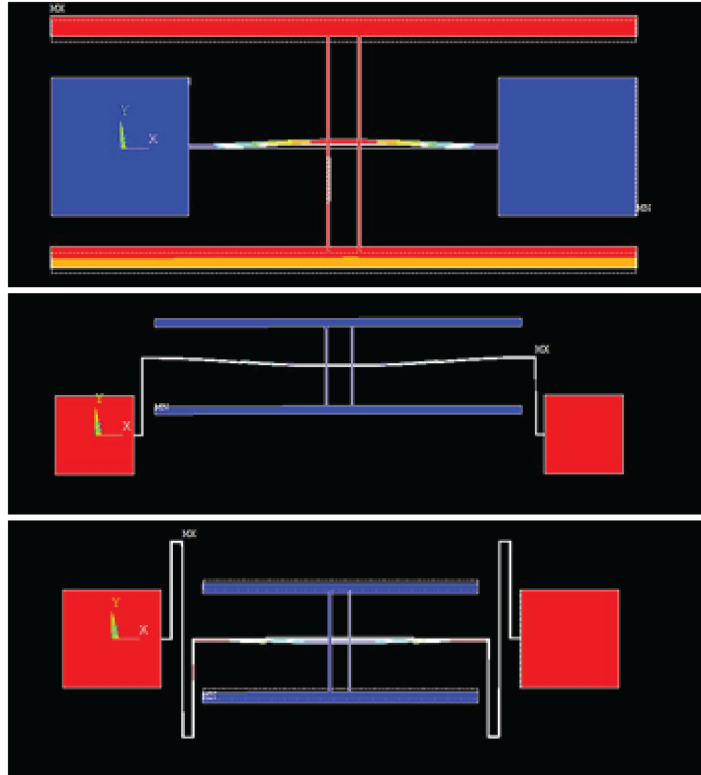
Figure 4.14. (Top) Original clamped-clamped design. (Center) Crab leg anchor design. (Bottom) Folded flexure anchor design.
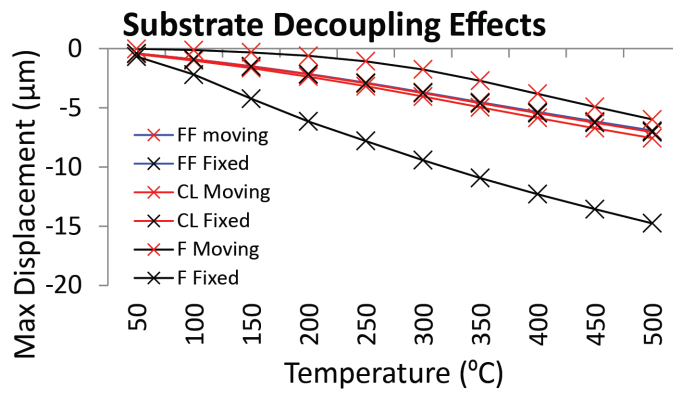
Figure 4.15. Displacement versus temperature for folded flexure (FF), crab leg (CL), and clamped-clamped (F) anchor designs. The closer the Fixed versus Moving curves are, the more decoupled the anchors are from the substrate.

73

4.2   In-Plane MEMS Temperature Sensor Fabrication

All devices were fabricated in the UC Berkeley Nanofabrication facility. The fabrication process was developed in two stages. A thin SiC device layer was used initially to reduce the fabrication difficulties while determining appropriate deposition, etching, and lithographic methods. Once the basic process parameters were understood, the fabrication process was iterated using a thicker SiC device layer. New challenges associated with the thicker device layer were addressed using an iterative approach.

4.2.1   Thin SiC Device Layer

This section details the fabrication of the thin SiC in-plane bimorph temperature sensors with comb finger readouts. These devices were fabricated using the side wall deposition process shown schematically in Figure 4.16.

The first round of sensor fabrication was done using a single, 1.3 μm layer of in-situ Nitrogen doped, 3C-silicon carbide (poly-SiC). The SiC was deposited on Si wafers using a Tystar Titan II low-pressure chemical vapor deposition (CVD) reactor furnace using 1,3-disilabutane, dichlorosilane, and ammonia at 170 mTorr and 800 °C. The SiC was then annealed for 10 hours in a Tystar Titan II furnace at 1050 °C in argon. In a parallel fabrication process, a 2 μm SiO_2 layer was deposited as electrical insulation between the Si and SiC.

An undoped SiO_2 hard mask was deposited using a Tystar Titan II furnace at 450 °C and etched using a photoresist mask in a Lam Research etcher with a fluorine-based chemistry. The SiC was then etched in a Lam Research etcher using a chlorine based etch chemistry. The oxide mask was the removed in an HF wet etch.

The sidewall SiO_2 was then deposited in a conformal layer using the same Tystar furnace. The oxide was anisotropically etched using a RIE process. This process left oxide stringers on the sides of all of the SiC features. The desired oxide side walls were then coated with photoresist. The undesired oxide walls, left unprotected, were etched with buffered HF. The photoresist was then removed.

Metal contact pads were patterned using a double layer photoresist lift-off process. The dies were then diced and the sensors were released using XeF_2 to selectively etch the underlying silicon substrate. One of the released devices can be seen in Figure 4.17. The process details are given in Appendix B.
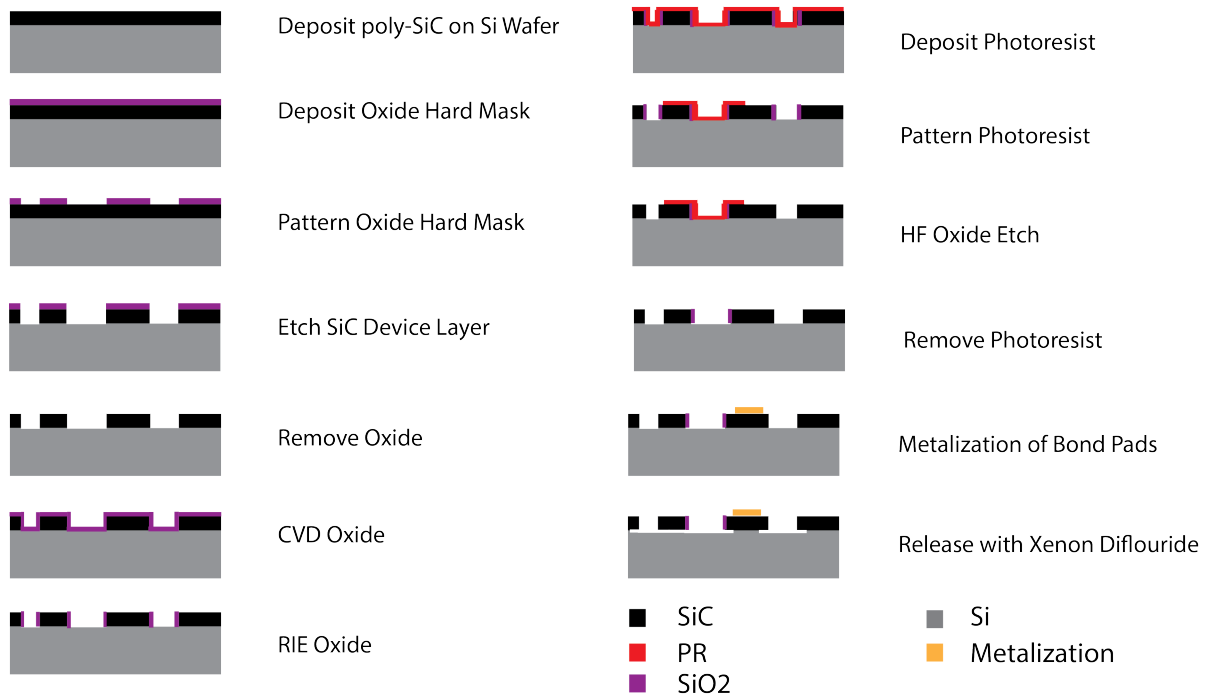
Figure 4.16. Fabrication process for thin device layer in-plane bimorphs.
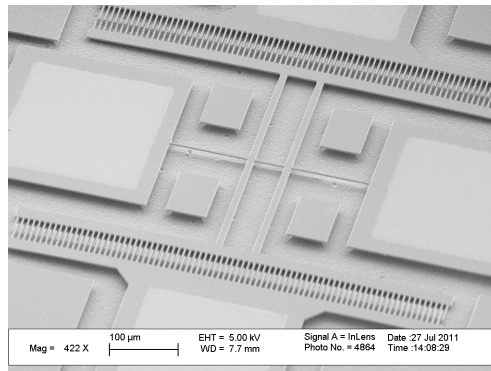
Figure 4.17. Released poly-SiC temperature sensor.

Once released, a strain gradient through the SiC layer became apparent. This strain is shown in the out-of-plane misalignment of the comb fingers shown in Figure 4.18. Another way in which the fabrication diverges from the theoretical is in the etched angles of the SiC wall profiles. Ideally, the SiC structures would have 90° sidewalls; however, once released, the angle of the SiC etch can be seen. Based on a 1.3 μm thick SiC layer, a 68.2° angle was etched. A top view of the side walls at the comb teeth can be seen in Figure 4.18. Successful patterning of the SiO_2 oxide side wall can be seen in Figure 4.19. The oxide is a similar

width and height to the SiC device layer. Once the process parameters were determined, thicker SiC device layers were used to fabricate the final devices.
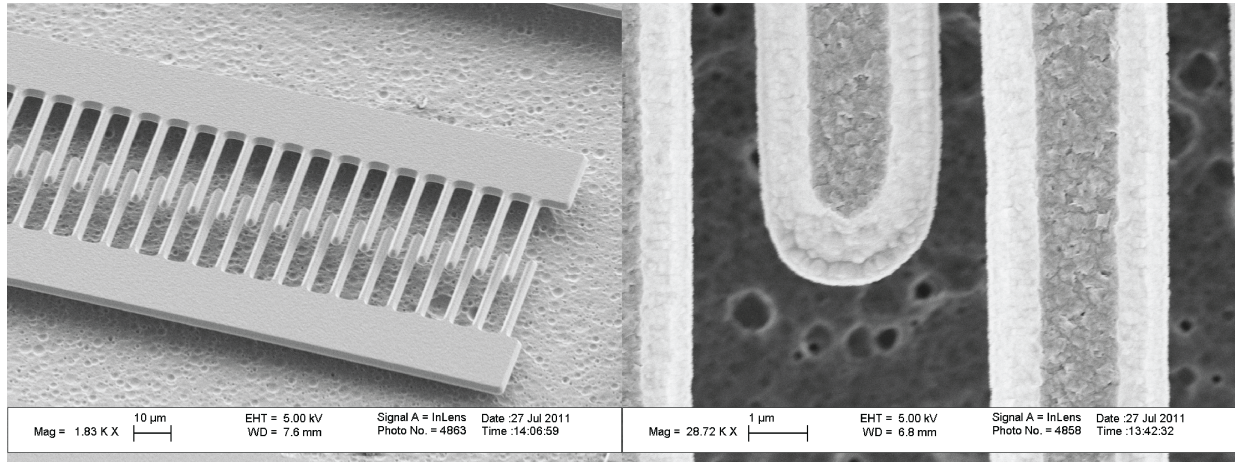
Figure 4.18. (Left) Poly-SiC stress in comb fingers. (Right) Comb-fingers close-up.

Figure 4.19. The side wall oxide next to the SiC structure.

4.2.2 Thick SiC Device Layer

Thicker SiC layer devices were fabricated once the SiC processing parameters were developed. The fabrication process was based on the thin SiC process. SiC was deposited using the same deposition process used for the thin SiC layers. However, to keep film stress down, thick layers were deposited with a series or 1.3 μm SiC depositions each followed by an annealing step. This fabrication process was done on 6" wafers rather than the 4" wafers used in the previous fabrication process. This switch was done to improve the SiC etch side

wall profiles. The etching tools used for fabrication are set-up for 6" wafer processes. The fabrication of 4" wafers requires the use of 6" handle wafers. This adds a thermal isolation layer that prevents proper wafer cooling during the plasma etch steps. This additional heating is detrimental to the etch process. Switching to the 6" wafer format improved the SiC side wall from 68.2° to 87°. A new mask set was used to incorporate the sensor designs that decouple the devices from the substrate by reducing moments at the anchors. While strain gradients were minimal with the 4" wafers, there was a strain gradient problem seen with thinner, less than 2 μm, SiC layers when using 6" substrates.

SiC Strain Gradients

Large positive strain gradients for SiC deposited directly on Si and on SiO_2 are shown in Figure 4.20. It is possible that the annealing step leads to larger strain gradients; however, with thicker SiC layers shown in Figure 4.21, this strain gradient switches from positive to negative and is greatly reduced. It is unclear as to why there were large strain gradients in the thin 6" substrate films that were not observed with the 4" substrates, which also had thin SiC layers. However, location of wafers in the furnace during deposition my be partially responsible. The strain gradients measured with the thicker lower strain gradient SiC are less than the minimum strain gradients seen in the literature, which report values on the order of the upper 10^{-4} μm^{-1} to the low 10^{-5} μm^{-1} range [100].
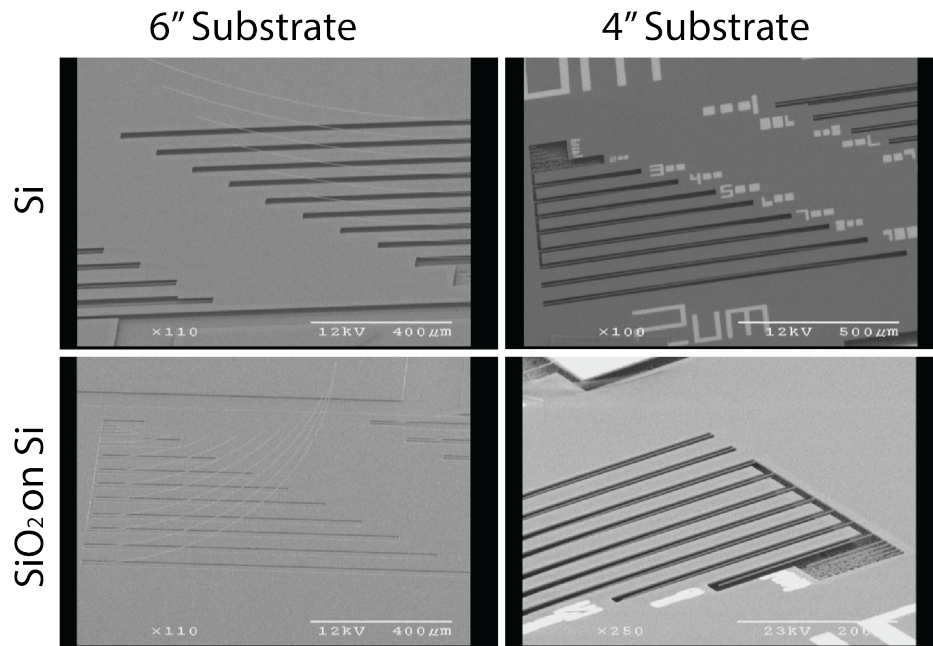
Figure 4.20. Released SiC structures. All structures are 1.3 μm thick. Structures are either directly on Si, released with XeF_2, or on SiO_2, released with HF vapor. The 6" substrates on the left have a large positive strain gradient, while the 4" substrates on the right have a small negative strain gradient.
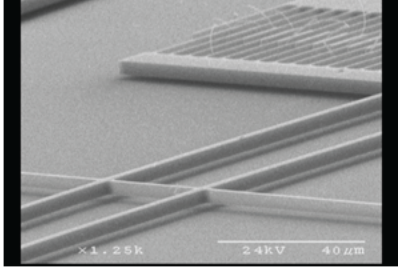
Figure 4.21. Released 4 μm SiC structures. There is a small negative strain gradient. Comb fingers appear to be aligned over a 100 μm distance.

While the released structures appear to be flat with the thicker SiC films over short distances, over longer distances a negative strain gradient can be observed. SiC films of 3.9 μm, 5.2 μm, and 6.5 μm were used to determine how the thickness of the SiC film would change the strain gradient due to both change in geometries and extra annealing steps used in the processing. Figure 4.22 shows that the strain gradient appears to be slightly less negative with SiC film thickness. However, even with the 6.5 μm thick device layer, the comb teeth at 200 μm are no longer fully interdigitated due to the film strain gradient.

T = 3.9 μm   T = 5.2 μm   T = 6.5 μm
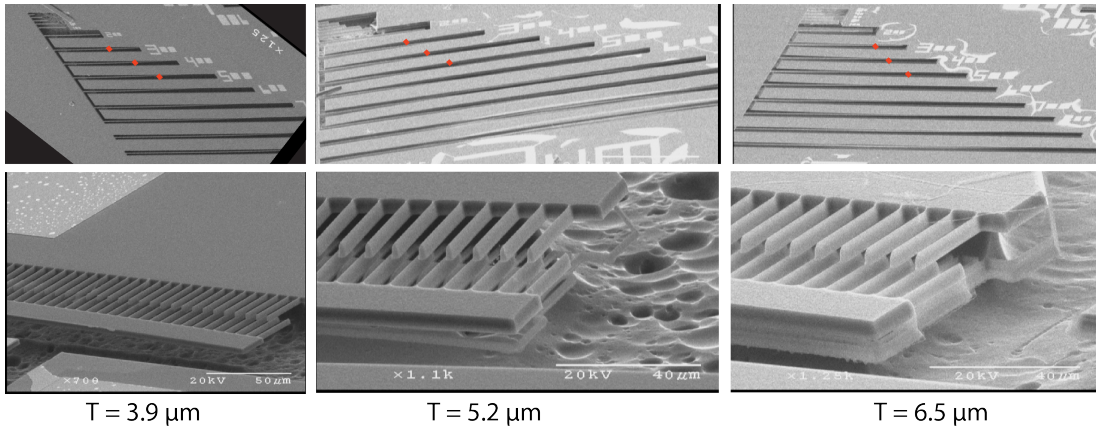
Figure 4.22. (Left) 3.9 μm SiC device layer. (Center) 5.2 μm SiC device layer. (Right) 6.5 μm SiC device layer. The bending down of different length beams, shown in the top images for each of the device layer thicknesses with red lines, occurs at near the same location for all of the thicknesses shown. There is slightly less bending of the thicker beams.

The strain gradients for a cantilever beam can be calculated using the following equation:

$$\delta = \frac{2\gamma}{L^2} \tag{4.12}$$

78

Where δ is the strain gradient, γ is the cantilever tip deflection, and L is the cantilever beam length [102]. The strain gradient of these three film thicknesses, shown in Figure 4.23, were calculated using the deflection of the 500 μm long released cantilevers shown in the top images from Figure 4.22.
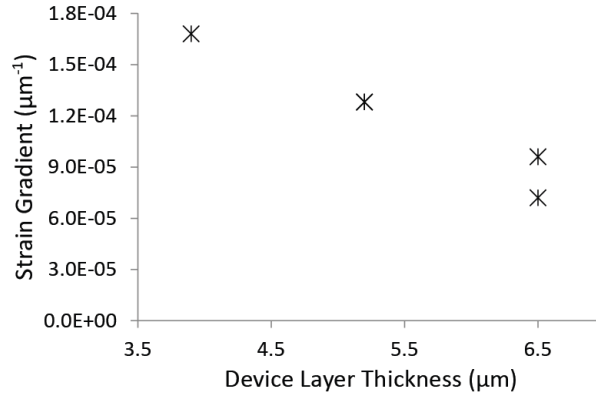
Figure 4.23. The strain gradients for 3.9 μm, 5.2 μm, and 6.5 μm thick device layers are plotted.

Side Wall Fabrication

The thicker SiC process increased the difficulty of the side wall fabrication due to the increased sensor topology. As the side walls increase in height, it becomes more challenging to coat the structures in photoresist. Applying thicker photoresist layers leads to underdeveloped resist. Once this issue was addressed by tailoring exposure and development times, the difficulty with maintaining a uniform SiO_2 sidewall at the full height of the SiC device layer was addressed. The process used in the fabrication the initial sensors was modified in an attempt to achieve acceptable side wall profiles. Eight fabrication techniques were attempted for the fabrication of the silicon dioxide side wall as shown schematically in Figure 4.24.

79
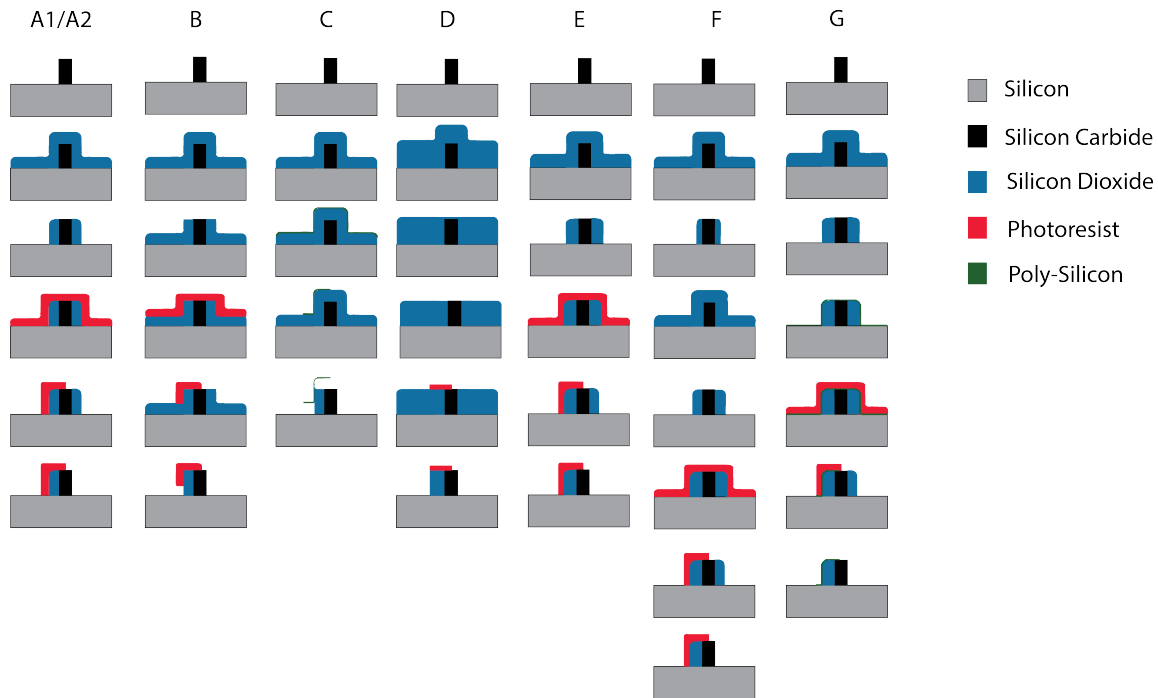
Figure 4.24. Eight process flows to describe the eight side wall fabrication techniques employed. A)RIE was used to etch the oxide on top of the Si and SiC structures while leaving the side walls. PR was patterned and the SiO_2 is etched. Both liquid HF (A1) and RIE etching (A2) were used in this fabrication iteration. B) CMP was used to remove oxide from the top of the SiC structures. PR was patterned and the oxide was etched using HF. C) A 100 nm poly-Si layer was deposited and patterned to mask the desired side wall area. HF vapor was used to etch the poly-Si. D) A thick layer of SiO_2 is deposited. The oxide is CMPed flat and etched back to the SiC layer using HF vapor. PR is patterned and the oxide side wall is etched. E) A thicker ˜3-4 μm oxide is deposited. This allows for some stray side wall etching during RIE. Once the top and bottom are etched down, the side wall is masked. F) Multiple SiO_2 deposition and etch steps are used to build up a side wall while removing the top and bottom oxide. Once the wall layer is built up, the side wall is masked and the etch process takes place. G) The final fabrication technique combines methods C and F. A thick layer of oxide is deposited and etched back so only the side walls remain. Then a thin poly-Si layer is deposited and etched as a hard mask before RIE of the unwanted oxide side walls.

Seven of these eight fabrication techniques had flaws that led to failures in the sidewall definition. Fabrication methods A1/A2 were directly based off of the thin SiC device layer process. However, due to less conformal photoresist coverage in the thicker device layers, neither buffered HF, used for method A1, or RIE with chlorine chemistry, for method A2, were able to remove the unwanted oxide while the desired oxide walls were unetched. Both of these methods resulted in the partial removal of the desired wall profile. There was also non-uniformity in the over-etching of the desired walls. One end of the wall would have

minimal over-etching, while the other end was significantly over-etched. The over-etching and its non-uniformity can be seen in Figure 4.25.
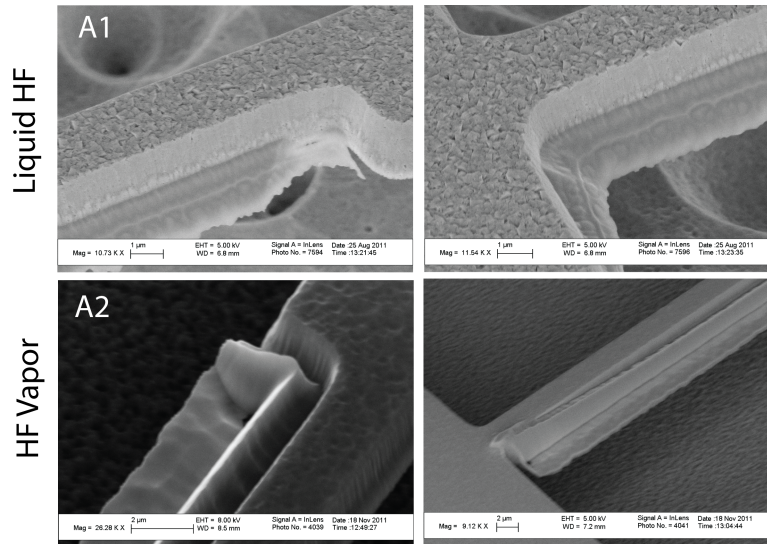
Figure 4.25. Side wall fabrication process A. (Top) The liquid HF over etched the oxide side wall. (Bottom) The initial RIE selectively over etched the oxide next to the SiC device layer. The PR protected both the side wall and the under etched SiO_2 that was masked next to the side wall.

Fabrication method B required the use of chemical mechanical polishing (CMP). In this method, a 2 μm SiO_2 layer was deposited conformally on the etched SiC device layer. The top of the SiO_2 layer was attempted to be planarized using the CMP. The CMP uses a mixture of DI water, KOH, and 200 nm diameter SiO_2 particles. The hydroxyl ions from the KOH attack the SiO_2 causing it to dissolve while the SiO_2 abrasive particles physically polish the wafer surface. The main reason that the desired results were not achieved using this method was the rate of chemical attack of the oxide layer versus the physical polishing effect. The chemical oxide etching reduced the side wall oxide profile while etching down the intended top oxide surface. By the time the top oxide layer was removed, the side wall oxide was almost entirely etched due to the chemical attack. This left minimal oxide side wall for later patterning steps. Figure 4.26 shows the before and after top views of the bimorph section of the sensors, which shows that the oxide side walls are no longer present post CMP.
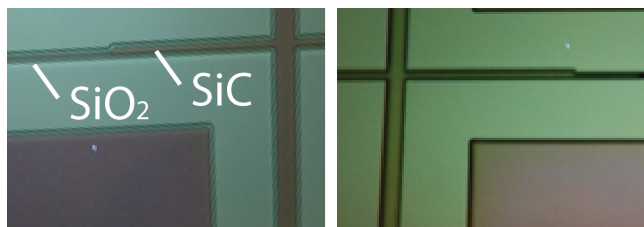
Figure 4.26. Process B was unsuccessful as the chemical attack on the oxide was enough to etch the sidewall oxide during the polishing process. The images above show (right) the SiC with the oxide sidewall before CMP and (left) the post CMP side wall where no oxide remains.

Fabrication method C used a poly-Si hard mask with HF vapor rather than the buffered HF used in process A1 for etching. This method was attempting to improve the oxide side wall coverage and prevent the HF infiltration, which led to the non-uniform etching seen in method A. However, it was found that even with very low HF etch rates, utilizing higher flow rates of purging gases, the HF vapor preferentially etched along the poly-Si/SiO$_2$ interface. This resulted in the lift-off of the poly-Si hard mask allowing the HF to attack the previously protected side wall. The lift off of the poly-Si hard mask can be seen in Figure 4.27.
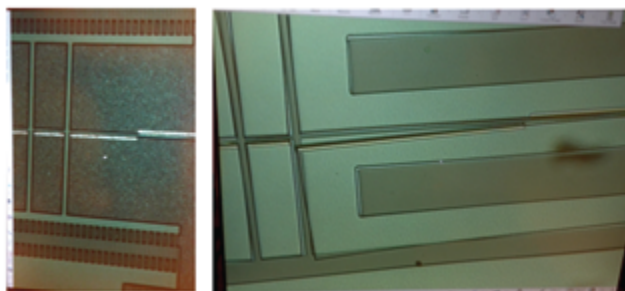
Figure 4.27. In fabrication method C the poly-Si layer had very good side wall coverage (left); however, the HF vapor selectively etched only the poly-Si/SiO$_2$ interface. It etched the whole SiO$_2$ wall and lifted off the poly-Si (right).

Fabrication method D used the CMP technique like in method B; however, in this attempt, the oxide layer that was deposited was thicker than the thickness of the SiC device layer. This reduced the chemical attack on the oxide side walls and did not require an exact etch stop time like that in method B when CMP had to stop when the top oxide was etched down to the SiC layer. The oxide needed to be CMPed until the oxide layer was flat and uniform above the SiC devices. However, this large amount of CMP processing led to the delamination of the SiC layers as shown in Figure 4.28. The individual layers were not seen in SEM images post deposition and were only noticeable in this fabrication attempt.
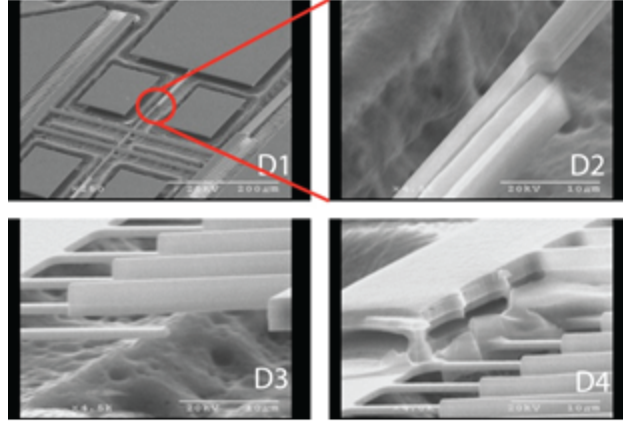
Figure 4.28. Fabrication method D using CMP failed because the CMP process caused the delamination of the SiC layers. However, there is a good side wall oxide profile as shown in D2. Delamination is seen most severely on the smaller areas of SiC. The inside comb fingers, those not attached directly to anchors, show the most layer delamination.

Fabrication method E is similar to method A2 with the dry RIE etching; however, a thicker oxide layer was deposited before the etching process. SEM images were taken mid-process to show the side wall profile as the blanket, unmasked, oxide layer is etched. These profiles, shown in Figure 4.29, show that the RIE etching process leaves a sloping sidewall profile. While this image shows a 6 μm thick layer of oxide, the sidewalls fabricated with this method were 3 μm thick. The top view of the sidewall post blanket etch, Figure 4.30, shows that there is more oxide than required by the design. The oxide is thicker than the Si test device structures. Two blanket etch times, 9 and 10 minutes, and four patterned etch times, 3, 6, 9, and 12 minutes, were tested using this method. Only the 9 and 12 minute etch times are shown. These test structures had good PR coverage on the thick test device structures; however, the PR layer is very thin on top of the devices. This can be seen in Figure 4.31. The thin PR on top and difficult alignment resulted in the etching of the oxide in contact with the device side wall while protecting oxide at a slight distance from the device feature. Trenches were etched between the two materials.

10 Minute Etch   15 Minute Etch   20 Minute Etch
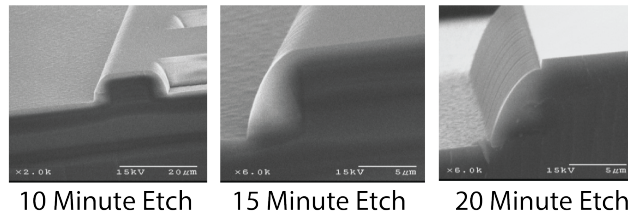
Figure 4.29. 6 μm of silicon dioxide was deposited on 9 μm Si devices. The oxide layer was dry etched using C_4F_8 for times of 10, 15, and 20 minutes.
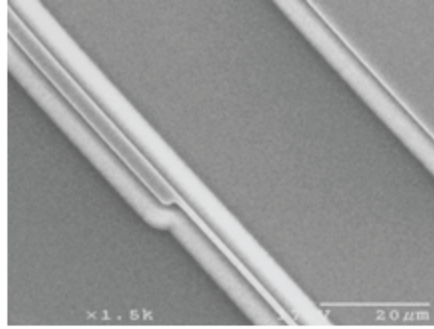
Figure 4.30. The top view of the 20 minute etched sample shows the width of the oxide side wall relative to the Si structure.
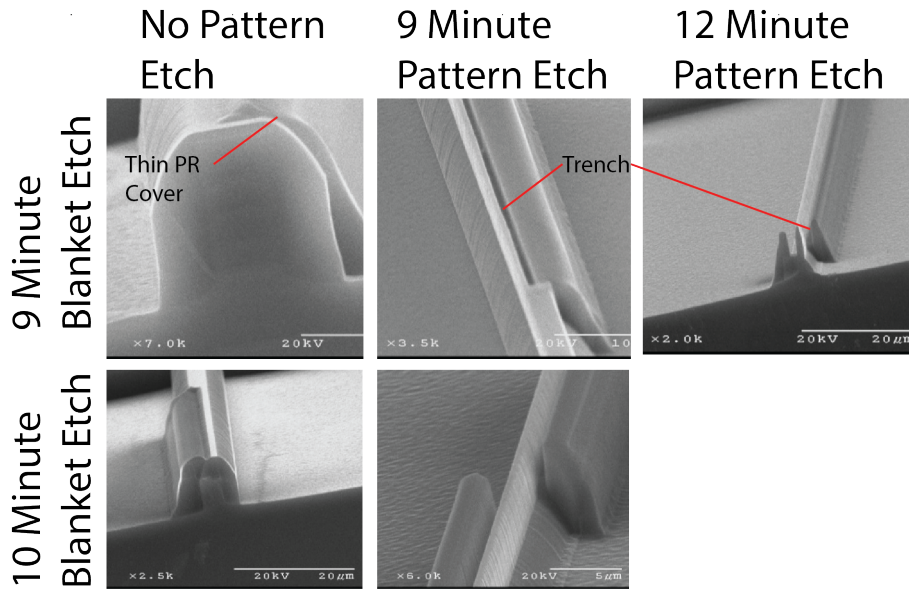
Figure 4.31. Silicon structures were coated with one 3 μm SiO_2 layer after either a 9 or 10 minute blanket etch of the SiO_2. The masked oxide was then etched for 0, 9, or 12 minutes. In the unpatterned, 9 minute blanket etched SEM image (top left) we can see that there is full photoresist on the side wall and top of the oxide that covers the SiC device layer; however this photoresist layer is very thin around the corner of the oxide. This thin layer leads to poor oxide protection during the etching process allowing a trench to form between the device layer and the oxide sidewall. This can be seen in the 9 minute and 12 minute patterning etches (top center and top right). Similar results are seen for the 10 minute blanket etch; however, the effect is amplified as the photoresist covering is less uniform. The 10 minute blanket etch exposed the SiC device layer that was fully covered with oxide in the 9 minute blanket etch samples.

Similar PR coverage and alignment issues were seen in method F, Figure 4.32. This

process had two depositions of 3μm of SiOμm. Blanket etches were performed between the depositions. Total blanket etch times of 17 and 19 minutes were tested. Patterned etch times of 3, 6, 9, and 12 minutes were tested. Only the unetched and 9 minute etch tests are shown to show the same misalignment seen in method E.
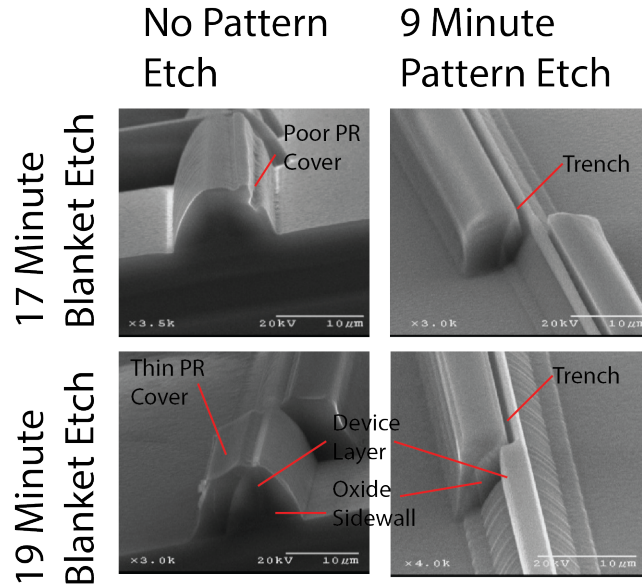
Figure 4.32. Silicon structures were coated with two 3 μm SiO$_2$ layers. The first layer was blanket etched for either 9 or 10 before the second deposition, which was blanket etched for either 8 or 9 minutes. This was followed by 9 minute etches of the patterned sidewalls. The second oxide deposition and etch steps generated a more sloped sidewall than was seen with the single oxide deposition. However, this sloped side wall did not improve the top and corner photoresist coatings. The oxide etch step was able to etch a trench between the oxide side wall and the device layer.

The final fabrication method, method G, incorporated the poly-Si mask used in fabrication method C and the RIE used in methods A2, E, and F. In this method a 3 μm SiO$_2$ layer was deposited on the etched SiC device layer. This layer was RIE etched to remove the oxide on the top of the SiC structures and the exposed Si between SiC features. Next, a thin (100 nm) poly-Si layer was deposited and patterned to define the SiO$_2$ side walls. RIE was utilized again to remove the undesired oxide. The uniform thin poly-Si layer prevented the trench formations seen in methods E and F. The initial result showed that the thin poly-Si mask was not fully etched when released with the XeF$_2$. This residual film was due to the low thermal mass on the released structure, which limited the ability to catalyze the XeF$_2$ reaction. Increasing the etch step time increases the XeF$_2$ etch temperature and results in the etching of the poly-Si mask during the release step. The released devices with SiO$_2$ sidewalls are shown in Figure 4.33.
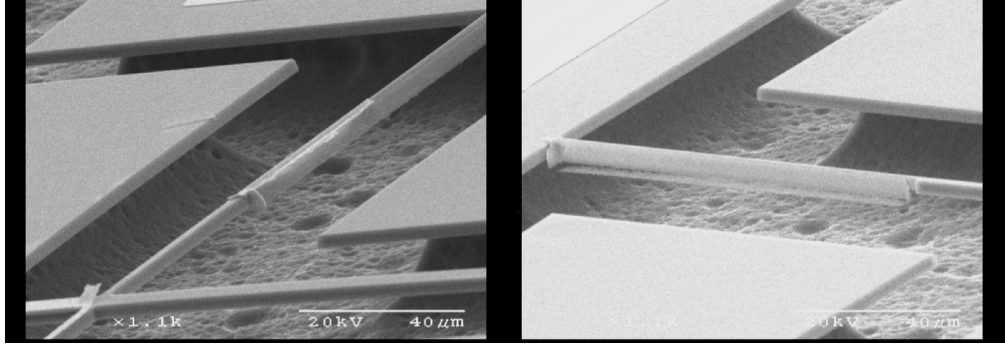
Figure 4.33. SiC devices were released using XeFl2. However, the poly-Si hard mask used in the side wall etching mask was not fully etched. (Left) Poly-Si is seen remaining only partially on the side wall. The SiO_2 side wall can be seen and is slightly lower than the SiC beam. (Right) A thin layer of SiO_2 remains on the bottom of the side wall, suspended off to the side of the beam.

Contact Resistance

The metalization of the devices for bond pads is needed for signal acquisition. Understanding the nature of the contact, Ohmic versus Schottky, when connecting metals to semiconductor materials is important to fully understand device performance. If there is a Schottky contact, there is an electrical barrier between the metal and semi-conductor that makes it difficult for holes and electrons to move between the two materials. This leads to better conduction in one direction, either semi-conductor to metal or metal to semi-conductor. Ohmic contacts have the same conduction in both directions, thus, they obey Ohm's Law. There has been some work done in the fabrication of Ohmic contacts for platinum with both poly-SiC and single crystal SiC [103], [104], [105]. Another common material used for metalization on SiC is nickel [106], [107], [108], [109]. Initially, sensors were metalized using platinum for high temperature stability. A 100 nm Pt layer was sputtered using a 30nm Cr adhesion layer in a lift-off process. Once deposited, IV curves were generated between two metal pads with a 5 μm gap spacing. As shown in the literature [104], [110] "as-deposited" Pt on n-type poly-SiC displayed Schottky behavior, which can be seen in the IV curves shown in Figure 4.34.
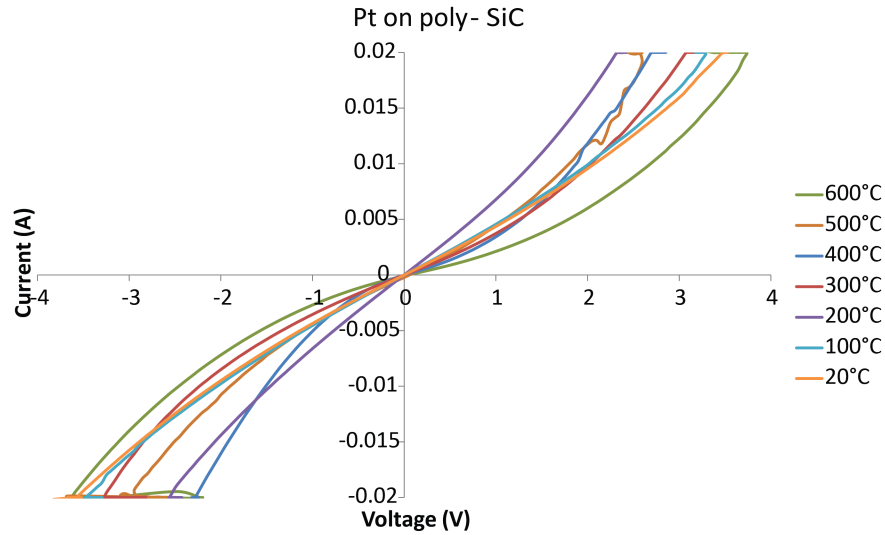
Figure 4.34. IV curves from 20 °C to 600 °C using a high temperature probe station.

Due to this Schottky contact, Ni was attempted for achieving an Ohmic contact. A 150 nm layer of Ni was sputtered with no adhesion layer onto the n-type poly-SiC device layer. The same 5 μm gap spacing was used to measure IV curves from 20 °C to 600 °C using a high temperature probe station. The Ni was tested in an "as-deposited" form and after two 30 second anneals in 950 °C argon. Ohmic contact was seen for both of these samples, Figures 4.35 and 4.36. The resistance change with temperature was shown to be less with the annealed Ni than the as deposited Ni, Figure 4.37. The annealing processes lead to the formation of nickel silicides. This effect can be seen in SEM images of the bond pads pre- and post- anneal in Figure 4.38.
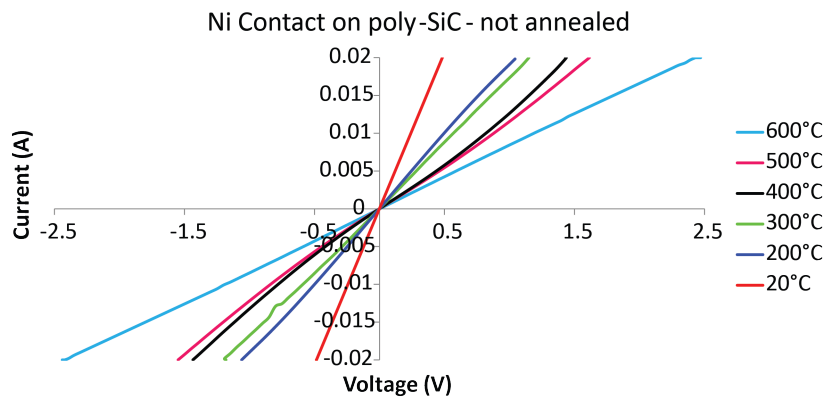
Figure 4.35. IV curves from 20 °C to 600 °C using a high temperature probe station of "as-deposited" Ni on n-type poly-SiC.
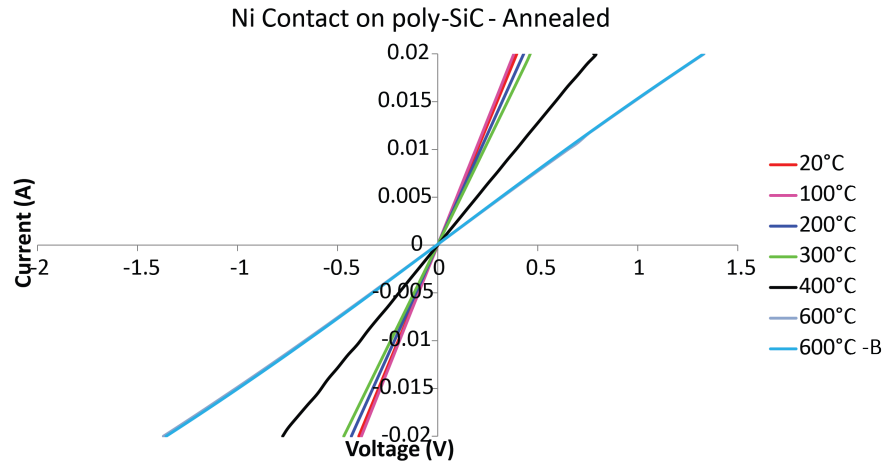
Figure 4.36. IV curves from 20 °C to 600 °C using a high temperature probe station of annealed Ni on n-type poly-SiC.
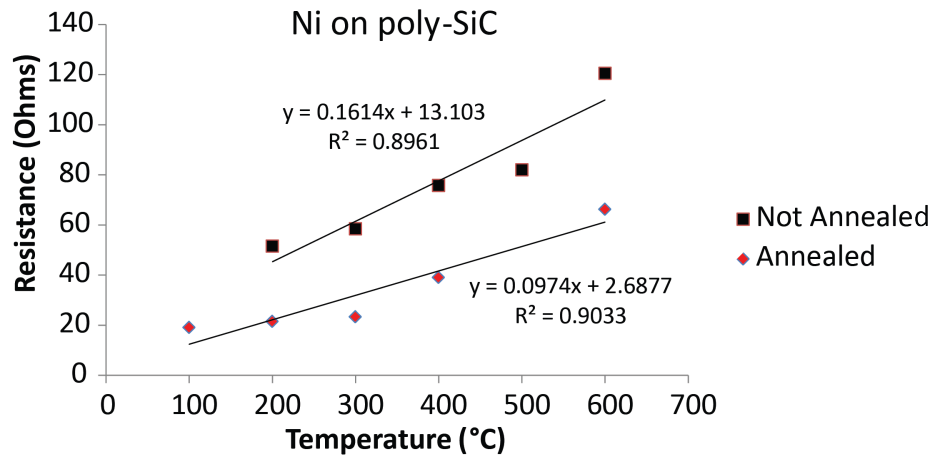
Figure 4.37. Resistance between Ni pads on n-type poly-SiC versus temperature.
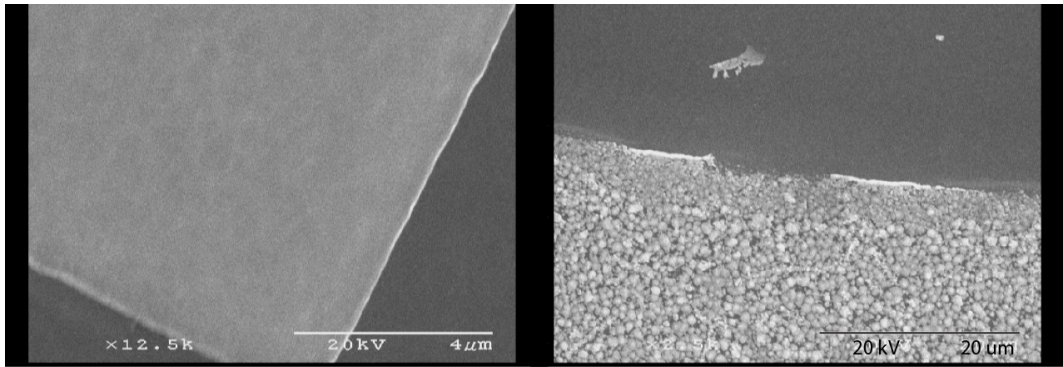
Figure 4.38. (Left) As deposited Ni on SiC device layer. (Right) Bond pad annealed at 950 °C for two 30 second cycles in an Ar environment.

4.3   In-Plane MEMS Temperature Sensor Testing

Thin SiC Device Layer

The first set of sensors that were tested were from the thin SiC device layer fabrication run. These sensors were initially tested using a high temperature, 5x5 mm, 50 W, ceramic heater on a probe station stage. When no in-plane motion could be detected, a voltage was applied across the fixed-fixed beam to Joule heat the structure. Due to the thin SiC layer, where the width of the bimorph was greater than that of the thickness, rather than buckling in plane due to the bimorph effect, the sensors buckled out-of-plane due to the small moment of area in the out of plane direction as shown in Figure 4.39. While the differences in the moments of area of in the in-plane versus out-of-plane directions was considered in the design, the bimorph effect was expected to overcome this geometric flaw to reduce fabrication complexity. However, the residual stress in the structures resulted in pre-bending the bimorph in the out-of-plane direction. This pre-bending made out-of-plane motion more favorable than the expected in-plane actuation.
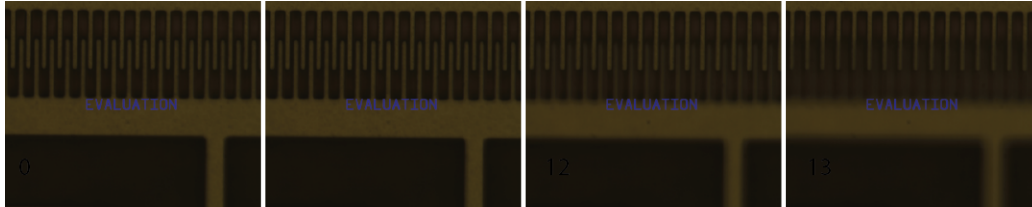
Figure 4.39. The thin SiC used for this fabrication iteration resulted in out of plane buckling. The figures left to right show DC bias values of 0, 10, 12, and 13 volts applied to heat the bimorph structure. The released structure (bottom combs) clearly shows out-of-plane motion by losing focus when temperature is increased.

Thick SiC Device Layer

The thicker devices stayed in plane during actuation; however, due to the SiC device layer strain gradient, there were too few fingers interdigitated to make capacitive measurements. Optical measurements were made by using the high temperature ceramic heater under a microscope, and can correspond to capacitive values that would be sensed with a reduced film strain gradient. Initial ANSYS simulations indicated that the in-plane sensing bimorph motion would initiate at room temperature with an applied thermal load. However, this was not observed. Measured data shows that the bimorph structure does not move until around 300 °C, see Figure 4.40 and Figure 4.41. Once the ANSYS simulations were revised to include the in-plane residual stresses of the SiC film, the theoretical temperature versus displacement curve matched the collected data within R^2 values of up to 0.959. The sensing range for these devices is higher than the 90 °C to 400 °C desired range. The 450 μm bimorph beam length devices have a 0.96 R^2 value showing linearity between 210 °C to 685 °C. The 500 μm bimporh beam length devices have a 0.95 R^2 value for their linearity between 380 °C to 660 °C.
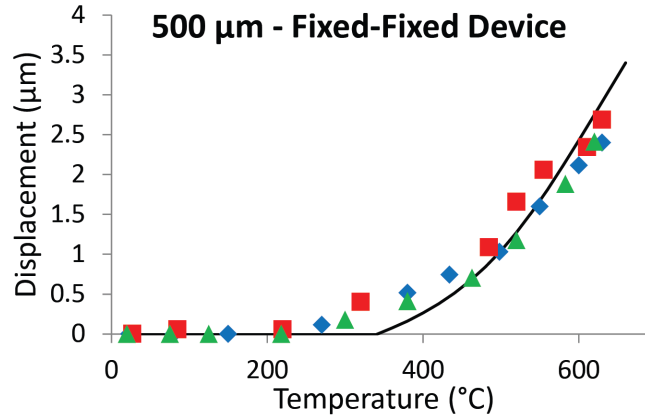
Figure 4.40. Optically measured comb tooth displacement of 500 μm fixed-fixed device up to 630 °C. Two heating cycles (red and green), one cooling cycle (blue) and the modified ANSYS curve (black) are shown.
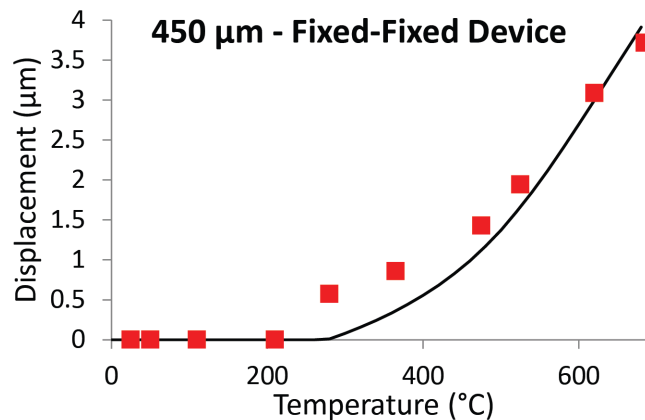
Figure 4.41. Optically measured comb tooth displacement of 450 μm fixed-fixed device up to 685 °C. The modified ANSYS code is shown in black.

Tests of the decoupled sensor designs were also conducted. Due to the length of the comb finger sections and the negative strain gradient, once released, the ends of the comb drives were touching down on the substrate surface. This additional resistance to mechanical motion resulted in minimal actuation. The 1000 μm long crab leg device was tested up to 610 °C and the motion was recorded optically. No motion was detected until the sensor reached around 400 °C, higher than that seen for the fixed-fixed devices. The motion was also significantly less than expected with 1.2 μm displacement at 610 °C. The plot in Figure 4.42 displays this reduced device motion. Similar results were observed with the folded flexure anchored devices. These devices were only tested up to 515 °C because of their location on the fabricated die relative to the ceramic heater. At 515 °C the comb teeth had only displaced 1.2 μm. This is the same displacement as seen with the 1000 μm crab leg

91

device. These motions are likely the same due to the fact that the longer crab leg devices had a larger area in contact with the substrate. This restricted the motion of these devices more than that of the shorter folded flexure designs. Modified ANSYS models were not made to model the contact between the strained comb fingers in contact with the substrate as the devices must be redesigned with shorter comb finger beam lengths.
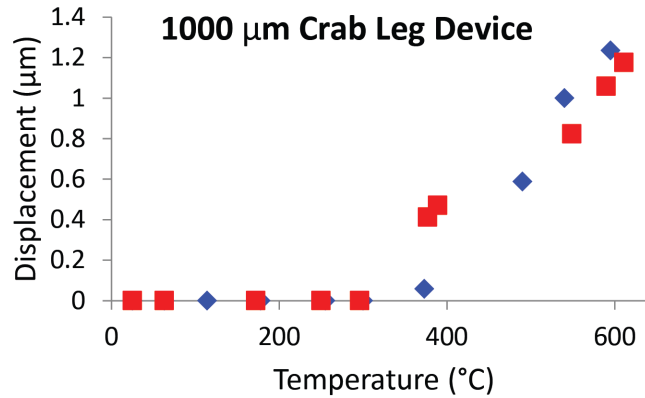
Figure 4.42. Optically measured comb tooth displacement of 1000 μm crab leg device up to 610 °C. Both heating (red) and cooling (blue) cycles are shown.
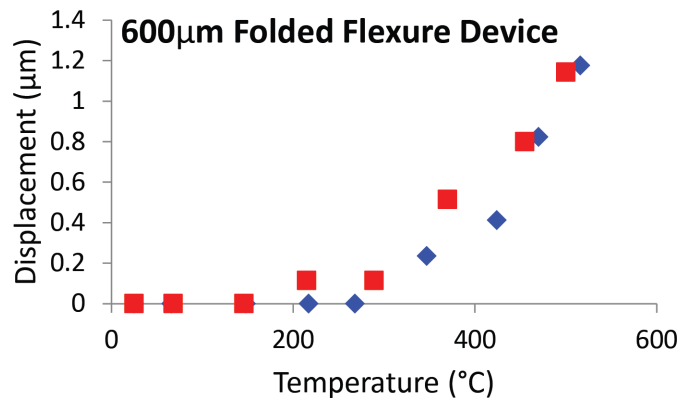
Figure 4.43. Optically measured comb tooth displacement of 600 μm folded flexure device up to 515 °C. Both heating (red) and cooling (blue) cycles are shown.

Lowering Sensing Temperature Range

While these temperature sensors could operate in the higher geothermal monitoring temperature range, 300 °C to 500 °C, the U.S. geothermal wells require a lower temperature range

90 °C to 400 °C. To reduce the temperatures in which the in-plane temperature sensors can operate, the SiC film strain should be reduced. However, the bimorph structure can also be differentially heating using Joule heating. This allows for sensing at lower temperatures by pre-heating the bimorph beam. Tests were conducted by applying an 11 volt DC offset to the temperature sensors, see Figure 4.44. This reduced the initial sensing temperature to 25 °C, see Figure 4.45. Due to the differential heating of the substrate and device, there is a larger influence from the buckling effect at lower temperatures, and larger deflections than those seen with ambient only heating. Multiple offset voltages were used to reduce the sensing range. Both 10 and 11 volt offsets are shown in Figure 4.46.
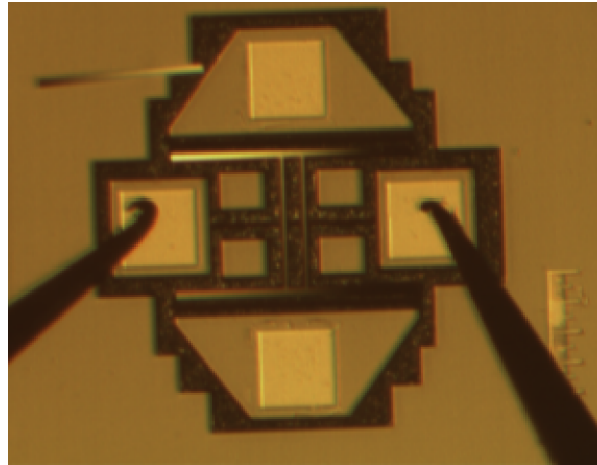
Figure 4.44. To reduce sensing actuation temperature, the bimorph structure was differentially heated using a DC offset applied on a probe station.
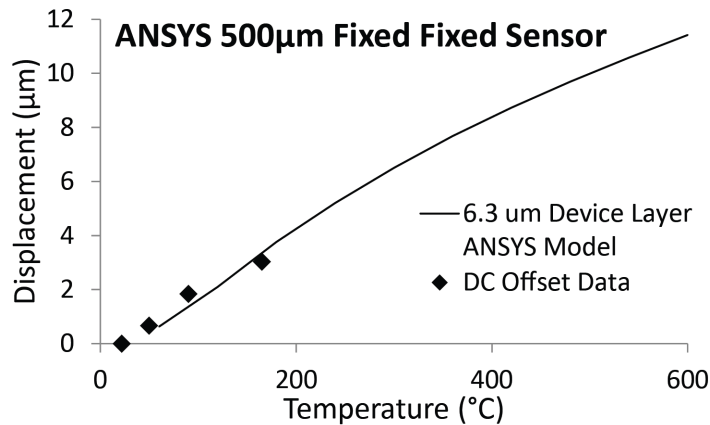
Figure 4.45. An 11 volt DC offset was applied to the 500 μm long, 6.3 μm thick, device to lower the minimum sensing temperature to 25 °C. This is shown with the ANSYS simulation modeling the lower temperature range.

93
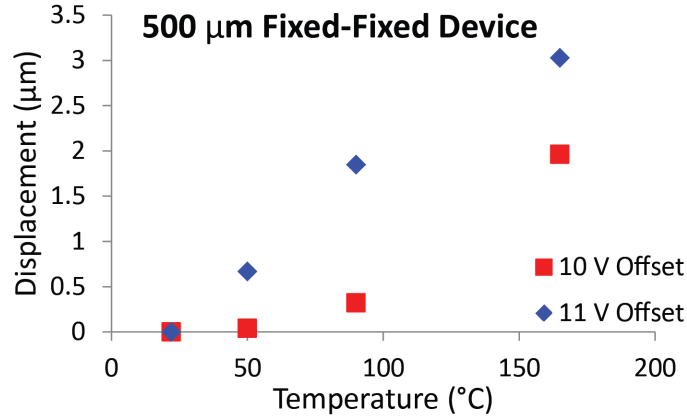
Figure 4.46. Both 11 volt and 10 volt DC offsets are applied across the fixed-fixed structure to reduce the sensing range. 11 volts reduces the sensing temperature to 50 °C while 10 volts reduces the sensing temperature to 90 °C.

4.4 In-Plane Temperature Sensor Summary

In-plane bimorph temperature sensors were designed and optimized for linearity for the temperature range of 150 °C to 400 °C. Designs for the in-plane temperature sensors are still based on the bimorph technology used for the out-of-plane sensors; however, the dissimilar materials are side-by-side rather than top and bottom. These designs are evaluated using basic analytical models and more detailed FEA models in ANSYS. Both thin, 1.3 μm, and thick, 3.6 μm - 6.5 μm, device layer sensors were fabricated. The development of a novel sidewall deposition process was developed to allow for in-plane bimorph actuation. The strain gradient of the SiC device layer was reduced by depositing more layers to make a thicker overall device layer. The sensors were tested up to 685 °C and displacements of up to 4 μm were measured optically. Due to residual stress in the SiC film layer, the operational sensor temperature range was above the expected values. Temperature sensing began at a minimum temperature of 300 °C. DC offset voltages were applied to the fixed-fixed anchor structures to differentially heat the bimorph section. This effectively reduced the temperature sensing range to that seen in U.S. geothermal wells. The modified ANSYS code matched the experimental data indicating that if the film stress was further reduced, the originally modeled linear performance would be achieved. The SiC strain gradient limited potential electrical tests that could be used to evaluate these sensors. Based on the optical test data, assuming a 10 Hz bandwidth and using the noise floor from the Irvine Sensors MS3110 of 4 af/rtHz, a theoretical sensing resolution of 0.225 °C is projected. A R^2 values for linearity of up 0.96 are achieved between 210 °C to 685 °C. This linearity is expected to improve with the reduction of residual SiC device layer film stress.

Chapter 5

Conclusions and Future Work

Geothermal energy is a valuable alternative energy source for producing stable, base load electric power. Harsh environment sensing technologies including wireless MEMS will help to improve geothermal well efficiency as well as provide data that can be used to improve subsurface maps used in geothermal well exploration. This dissertation described the testing of sensor materials and the development of temperature sensors for down hole geothermal environments. The main outcomes of this work relating to both materials exposure testing and temperature sensor design are: 1) the determination of two potential materials, single crystal and micro-crystalline diamond, that are for encapsulation within the geothermal environment, 2) the elimination of four potential materials, AlN, Si, vitreous carbon, and amorphous SiC, for the encapsulation of MEMS in the geothermal environment, 3) the necessity for further testing of two potential encapsulation materials, SiC and sapphire, 4) The development of an out-of-plane harsh environment compatible temperature sensor, and 5) the development of a novel in-plane temperature sensor design that was tested at temperatures up to 685 °C.

In this work five different materials were exposed to water environments in liquid, vapor, critical point, and supercritical phases. The silicon control material demonstrated the need for specialized harsh environment materials in the down hole environment by experiencing mass losses of up to 80% from 20 hours of exposure to supercritical water. Sapphire was the most promising harsh environment compatible material from the water testing with an asymptotic surface roughening profile from 1 to 100 hours of exposure testing. XPS analysis revealed the same amount of both sample degradation and Ni diffusion for 50 and 100 hour exposed samples. The tested SiC substrate materials oxidized more readily than the sapphire and allowed for deeper Ni diffusion.

Geothermal brine testing was conducted to simulate the effects of the salt within the down hole environment on the harsh environment sensor materials. Tests of 100, 200, and 300 hours in sub-critical liquid brine were conducted within welded gold reaction capsules. Of the exposed materials, single crystal diamond and micro-crystalline diamond had the best

survivability characteristics based on minimal oxidation and surface roughening. Micro-crystalline diamond was designated the preferred material for encapsulation for the geothermal environment as it can be grown in MEMS compatible processes.

A review of the state of the art temperature sensing technologies was given. Based on this review, the need for a harsh environment compatible, passive, capacitive temperature sensor was determined. An initial harsh environment prototype was designed after an existing silicon-based temperature sensor using the more common out-of-plane capacitive sensing mode. This sensor was fabricated and tested up to 350 °C to show that an out-of-plane sensing solution was possible for this harsh environment.

Finally, this dissertation details the design, optimization, fabrication, and testing of a novel in-plane temperature sensor. The in-plane sensing mode was used to improve signal linearity without increasing system complexity. The development of the fabrication process to make a side-by-side material bimorph is described in detail. These sensors were tested up to 685 °C. Optical measurements verify ANSYS models for the devices. Based on the ANSYS simulation verifications, the in-plane sensors are projected to have a more linear capacitance versus temperature response to the out-of-plane temperature sensors.

Future work for this project includes the reduction of residual film stress to reduce the passive sensing temperature range for the in-plane temperature sensors. The strain gradient must also be further reduced to allow for electrical signal transduction. Different annealing processes can be developed to reduce these two factors. Changing of the SiC doping levels may also play a role in the reduction of residual stress and strain gradients in the film. These changes will allow for the capacitive reading of the in-plane SiC devices.

Future work also includes longer duration exposure testing of SiC and sapphire materials to determine if they can be used for encapsulation materials. These two materials should be retested in the low concentration pH for up to 300 hours. These retests will provide the data needed to show if the oxidation and degradation behaviors of these materials is self limiting. Long term testing of the micro-crystalline diamond in different geothermal well conditions will give a more complete picture of the materials survivability in a variety of well chemistries. In addition, super critical water testing should be conducted to ensure that there is no oxidation or significant surface graphitization of the grown films in the higher temperature and pressure environment. Chemistries for specific wells that would be used for sensor deployment should be used for materials testing conditions prior to sensor integration attempts.

Other areas for future work include the designing of a fabrication process flow to incorporate the micro-crystalline diamond encapsulation layer into the temperature sensor fabrication process. Care must be taken not to exceed the sensors thermal budget. This may involve making a cap with the micro-crystalline diamond and bonding that cap over the chip, or the direct growth of the diamond on the devices.

Once encapsulated, the sensors must be operationally tested in a simulated geothermal environment in both isolated conditions and as wired devices. The initial designs for test apparatuses are shown in Appendix C. Pre-wired tests would start with the exposure of sealed cavities and diaphragms. These tests would be conducted to determine the survivability of

the bonding between the sensor materials. Bonded cavities and sealed volumes on chips would be sealed in to gold capsules to long term exposure. Pre- and post sample weights could be used to determine leaks in the capsules. A visual inspection of the cavity surface can be used to determine and material fracture or surface degradation. Cavity cross sections can be made to inspect the internal surfaces. Internal damage could be due to leaking or stresses from CTE mismatches. Once sealed capsules are tested, operational sensors can be tested pre- and post geothermal environmental exposure. To begin this testing, pre-exposure sensor characterization should be done to determine measurement ranges and accuracies. Once sensor performance baselines are determined, the sensor would then be exposed to the simulated geothermal environment. These tests could be conducted in welded gold capsules to expose materials to different chemical environments. Once long term exposure tests are completed, the sensors would be post-exposure characterized to compare the measure parameters to the pre-exposure tests.

Once the simulated tests have been conducted, field tests will be required for a final validation of the sensors and their encapsulation. Initially, deployed sensors may be in a wired configuration. SiC circuit integration will be required to implement wireless sensing solutions.

Bibliography

[1] Massachusetts Institute of Technology. The future of geothermal energy: Impact of enhanced geothermal systems (EGS) on the united states in the 21st century. 2006.

[2] D. Chandrasekharam and J. Bundschuh. Low-enthalpy geothermal resources for power generation. 2008.

[3] J. Finger and D. Blankenship. Handbook of best practices for geothermal drilling. *Sandia Reports*, 2010.

[4] S. Wodin-Schwartz, M. W. Chan, K.R. Mansukhani, A. P. Pisano, and D.G. Senesky. MEMS sensors for down-hole monitoring of geothermal energy systems. *ASME 2011 5th International Conference on Energy Sustainability and 9th Fuel Cell Science, Engineering and Technology Conference*, 2011.

[5] Wendy M. Calvin, Mark Coolbaugh, Chris Kratt, and R. Greg Vaughan. Application of remote sensing technology to geothermal exploration. *Great Basin Center for Geothermal Energy (GBCGE) and the Department of Geological Sciences*, 2005.

[6] L. Candela. Advances in subsurface pollution of porous media: Indicators, processes and modeling. *CRC Press*, 2008.

[7] Kuster Company. K10 geothermal pts sro instrument operation and service manual. 2010.

[8] DOE National Renewable Energy. Reservoir engineering. *Office of Geothermal Technologies*, 1998.

[9] M. Jaaskelainen. Distributed temperature sensing (DTS) in geothermal energy applications. *Sensors Magazine*, 2009.

[10] MICA Controls LTD. Qorex: Fiber optic monitoring.

[11] C.E. Clark, C.B. Harto, J.L. Sullivan, and M.Q. Wang. Water use in the development and operation of geothermal power plants. *US DOE EERE Geothermal Technologies Program*, 2010.

[12] Geothermal Technologies Office. What is an enhanced geothermal system (EGS)? *U.S. Department of Energy*, DOE/EE-0785, 2012.

[13] MINCO. Technical specifications RTDs. 2006.

[14] Omega. Thermocouples - an introduction. *OMEGA Engineering Technical Reference.*

[15] Omega. High temperature thermistors.

[16] D.R. Myers, K.B. Cheng, B. Jamshidi, R.G. Azevado, D.G. Senesky, M. Mehregany, and A. P. Pisano. Silicon carbide resonant tuning fork for microsensing applications in high-temperature and high g-shock environments. *J. Micro/Nanolith*, 8(2), 2009.

[17] E. Barringer, Z. Faiztompkins, and H. Feinroth. Corrosion of CVD silicon carbide in 500c supercritical water. *Journal of American Ceramics Society*, 90:315–318, 2006.

[18] H. Hirayama, T. Kawakubo, A. Goto, and T. Kaneko. Corrosion behavior of silicon carbide in 290c water. *J. Am. Ceram. Soc*, 1989.

[19] T. Kraft and K.G. Nickel. Hydrothermal degradation of chemical vapor deposited SiC fibres. *Journal Of Materials Science*, 1998.

[20] W. Kim, H.S. Hwang, and J.Y. Park. Corrosion behavior of reaction-bonded silicon carbide ceramics in high-temperature water. *J. Material Science Letters*, 2002.

[21] W. Kim, H.S. Hwang, J.Y. Park, and W. Ryu. Corrosion behavior of sintered and chemically vapor deposited silicon carbide ceramics in water at 360C. *J. Material Science Letters*, 2003.

[22] K.-N. Lee, D.-S. Lee, S.-W. Jung, Y.-H. Jang, Y.-K. Kim, and W.-K. Seong. A high-temperature MEMS heater using suspended silicon structures. *J. Micromech. Microeng*, 19, 2009.

[23] B.E. Deal and A.S. Grove. General relationship for the thermal oxidation of silicon. *Journal of Applied Physics*, 36(12), 1965.

[24] Kirt R. Williams and R.S. Muller. Etch rates for micromachining processing. *Journal of Microelectromechanical Systems*, 5(4), 1996.

[25] T. Richard, J. Poirier, C. Reverte, C. Aymonier, A. Loppinet-Serani, G. Iskender, E-B. Pablo, and F. Marias. Corrosion of ceramics for vinasse gasification in supercritical water. *Journal of the European Ceramics Society*, 32:2219–2233, 2012.

[26] Y. Song, S. Dhar, L.C. Feldman, G. Chung, and J.R. Williams. Modified deal grove model for thermal oxidation of silicon carbide. *Journal of Applied Physics*, 95(9), 2004.

[27] A. Koh, A. Kesle, C. Wright, S.P. Wilks, P.A. Mawby, and W.R. Bowen. Comparative surface studies on wet and dry sacrificial thermal oxidation of silicon carbide. *Applied Surface Science*, 174:210–216, 2001.

[28] C.H. Henager Jr., A.L. Schemer-Kohrn, and K.G. Pitman. Pitting corrosion in CVD SiC at 300C in deoxygenated high-purity water. *Journal of Nuclear Materials*, 378(1):9–16, 2008.

[29] L. Tan, T.R. Allen, and E. Barringer. Effect of microstructure on corrosion of CVD-SiC exposed to supercritical water. *Journal of Nuclear Materials*, 394:95–101, 2009.

[30] M. Yoshimura, J. I. Kase, and S. Somiya. Oxidation of SiC powder by high-temperature, high-pressure H2O. *J.Mater Res.*, 1:100, 1986.

[31] Jessica Eid, I.G. Galben, and S. Saddow. 3C-SiC growth on Si substrates via CVD: An introduction. *Physics of Advanced Materials Winter School*, 2008.

[32] Y. Gogotsi G. Yushin, A. Nikitin. 8 carbide-derived carbon. *Nanomaterials Handbook Department of Materials Science and Engineering Drexel University*, 2006.

[33] Liudi Jiang, N O V Plank, M A Blauw, Rebecca Cheung, and E van der Drift. Dry etching of SiC in inductively coupled Cl2/Ar plasma. *J. Phys. D: Appl. Phys*, 37, 2004.

[34] W.-S. Pan and A.J. Steckl. Reactive ion etching of SiC thin films by mixtures of fluorinated gases and oxygen. *J. Electrochem. Soc.*, 137(1), 1990.

[35] L.A. Marasina, V.V. Malinovsky, I.G. Pichugin, and P. Prentky. Chemical etching of sapphire. *Crystal Res and Technol*, 17(3):365–371, 1982.

[36] Jing Wang, L.W. Guo, H.Q. Jai, Y. Wang, Z.G. Xing, W. Li, H. Chen, and L.M. Zhou. Fabricaiton of patterned sapphire substrate by wet chemical etching of maskless lateral overgrowth of GaN. *Journal of Electrochemical Society*, 3(153):C182–C185, 2006.

[37] H. Ogiya, T. Nishimiya, M. Hiramoto, S. Motoyama, and O. Tsuji. Chlorine-based ICP etching for improving the luminance efficiency in nitride leds. *The International Conference on Compund Semiconductor Manufacturing Technology*, 2012.

[38] F. Demmel, S. Hosokawa, M. Lorenzen, and W.-C. Pilgrim. Propagating particle density fluctuations in molten nacl. *Physical Review*, 69, 2004.

[39] F.C. Cowlard and J. C. Jewis. Vitreous carbon - a new form of carbon. *Journal Of Materials Science*, 2:507–512, 1967.

[40] N.E Herbert, B. Snyder, R.L McCreery, W. G. Kuhr, and S. A. Brazill. Performance of pyrolyzed photoresist carbon films in a microchip capilary electrophoresis device with sinusoidal voltammetric detection. *Anal. Chem.*, 75:4265–4271, 2003.

[41] D.P Munger. The use of photoresist derived carbon as microelectrodes for genetic assays. *B.S. report, WPI Chemical Engineering*, 2008.

[42] S. Ranganathan, R.L McCreery, S.M. Majji, and M. Madou. Photoresist-derived carbon for microelectromechanical systems and electrochemical applications. *Journal of Electrochemical Society*, 147:277–282, 2000.

[43] J. Kim, X. Song, K. Kinoshita, M. Madou, and R. White. Electrochemical studies of carbon films from pyrolyzed photoresist. *J. Electrochem. Soc.*, 1998.

[44] J. Rautavuori and P. Tormala. Coating of microporous glassy carbon with nonporous surface layer. *Journal of Materials Science Letters*, 3:789–790, 1984.

[45] G.K Kiema, S. Ssenyange, and M.T. McDermott. Microfabrication of glassy carbon by electrochemical etching. *Journal of Electrochemical Society*, 151(2):C142–C148, 2004.

[46] Y. Okano and A. Katagiri. Electrochemical behavior of glassy carbon and some metals in a ZnCl2 - NaCl (60-40 mole percent) melt. *J. Electrochem. Soc.*, 144(6), 1997.

[47] K.S. Mohandas, N. Sanil, M. Noel, and P. Rodriques. Anodic behavior of carbon materials in NaCl saturated NaAlCl4 fused electrolyte at low temperatures: A cyclic voltammetryic study. *Journal of Applied Electrochemistry*, 31, 2001.

[48] Nauflett. Supercritical water oxidation reactor with a corrosion-resistant lining. *Patent*, 1995.

[49] S. Hosokawa. Inelastic x-ray scattering experiments at extreme conditions: high temperatures and high pressures. *Condensed Matter Physics*, 11(1):71–81, 2008.

[50] H. Yoshikawa, S. Shikata, N. FIujimori, N. Sato, and T. Ikehata. Smooth surface dry etching of diamond by very high frequency inductively coupled plasma. *New Diamond and Frontier Carbon Technology*, 16(2), 2006.

[51] Inc. Advanced Diamond Technologies. Uncd wafers - diamond MEMS lesson 1. 2010.

[52] C.Q. Sun, H. Xie, W. Zhang, H. Ye, and P. Hing. Preferential oxidation of diamond 111. *J. Phys. D: Appl. Phys*, 33, 2000.

[53] R.R. Nimmagadda, A. Joshi, and W.L. Hsu. Role of microstructure on the oxidation behavior of microwave plasma synthesized diamond and diamond-like carbon films. *Materials Research Society*, 5(11):2445, 1990.

[54] D.A. Stubbs and R.E. Dutton. An ultrasonic sensor for high-temperature materials processing. *JOM*, 48(9):29–31, 1996.

[55] R. Hou, D. Hutson, and K.J. Kirk. Development of sputtered aln thin film ultrasonic transducers for durable high temperature applications. *www.bindt.org*.

[56] Y.-H. Koh, J.-J. Choi, and H.-E. Kim. Strengthening and prevention of oxidation of aluminum nitride by formation of a silica layer on the surface. *J. Am. Ceram. Soc*, 83, 2000.

[57] R.J. Shul, C.G. Willison, M. M. Bridges, J. Han, J.W. Lee, S.J. Pearton, C.R. Abernathy, J.D. MacKenzie, L Zhang, and L.F. Lester. Selective inductively coupled plasma etching of group-iii nitrides in Cl2- and BCL3-based plasmas. *Journal of American Vacuum Society*, 16(3), 1998.

[58] G.L. McIntire and T. K. Hatwar. The corrosion protection behaviour of aluminum nitride and silicon dioxide coatings on magneto-optical media. *Corrosion Science*, 29(7), 1989.

[59] S. Wodin-Schwartz, J.C. Cheng, D.G. Senesky, J. E. Hammer, and A. P. Pisano. Geothermal environmental exposure testing of encapsulant and device materials for harsh environment MEMS sensors. *MEMS 2012*, 2012.

[60] O.F. Tuttle. Two pressure vessels for silicate-water studies. *Bulletin: The Geological Society of America*, 60(10):1727–1729, 1949.

[61] D. Schmeiber, D.R. Batchelor, R.P. Mikalo, P. Hoffmann, and A. Lloyd-Spetz. Oxide growth on SiC(0 0 0 1) surfaces. *Applied Surface Science*, 184:340–345, 2001.

[62] Z. Zolnai, N.Q. Khanh, E. Szilagyi, Z.E. Horvath, and T. Lohner. Native oxide and ion implantation damaged layers on silicon carbide studied by ion beam analysis and ellipsometry. *HQ Books*, 2012.

[63] P. Kritzer. Corrosion in high-temperature and supercritical water and aqeos solutions: a review. *J. of Supercritical Fluids*, 29:1–29, 2004.

[64] V.M. Valyashko. Phase behavior in the binary and ternary water-salt systems at high temperatures and pressures. *Pure and Appl. Chem*, 69(11):2271–2280, 1997.

[65] L.B. Kirksunov and D.D. Macdonald. Corrosion in supercritical water oxidation systems: A phenomenological analysis. *J. Electrochem. Soc.*, 142(12):4069–4073, 1995.

[66] L.B. Kriksunov and D.D. Macdonald. Corrosion testing and prediction in scwo environments. *ASME Heat Transfer Division*, page 281, 1995.

[67] D.B. Mitton, N. Eliaz, J.A. Cline, and R.M. Latanision. An overview of the current understanding of corrosion in scwo systems for the destruction of hazardous waste products. *Mat. Tech and Adv. Perf. Mat.*, 16:44–53, 2001.

[68] Y.G. Gogotsi, P. Kofstad, M. Yoshimura, and K.G. Nickel. Formation of sp3-bonded carbon upon hydrothermal treatment of SiC. *Diamond and Related Materials*, 1996.

[69] Y. Gogotsi and M. Yoshimura. Degradation of SiC (Tyranno) fibres in high-temperature, high-pressure water. *Journal of Materials Science Letters*, 14:755–759, 1995.

[70] R. Roy, D. Ravichandran, A. Badzian, and E. Breval. Attempted hydrothermal synthesis of diamond by hydrolysis of P-SiC powder. *Diamond and Related Materials*, 5, 1996.

[71] H. Lu, T. Chen, J Jiu, P. Pent, Z Lu, and Q. Ma. Yields of H2S and gaseous hydrocarbons in gold tube experiments simulating thermochemical sulfate reduction reactions between MgSO4 and petroleum fractions. *Organic Geochemistry*, 41:1189–1197, 2010.

[72] T. Kraft and K.G. Nickel. Carbon formed by hydrothermal treatment of a-SiC crystals. *J. Mater. Chem*, 10:671–680, 2000.

[73] Y. Nagai, N. Matubayasi, and M. Nakahara. Mechanisms and kinetics of noncatalytic ether reaction in supercritical water. 1. proton-transfered fragmentation of diethyl ether to acetaldehyde in competition with hydrolysis. *J. Phys. Chem*, (109):3550–3557, 2005.

[74] A. P. Dementjev and M. N. Petukhov. Comparison of x-ray-excited auger line shapes of graphite, polyethylene and diamond. *Surface and Interface Analysis*, 24:517–521, 1996.

[75] Einar Gunnlaugsson. Importance of chemistry in geothermal exploraiton and utilization. *Workshop for Decision Makers on Direct Heating Use of Geothermal Resources in Asia*, 2008.

[76] Micro-chip Technologies. Ntc thermistors. 2010.

[77] Burns Engineering. Frequently asked questions. *Internal Publication*.

[78] R.E. Bently. Temperature and humidity measurement. *Handbook of temperature measurement*, 1(Springer), 1998.

[79] Sean Scott and Dimitrios Peroulis. A capacitively-loaded MEMS slot element for wireless temperature sensing of up to 300C. *IEEE*, pages 1161–1164, 2009.

[80] Don C. Abeysinghe, Samhita Dasgupta, Howard E. Jackson, and Joseph T Boyd. Novel MEMS pressure and temperature sensors fabricated on optical fibers. *Journal of MIcromechanics Microengineering*, 12:229–235, 2002.

[81] C.M. Jha, G. Bahl, R. Melamud, S.A. Chandorkar, M. Hopcroft, B. Kim, M. Agarwal, J. Salvia, H. Mehta, and T. W. Kenny. CMOS-compatible dual-resonator MEMS temperature sensor with milli-degree accuracy. *Proceedings of solid-state sensors, actuators and microsystems conference*, 2007.

[82] Y. Wang, Y. Jia, Q. Chen, and Y. Wang. A passive wireless temperature sensor for harsh environment applications. *sensors*, 8:7982–7995, 2008.

[83] Ching-Liang Dai, Jin-Yu Hong, and Mao-Chen Liu. High Q-factor CMOS-MEMS inductor. *DTIP of MEMS and MOEMS*, 2008.

[84] L. Li and D. Uttamchandani. Monolithic RF MEMS inductor using silicon MEMS foundry process. *Micro and Nano Letters*, 1(1):5–8, 2006.

[85] Sheng-Hsiang Tseng, Ying-Jui Hung, Ying-Zong Juang, and Michael S.-C. Lu. A 5.8-GHz VCO with CMOS-compatible MEMS inductors. *Sensors and Actuators*, 139:187–193, 2007.

[86] James J. Wang. Adjustable, integrated inductors and transformers. *INDUCTICA Conference*, 2010.

[87] Sergey Y. Yurish. Universal capacitive sensors and transducers interface. *Eurosensors XXII Conference*, pages 441–444, 2009.

[88] Martin Ruff, Heinz Mitlehner, and Reinhard Helbig. SiC devices: Physics and numerical simulation. *IEEE Transactions on Electron Devices*, 41(6), 1994.

[89] Clinton Gregory Warren. Polymer-ceramic MEMS bimorphs as thermal infrared sensors. *PhD Thesis, UC Berkeley*, page 105, 2010.

[90] Robert Azevado, Debbie G. Jones, Anand V. Jog, Babak Jamshidi, David R. Myers, Li Chen, Xiao-an Fu, M. Mehregany, M.B.J Wijesundara, and A. P. Pisano. A SiC MEMS resonant strain sensor for harsh environment applications. *IEEE Sensors Journal*, 7(4):568–577, 2007.

[91] Babak Jamshidi. Poly-crystalline silicon carbide passivated capacitive MEMS strain gauge for harsh environments. *PhD Thesis, UC Berkeley*, page 157, 2008.

[92] Irvine Sensors. Ms3110 universal capacitive readout ic. 2004.

[93] A Timoshenko. Analysis of bi-metal thermostats. *J. Opt. Soc. Am.*, 11(3):233–233, 1925.

[94] Mohammad Shavezipur. Novel MEMS tunable capacitors with linear capacitance-voltage response considering fabrication uncertainties. *PhD Thesis, University of Waterloo*, 2008.

[95] MEMSCAP. PolyMUMPs process. *http://www.MEMScap.com/products/mumps*.

[96] A. N. Sohi, M. Shavesipur, P. Nieva, and A. Khajepour. A structurally multifunctional pressure-temperature sensor. *2nd Microsystems and Nanoelectronics Research Conference (MNRC)*, 2009.

[97] Sean Scott, F. Sadeghi, and D. Peroulis. Highly reliable MEMS temperature sensors for 275C applications - part 2 design and technology. *Journal of Microelectromechanical Systems*, 22(1), 2013.

[98] Sean Scott, J. Katz, F. Sadeghi, and D. Peroulis. Highly reliable MEMS temperature sensors for 275C applications - part 2 creep and cycling performance. *Journal of Microelectromechanical Systems*, 22(1), 2013.

[99] N. Zhang, J.C. Cheng, C.G. Warren, and A. P. Pisano. Bioinspired, uncooled chitin photomechanical sensor for thermal infrared sensing. *IEEE Sensors Journal*, 2011.

[100] R.T. Howe R. Maboudian C. S. Roper, V. Radmilovic. Effects of annealing on residual stress and strain gradient of doped polycrystalline SiC thin films. *Electrochemical and Solid-State Letter*, 11:D35–D37, 2008.

[101] H-Y Chu, M-H Weng, C-C Nien, C. Lin, and K-I Hu. The influence of sputtering power of aluminum film in aluminum induced crystallization of low temperature poly-silicon film. *Conference of Nano/Micro Engineerd and Molular Systems*, pages 1190–1193, 2006.

[102] A.E. Franke, J.M. Heck, T-J King, and R.T. Howe. Polycrystalline silicongermanium films for integrated microsystems. *J. MEMS*, 12(2), 2003.

[103] F. Liu, B. Hsia, C. Carraro, A.P. Pisano, and R. Maboudian. Enhanced ohmic contact via graphitization of polycrystalline silicon carbide. *Appl. Phys. Lett*, 97(26), 2010.

[104] J. Zhang, R.T. Howe, and R. Maboudian. Nickel and platinum ohmic contacts to polycrystalline 3C-silicon carbide. *Mater. Sci. Eng.*, 139:235–239, 2007.

[105] H. Yang, T. Peng, W. Wang, and X. Chen. Interface metallization and electrical characterization of Ta-Pt multilayers on N-type SiC. *Appl. Surf. Sci*, 255:3121–3125, 2008.

[106] M.W. Cole, P.C. Joshi, C.W Hubbard, M.C. Wood, M.H. Ervin, B. Geil, and F. Ren. Improved Ni based composite ohmic contact to N-SiC for high temperature and high power device applications. *Appl Physics*, 88(5):2652–2657, 2000.

[107] Stanislav CICHO, Bohumil BARDA, and Petr MACH. Ni and Ni silicides ohmic contacts on N-type 6H-SiC with medium and low doping level. *Radioengineering*, 20(1):209–213, 2011.

[108] A. V. Kuchuk, V. P. Kladko, A. Piotrowska, R. Ratajczak, and R. Jakiela. On the formation of Ni - based ohmic contacts to N-type 4H-SiC. *Materials Science Forum*, 615-617:573–576, 2009.

[109] A.V. Kuchuk, M. Guziewicz, R. Ratajczak, M. Wzorek, V.P. Kladko, and A. Piotrowska. Long-term stability of Nisilicide ohmic contact to N-type 4HSiC. *Microelectronic Engineering*, 85(2142-2145), 2008.

[110] J. Foggiatoa, W.S. Yooa, M. Ouakninea, T. Murakamib, and T. Fukadab. Optimizing the formation of nickel silicide. *Materials Science and Engineering B*, 114, 2004.

[111] D.R. Harrison and J. Dimeff. A diode-quad bridge circuit of use with capacitance transducers. *Review of Scientific Instruments*, 44:1468, 1973.

[112] Autoclave Engineers. Technical information.

Appendix A

SEM Images from Brine Testing
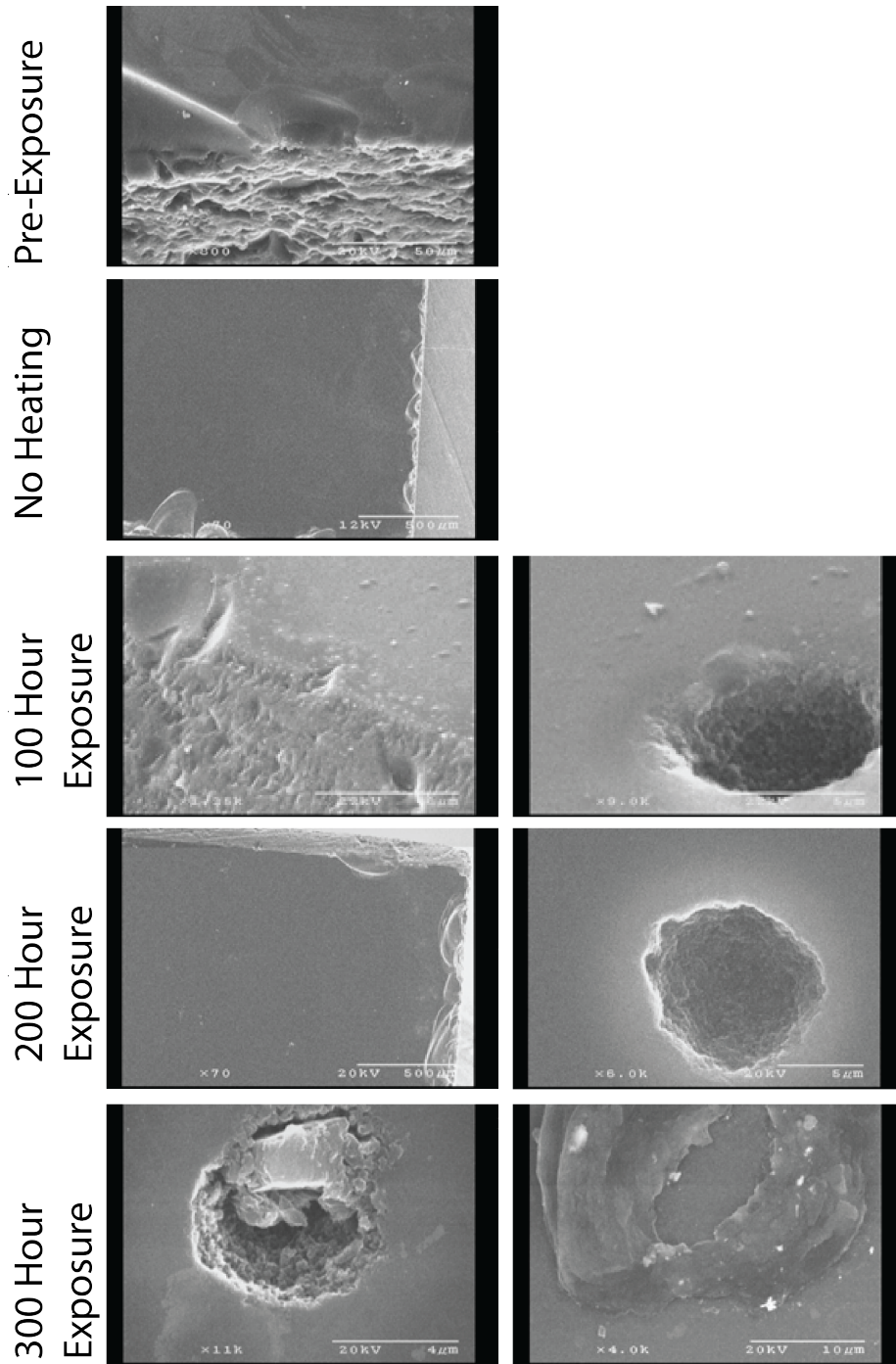
Figure A.1. SEM images of vitreous carbon exposed for different times in the simulated geothermal brine environment.
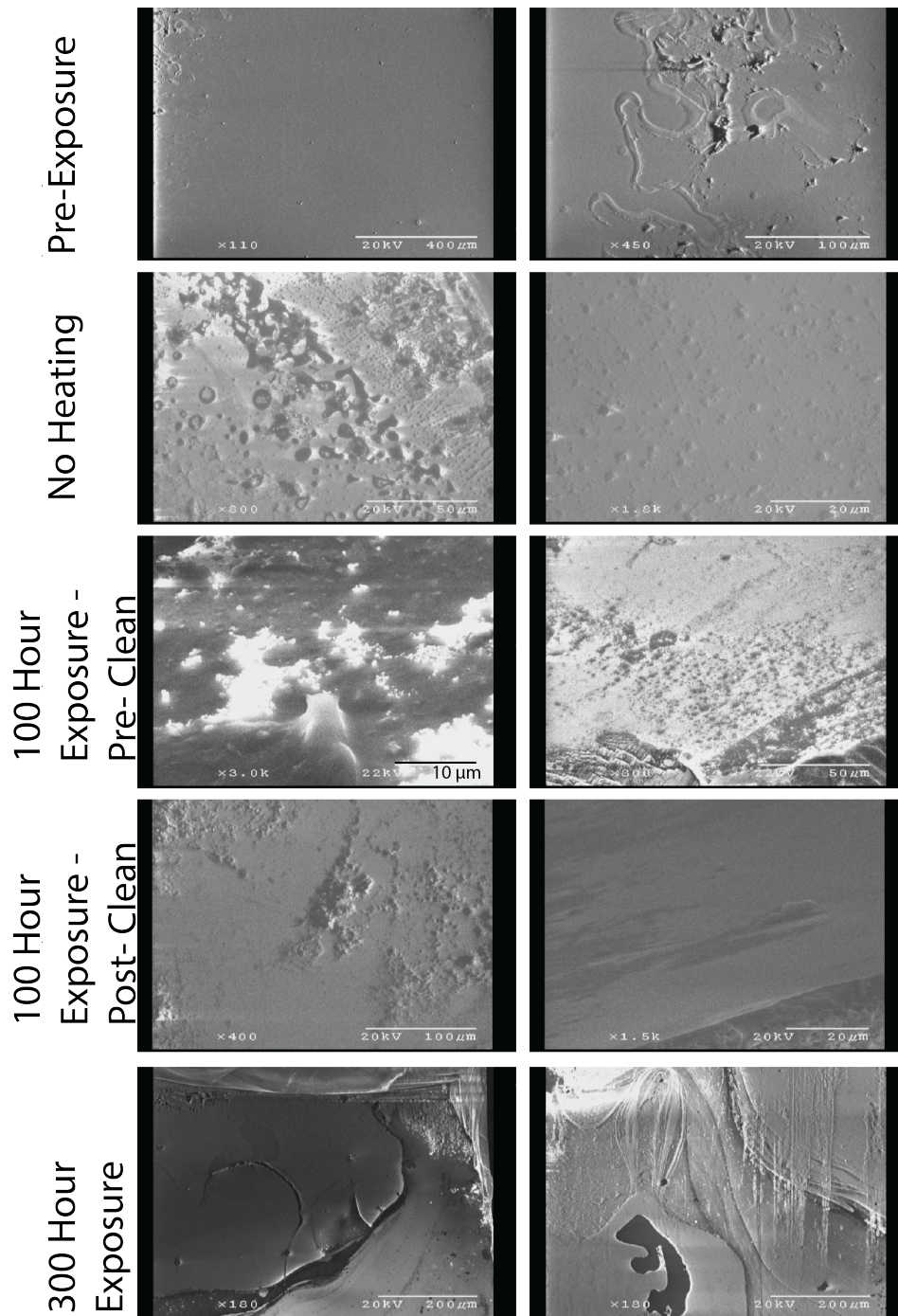
Figure A.2. SEM images of sapphire exposed for different times in the simulated geothermal brine environment. A 300 hour sample, from a burst capsule, is shown below a pre-exposure die, the properly tested control, and a 100 hour sample.

Surface Scan   Side Profile
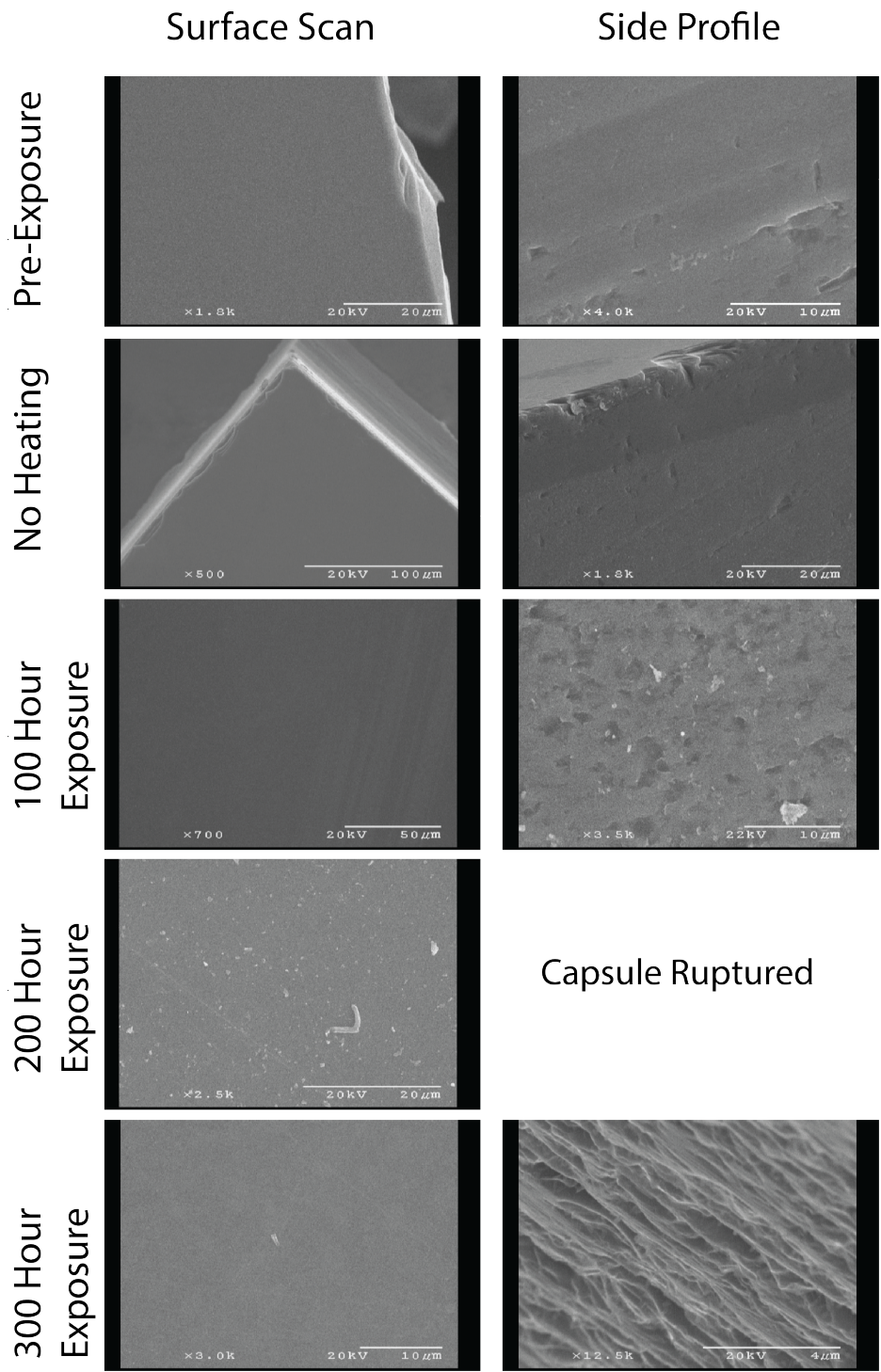
Figure A.3. SEMs of SiC exposed for different times in the simulated geothermal brine environment.

Surface Scan   Side Profile

Pre-Exposure

No Heating

100 Hour
Exposure

200 Hour
Exposure

300 Hour
Exposure

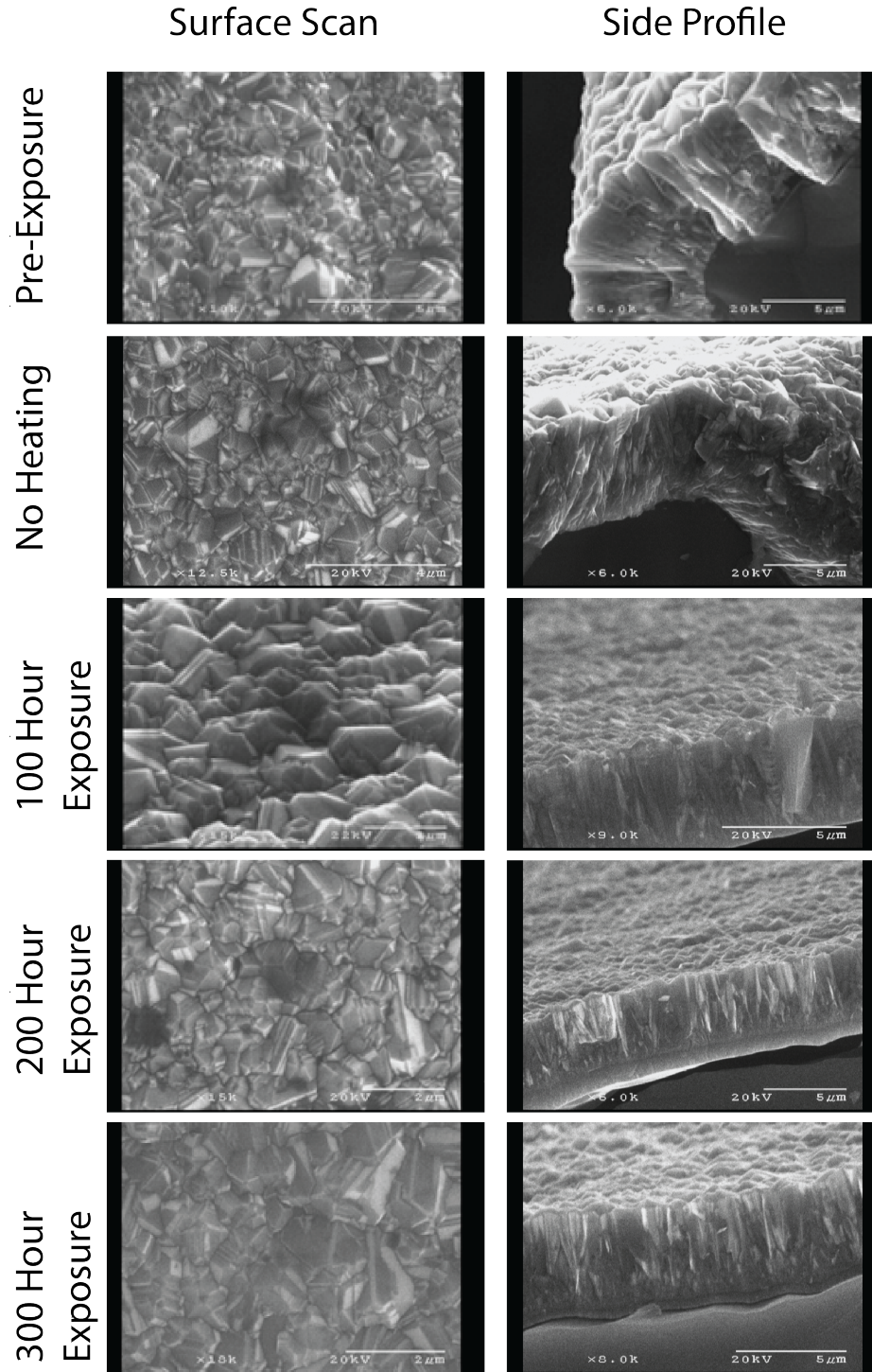Figure A.4. SEMs of micro-crystalline exposed for different times in the simulated geothermal brine environment.

Appendix B

Fabrication Process Flows - In-Plane Temperature Sensors

Step #	Equipment	Process Step	Thickness (um)	Time	Chemicals/Parameters
1	Msink 8&6	Clean Wafers		10 min/sink	H2SO4 +H2O2
2	Tystar 15	Deposit SiC	1.5	5h33min	800 degC, NH3=2.5, DCS = 30, pressure = 170
3	Tystar 12	Deposit SiO2	0.5	45min	450 degC, SiH4, O2
4	Tystar 4	Anneal		10 h	Argon, 1050 degC
5	Primeoven	Deposit HMDS		2min	HMDS
6	svgcoat	Spin PR	1.3	30 sec	5000RPM, OCG 825 (G-line), 90 sec bake at 90degC, 6 sec chill
7	gcaws2	expose PR		2 sec	
8	svgdev	develop PR		60 sec	OCG 934 2:1 - 2x30sec
9	uvbake	hard bake PR		5 min	program S
10	lam6	etch hard mask	0.5		
11	matrix	remove PR			
12	lam8	etch SiC			
13	lam6	remove oxide mask			
14	Msink 8&6	Clean Wafers		10 min/sink	H2SO4 +H2O2
15	Tystar 12	Deposit SiO2	1.5	2h15min	450 degC, SiH4, O2
16	lam6	etch top and bottom oxide	1.5		
17	svgcoat	Spin PR	1.3	30 sec	5000RPM, OCG 825 (G-line), 90 sec bake at 90degC, 6 sec chill
18	gcaws2	expose PR		2 sec	
19	svgdev	develop PR		60 sec	OCG 934 2:1 - 2x30sec
20	uvbake	hard bake PR		5 min	program S
21	Msink18	HF dip			1000 A/min
22	matrix	remove PR			
23	svgcoat	Spin PR	1.1	30 sec	4100RPM OiR 10i (I-line), 60 sec bake at 90degC, 6 sec chill
24	ksaligner	Flood expose		10 sec	intensity 9.8 mw/cm^2
25	svgcoat	Spin PR	1.3	30 sec	5000RPM, OCG 825 (G-line), 90 sec bake at 90degC, 6 sec chill
26	gcaws2	expose PR		2 sec	
27	svgdev	develop PR		60 sec	OCG 934 2:1 - 2x30sec
28	edwards	sputter Pt and Cr adhesion layer	30 nm and 100 nm		
29	msink18	lift off		10 min	acetone in sonicator bath
30	disco	dice			
31	xetch	release	30	?	XeFl2, N2

Table B.1. Fabrication flow of the thin in-plane temperature sensors fabrication run.

Step #	Equipment	Process Step	Thickness (um)	Time	Chemicals/Parameters
1	Msink 8&6	Clean Wafers		10 min/sink	H2SO4 +H2O2
2	Tystar 15	Deposit SiC	1.3	5h33min	800 degC, NH3=2.5, DCS = 30, pressure = 170
3	Tystar 4	Anneal		10 h	Argon, 1050 degC
4	Tystar 15	Deposit SiC	1.3	5h33min	800 degC, NH3=2.5, DCS = 30, pressure = 170
5	Tystar 4	Anneal		10 h	Argon, 1050 degC
6	Tystar 15	Deposit SiC	1.3	5h33min	800 degC, NH3=2.5, DCS = 30, pressure = 170
7	Tystar 4	Anneal		10 h	Argon, 1050 degC
8	Tystar 15	Deposit SiC	1.3	5h33min	800 degC, NH3=2.5, DCS = 30, pressure = 170
9	Tystar 4	Anneal		10 h	Argon, 1050 degC
10	Tystar 15	Deposit SiC	1.3	5h33min	800 degC, NH3=2.5, DCS = 30, pressure = 170
11	Tystar 4	Anneal		10 h	Argon, 1050 degC
12	Tystar 12	Deposit SiO2	2	3h	450 degC, SiH4, O2
13	Primeoven	Deposit HMDS		2min	HMDS
14	svgcoat	Spin PR	1.3	30 sec	5000RPM, OCG 825 (G-line), 90 sec bake at 90degC, 6 sec chill
15	gcaws6	expose PR		2.8 sec	
16	svgdev	develop PR		60 sec	OPD 4262
17	uvbake	hard bake PR		5 min	program S
18	sts-oxide	etch hard mask	2	7 min	pressure 4 mtorr - strike pressure 10 mTorr, C4F8 = 15 sccm, He = 174 sccm, H2 = 8 sccm, 13.56MHz coil = 1500W, 13.56MHz Platen (bias) =350 W, chiller temp = 0degC
19	matrix	remove PR			
20	lam8	etch SiC		50 min	HBr = 125 sccm, CL2 = 75 sccm, pressure = 12 mtorr, TCP RF = 300 W, Bias RF = 150 W, gap = 6.03 cm, chiller temp = 40degC, ESC = 660V
21	sts-oxide	remove oxide mask		1 min	
22	Msink18	remove polymer coating from sts-oxide		10 min	EKC 270 from Dupont - heated in water bath ~90degC
23	Msink 8&6	Clean Wafers		10 min/sink	H2SO4 +H2O2
24	Tystar 12	Deposit SiO2	3	4h22min	450 degC, SiH4, O2
25	sts-oxide	etch top and bottom oxide	2.7	9 min	pressure 4 mtorr - strike pressure 10 mTorr, C4F8 = 15 sccm, He = 174 sccm, H2 = 8 sccm, 13.56MHz coil = 1500W, 13.56MHz Platen (bias) =350 W, chiller temp = 0degC
26	Msink 8&6	Clean Wafers		10 min/sink	H2SO4 +H2O2
27	Tystar16	Deposit Poly-Si	300 nm	30 min	N2, SiH4, 615degC
28	Primeoven	Deposit HMDS		2 min	HMDS
29	headway	Spin PR	5um	30 sec	500RPM, OiR 10i (I-line), 120 sec bake at 90degC
30	gcaws6	expose PR		10 sec	
31	svgdev	develop PR		90 sec	OPD 4262, 60 sec+30sec
32	oven	hard bake PR		1h	
33	sts-oxide	RIE oxide	6.5um	9 min	
34	msink3	remove PR		1h	PRS 3000
35	svgcoat	Spin PR	1.1	30 sec	4100RPM OiR 10i (I-line), 60 sec bake at 90degC, 6 sec chill
36	ksaligner	Flood expose		10 sec	intensity 9.8 mw/cm^2
37	svgcoat	Spin PR	1.3	30 sec	5000RPM, OCG 825 (G-line), 90 sec bake at 90degC, 6 sec chill
38	gcaws6	expose PR		2 sec	
39	svgdev	develop PR		60 sec	OCG 934 2:1 - 2x30sec
40	edwards	sputter Pt and Cr adhesion layer	30 nm and 100 nm		
41	msink18	lift off		10 min	acetone in sonicator bath
42	disco	dice			
43	xetch	release	30	?	XeFl2, N2

Table B.2. Fabrication flow of the thicker in-plane temperature sensor fabrication using the final side wall fabrication method.

Appendix C

Design of Wired Pressure Vessel for Operational Sensor Testing

The pressure vessel used for initial testing, a cold seal (Tuttle-type), is very simplistic in its design. This type of experimental setup is ideal for materials testing and before and after testing of functioning sensors. However, to test operational sensors within the simulated geothermal environment a fixture that allows for feedthroughs is necessary. While standard power feedthroughs can survive the pressures and temperatures within the pressure vessel, the corrosive brine chemistry would lead to standard feedthrough failures. Designs for both the pressure vessel and the die attachment system were evaluated based on their ability to expose minimal surfaces other than the sensor to the brine fluid, ease of assembly, ease of manufacturing, and safety of use. All of the designs were evaluated using pressure vessel equations and allowing for adequate safety factors. For the wired sensor testing, the backside of the sensor chip may have an integrated diode-quad bridge circuit, configured to improve capacitive signal transmission [111]. This transducer bridge allows for high output independent of the excitation waveform and frequency, has a high resolution of 4.4 x 10^{-8} at 10-30 Hz, and can ground the sensor. For all designs, wires will be run through the feedthrough and will be insulted using ceramic thermocouple wire shielding. Either wire-bonding or through etching with electroplated fill will be used to make electrical connections between the sensor and the feedthrough. Gold will be used to cover the interior walls of the vessel to limit brine contamination with elemental leaching from the sides of the exposed vessel.

The stresses in a thick walled pressure vessel can be solved for by looking at the forces on a element within the vessel wall as shown in Figure D.1. This element, defined within a radial coordinate system, has circumferential and radial stresses shown at a distance, r, from the center of the vessel. By assuming static equilibrium, the forces along the radial axis can be summed to zero.

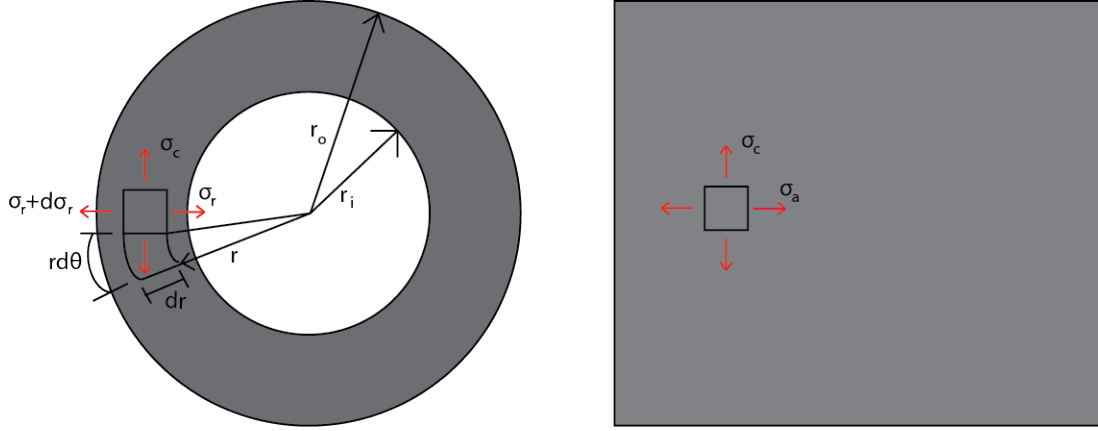$$(\sigma_r + d\sigma_r)(r + dr)d\theta = \sigma_r r d\theta + \sigma_c d\theta dr \tag{C.1}$$

Figure C.1. Stress elements labeled on a thick walled pressure vessel. The circumferential stress, σ_c, the radial stress, σ_r, and the axial stress, σ_a, are shown.

A full derivation can be seen in Appendix D. The maximum stresses occur at the inside, r_i, surface and are described by:

$$\sigma_c = \frac{-2P_o r_o^2}{r_o^2 - r_i^2} \tag{C.2}$$

$$\sigma_r = 0 \tag{C.3}$$

$$\sigma_a = \frac{-P_o r_o^2}{r_o^2 - r_i^2} \tag{C.4}$$

Once the strain equations were understood, the potential materials yield stress values were evaluated at the temperature at which the vessel would operate. The leading potential materials for the vessel included 316 stainless steel, 304 stainless steel, Hastelloy C276, Inconel 625 and Inconel 600. Data for these materials was collected from Autoclave Engineers [112]. Both stainless steels initially have high pressure ratings, 100% to 85%, up to 427 °C before cycling above that temperature. However, post cycling, the pressure rating reduces to at maximum 40% of the room temperature pressure rating once temperature is elevated. Both Hastelloy and both Inconel grades have lower initial pressure ratings than stainless steel, between 35%-60%, and they have better high temperature performance. Inconel 600 has a 100% pressure rating of the initial pressure rating up to 427 °C; however, there is a large drop off in performance, reaching 10% of the initial pressure rating by 649 °C. Inconel 625 begins to lose some of its strength by 200 °C; however it still has and 85% pressure rating by 600 °C and 50% by 649 °C, making it the most attractive material option. Hastelloy follows a similar temperature performance trend to that of Inconel 625; however, with a lower initial pressure rating, it is a less attractive option.

Once the material properties are understood, the internal and external dimensions of the

pressure vessel portion of the test setup can be set. From there, the design of the wired feedthrough system can be designed.

While many design iterations were contemplated, one design iteration most directly lead to the two final designs for reusable test assemblies. This first completed design iteration, shown in Figure C.2, utilized a double tunnel style design. This design nests a feedthrough system within a brine filled vessel. The geothermal brine fluid surrounds the outside of the smaller inside feedthrough. A channel is milled into the end of the feedthrough to allow for a pinned spacer to apply axial loading onto a gold gasket sealing at the MEMS chip face. The channel and pin prevent shear loading of the gasket and at the die face. The feedthrough is conically sealed into the outer pressure vessel in a similar manor to the sealing of the Tuddle type pressure vessel. The non-feedthrough side of the vessel has the pressurizing line. This would act as an inlet and connect to a water or brine pressure line. This design, shown in Figure C.3, was printed using ABS plastic in a 3D printer to demonstrate the concept. While this test set-up design would hold the die in place for testing, there is a threaded component that is exposed to the geothermal brine environment.
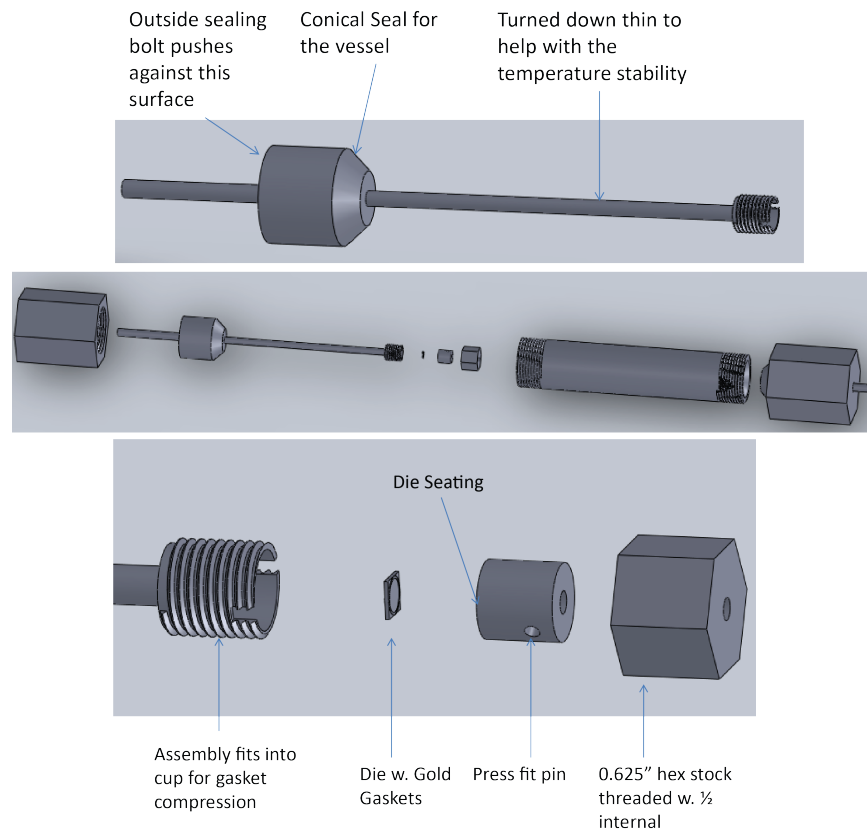

Figure C.2. Initial design holds die in place with threads that are exposed to the brine environment.

Based on the first prototyped design, the first final reusable test vessel design was generated, see Figure C.4. This new design moved all threaded components to an area isolated from the supercritical brine region of the set-up. A thrust bearing was introduced to the
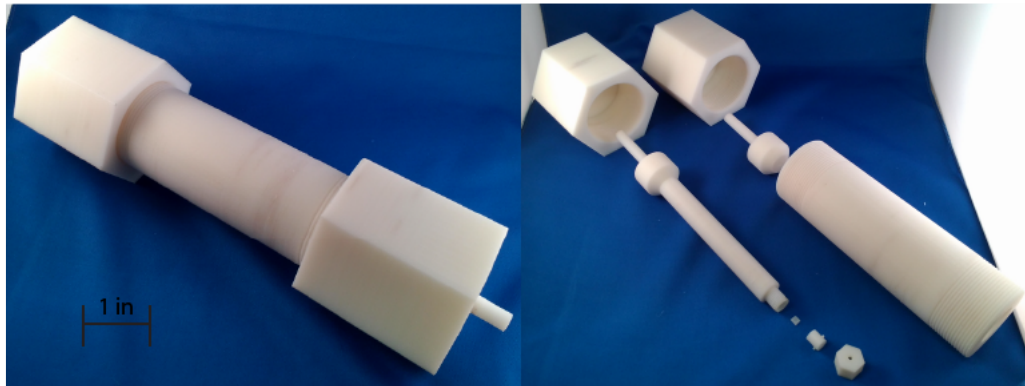
116

Figure C.3. 3D printed version of initial pressure vessel design with wire feedthroughs.

design, located behind the MEMS chip, to continue to allow for axial loading on the chip with the removal of the slot and pin system seen in the previous design. The design still incorporates gold gaskets for sealing. A die holder piece is custom made to integrate either wirebonds or through etching and electroplating of MEMS sensors for electrical connections. This piece is designed to fit within the thrust bearing to allow for free rotation. A hallow push rod is used to axial compress the gold gaskets used to seal the fluid region. A secondary feedthrough is not shown in the graphic, but would be integrated into the push rod to act as a backup sealing mechanism in the event of a gasket rupture. In addition to removing the threads from the exposed brine region, the die is moved closer to the bulk of the brine fluid region. The inlet for this design is the same as that shown in the initial prototype.

The other final design differs more dramatically from the initial prototype. This design, shown in Figure C.5, has the geothermal brine volume located within the smaller interior vessel rather than surrounding a feedthrough system. This type of design allows for the reduction in overall set-up size as the high pressure area is much smaller. The MEMS die is sealed to the interior tubing using gold gaskets by the axial loading provided by the tightening of the inner tube into the outer tube as transfered through a thrust bearing. Conical sealing is used to integrate the inner tube with the external water or brine line for fluid pressurization. The backup feedthrough is also conically sealed to the outer vessel. While this design reduces required fluid, set-up size, and machining complexity, it increases the difficulty of assembly. The entire vessel must be assembled before the sensor can be tested in air before brine exposure.

While reusable vessel designs are desirable because they can reduce cost and waste, a disposable type of sensor packaging may be favorable for the initial testing of functioning sensors within the geothermal environment. A disposable type of design could be made of a
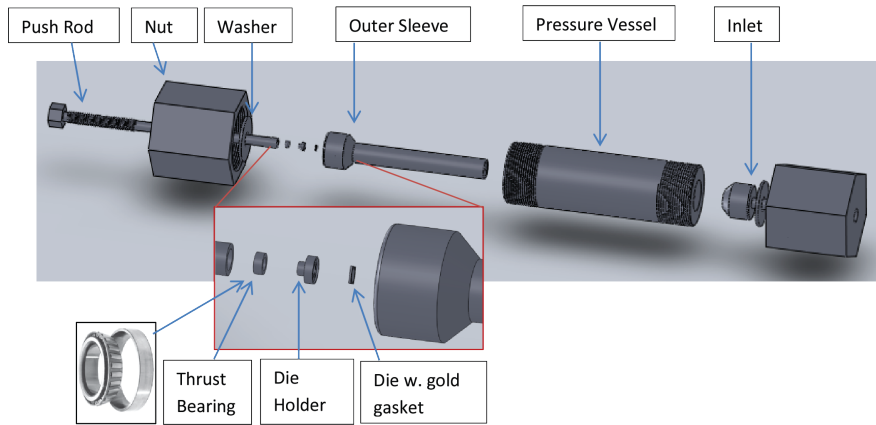
Figure C.4. Water in larger volume area allows for assembly of electrical connection for testing pre-full vessel assembly. Need to add feedthrough to push rod in image, but basic design in shown.

tube that is then back filled with high temperature epoxy, which would eliminate the need for a backup feedthrough.
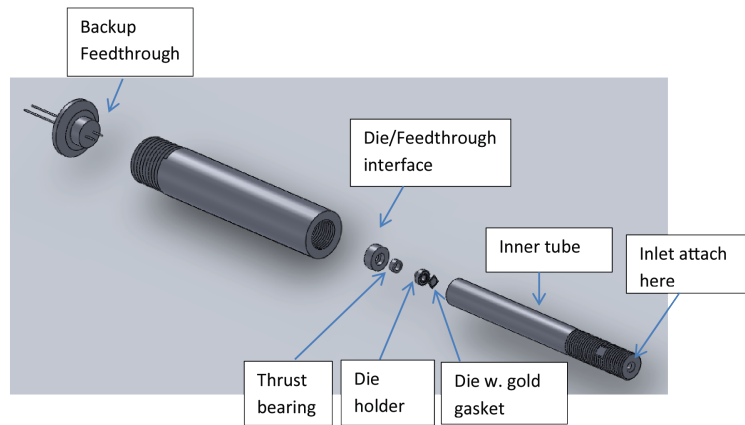
Figure C.5. This design has the following advantages and disadvantages: 1) Brine on inside of inner tube. 2) Smaller volume of brine. 3) Smaller overall structure. 4) May be easier to machine as critical surfaces are on outside of long rod. 4) Can not test wiring until fully assembled.

Appendix D

Pressure Vessel Equations

This derivation is based on that done at the University of Washington in their ME354a course.

The stresses in a thick walled pressure vessel can be solved for by looking at the forces on a element within the vessel wall as shown in Figure, D.1. This element, defined within a radial coordinate system, has circumferential and radial stresses shown at a distance r from the center of the vessel. By assuming static equilibrium, the forces along the radial axis can be summed to zero.
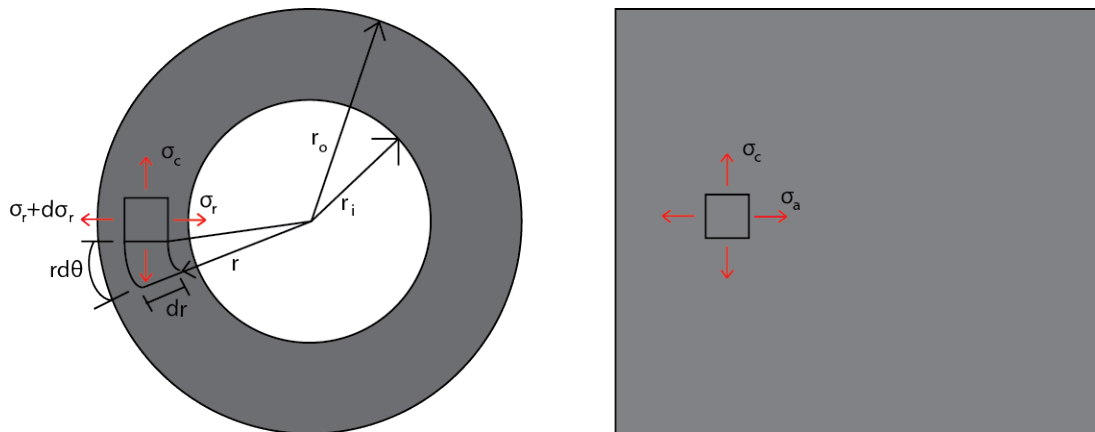

Figure D.1. Stress elements labeled on a thick walled pressure vessel. σ_c is the circumferential stress, σ_r is the radial stress, and σ_a is the axial stress.

$$(\sigma_r + d\sigma_r)(r + dr)d\theta = \sigma_r r d\theta + \sigma_c d\theta dr \tag{D.1}$$

By canceling out the second order term, this can be simplified to:

$$-\sigma_c + \sigma_r + \frac{r d\sigma_r}{dr} = 0 \tag{D.2}$$

This equation leaves two unknowns, σ_r and σ_c. It can be assumed that plane sections of the pipe remain plane along the length of the pipe after it has expanded due to internal pressure. Also, linearly elastic material properties are assumed. Based on these assumptions the strain may be analyzed. Figure D.2 shows an element pre- and post-strained. Line ab has a length of $rd\theta$ and line a'b' has a length $(r+u)d\theta$ for a given radial displacement of u, shown by line b'b. Point c is displaced in the radial direction by $(u + du)$, where du is the differential displacement seen over the length bc. The radial strain can be written as:

$$\epsilon_r = \frac{u + du - u}{dr} = \frac{du}{dr} \tag{D.3}$$

In the circumferential direction, the strain can be observed when looking at the change in length from line ab to that of line a'b'. Line ab has a length $rd\theta$ where line a'b' has a length $(r+u)d\theta$. The circumferential strain is written as:

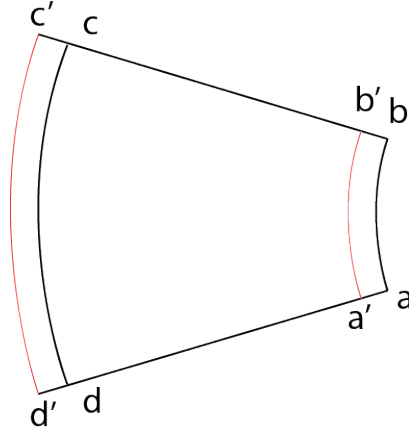$$\epsilon_c = \frac{(r + u)d\theta - rd\theta}{rd\theta} = \frac{u}{r} \tag{D.4}$$

Figure D.2. Stress elements labeled with pre- and post- strained points. a,b,c, and d represent the pre-strained element. Points a',b',c', and d' show the element post-strain.

The ends of the vessel are assumed to be open at this point in the derivation. Based on this assumption, it can be said that $\sigma_r = 0$. Hooke's law can be used to solve for the stresses in terms of the strain.

$$\epsilon_r = \frac{du}{dr} = \frac{1}{E}(\sigma_r - \nu\sigma_c) \tag{D.5}$$

where ν is Poisson's ratio, and:

$$\epsilon_c = \frac{u}{r} = \frac{1}{E}(\sigma_c - \sigma_r) \tag{D.6}$$

121

Stress can be isolated from these equations and written as:

$$\sigma_r = \frac{E}{1-\nu^2}\left(\frac{du}{dr} + \nu\frac{u}{r}\right) \tag{D.7}$$

and:

$$\sigma_c = \frac{E}{1-\nu^2}\left(\frac{u}{r} + \nu\frac{du}{dr}\right) \tag{D.8}$$

These equations can then be substituted into Equation D.2 and simplified to get the differential equation:

$$\frac{d^2u}{dr^2} + \frac{1}{r}\frac{du}{dr} - \frac{u}{r^2} = 0 \tag{D.9}$$

This differential equation has a solution in the form:

$$u = C_1 r + \frac{C_2}{r} \tag{D.10}$$

Substituting this solution form into the stress equations gives:

$$\sigma_r = \frac{E}{1-\nu^2}\left(C_1(1+\nu) - C_2\left(\frac{1-\nu}{r^2}\right)\right) \tag{D.11}$$

and:

$$\sigma_c = \frac{E}{1-\nu^2}\left(C_1(1+\nu) + C_2\left(\frac{1-\nu}{r^2}\right)\right) \tag{D.12}$$

Now that the characteristic equations are known, boundary conditions can be applied to solve for the integration constants. Using the external and internal pressures applied to the pressure vessel, $\sigma_r(r_o) = -P_o$ and $\sigma_r(r_i) = -P_i$ respectively. The constants are found to be:

$$C_1 = \frac{1-\nu}{E}\left(\frac{r_i^2 P_i - r_o^2 P_o}{r_o^2 - r_i^2}\right) \tag{D.13}$$

$$C_2 = \frac{1-\nu}{E}\left(\frac{r_i^2 r_o^2 (P_i - P_o)}{r_o^2 - r_i^2}\right) \tag{D.14}$$

The stresses along the radius of the pressure vessel, represented by Lame's equations are given as:

$$\sigma_r = \left(\frac{r_i^2 P_i - r_o^2 P_o}{r_o^2 - r_i^2}\right) - \left(\frac{r_i^2 r_o^2 (P_i - P_o)}{(r_o^2 - r_i^2)r^2}\right) \tag{D.15}$$

and:

$$\sigma_c = \left(\frac{r_i^2 P_i - r_o^2 P_o}{r_o^2 - r_i^2}\right) + \left(\frac{r_i^2 r_o^2 (P_i - P_o)}{(r_o^2 - r_i^2)r^2}\right) \tag{D.16}$$

As the ends of this pressure vessel will be sealed, there will be an axial component of stress added to the system. Now, rather than $\sigma_a = 0$, $\sigma_a = $ -K. Where, based on the balancing of forces:

$$\sigma_a = \left(\frac{r_i^2 P_i - r_o^2 P_o}{r_o^2 - r_i^2} \right) \tag{D.17}$$

In the designing of this pressure vessel, the external pressure, P_o, can be assumed to be zero. This simplifies the governing equations to:

$$\sigma_c = \frac{-P_o r_o^2}{r_o^2 - r_i^2} \left(1 + \frac{r_i^2}{r^2} \right) \tag{D.18}$$

$$\sigma_r = \frac{-P_o r_o^2}{r_o^2 - r_i^2} \left(1 - \frac{r_i^2}{r^2} \right) \tag{D.19}$$

$$\sigma_a = \frac{-P_o r_o^2}{r_o^2 - r_i^2} \tag{D.20}$$